DISSERTATION

ORGANIC CATION DYNAMICS AND PROPERTY RELATIONSHIPS IN LAYERED PEROVSKITE DERIVATIVES

Submitted by

Alexandra A. Koegel

Department of Chemistry

In partial fulfillment of the requirements

For the Degree of Doctor of Philosophy

Colorado State University

Fort Collins, Colorado

Fall 2022

Doctoral Committee:

Advisor: James R. Neilson

Christopher Ackerson
Alan Kennan
James Sites

ABSTRACT

ORGANIC CATION DYNAMICS AND PROPERTY RELATIONSHIPS IN LAYERED PEROVSKITE DERIVATIVES

Layered hybrid halide perovskites are materials with applications in solid-state lighting due to their intrinsic white light emission. Layered hybrid perovskite derivates typically have the composition, $(A')_2(A)_{n-1}B_nX_{3n+1}$, where A' = R$-NH_3^+$ containing organic cation, A = methylammonium ($CH_3NH_3^+$, MA), B = Sn, Pb, X = Cl, Br, I, and n = number of inorganic octahedral layers. They are called "hybrid" materials because of the inclusion of both organic and inorganic moeities in the material. Studies on the three-dimensional perovskite family have shown correlations between restricted rotational motion of the organic cation and structural phase transitions, and electronic properties. However, several questions remain about the coupling between structure, optoelectronic properties, and organic cation dynamics in layered perovskites. Here, I show that the restriction of the organic cation dynamics influences the static inorganic structure. The relevant excited states that produce the observed white light emission are also impacted by the cation dynamics.

Chapter One is an overview of layered perovskites and how their structural diversity influences myriad properties. The excited state dynamics proposed in the literature are examined with respect to broad emission. Chapter Two goes in depth and describes the interplay between organic cation dynamics and broadband emission. Quasi-elastic neutron scattering elucidates the dynamic radii of the organic cation ammonium head groups and their role in tilting the inorganic octahedral structure. The smaller crystallographic

volumes resulting from restricted cation dynamics induces further out-of-plane octahedral tilting. This tilting gives rise to the observed white light emission by the formation of self-trapped excitons. The ammonium headgroup rotations happen on a time-scale that is faster than the recombination of the self-trapped excitons, providing multiple environments for the excited state to sample, leading to inhomogeneous broadening of the white light.

In perovskite derivatives, chemical substitution provides an opportunity to change the physical structure. Chapter Three demonstrates how changing the number of inorganic layers influences the cation dynamics. The methylammonium residence times, determined from quasi-elastic neutron scattering, are shorter in the layered perovskite with more inorganic layers. The dielectric screening provided by the increased number of methylammonium cations in the material with thicker inorganic enables the faster molecular motions to occupy larger crystallographic volumes.

The inorganic layer hosts the relevant frontier electronic states necessary for broad emission. The population of these frontier states is influenced by a number of factors, namely the out-of-plane tilt angle. Chemical substitution of the inorganic layer affects the out-of-plane tilting; therefore, it is necessary to control the tilt angle as a variable in order to determine a more direct correlation between cation dynamics and white light. Chapter Four discusses the effect of isotopic substitution of the organic cation as a way to understand the influence of dynamics independent of tilt angle. Calculations using a harmonic oscillator approximation show the deuteration of the ammonium headgroup is

closely coupled to the inorganic lattice, does not have much effect on the residence times of hydrogen motion.

Halide substitution in the three-dimensional perovskites leads to reduced organic cation rotation residence times and further correlates to changes in electronic properties. Neutron spectroscopy presented in Chapter Five demonstrates how substitution of the halide site influences the cation dynamics and broadband emission in layered perovskites. Materials with broad emission have a lesser extent of hydrogen rotational motion, which follows previous trends in the literature.

Chapter Six further demonstrates the effect of chemical substitution on broad emission and cation dynamics. The formation of solid solutions in the three-dimensional materials influence cation dynamics and phase transitions. White light emission at room temperature is achievable with solid solutions of layered perovskite derivatives. The extent of hydrogen motion determined from neutron scattering does not follow what is previously discussed in Chapter Two.

Cation dynamics modify the static inorganic structure and optoelectronic properties in complex, excited state-mediated pathways. The identity of the organic cation dictates the overall perovskite structure and influences the tilting of the octahedra. The cation dynamics influence the broad emission in layered perovskite derivatives. Characterization of these coupled behaviors enable design principles for solid-state lighting applications.

ACKNOWLEDGEMENTS

"Getting a PhD is kinda a big deal." - Kayla L. Keipe, best friend and court jester, 2022.

I don't think this document is long enough to thank all the people who have who have been instrumental to my success, not only as a scientist and graduate student, but also as a human along this journey; however, I am going to try.

I first want to thank my advisor, Prof. James Neilson. Jamie, thank you for hiring (and not firing) me. Thank you for letting me fail and learn, for your patience, sage advice, and stern words when they were needed. You've taught me that perovskite is always the answer, that I *can* do difficult things, and a healthy work-life balance is critical to my success and sanity.

Most of the advice I give to current Neilsonites is inherited from past members. Dr. Eve Mozur, Dr. Annalise Maughan, and Dr. Iain Oswald, thank you for your mentorship, constructive criticism, rubber-ducking, and questions. Neilsonites, you've all helped me learn more than I thought was possible.

The Prieto Group has been influencing me long before I became an honorary group member. My undergraduate advisor (and former Prieto Group member) Prof. Shannon Riha is to thank for my occupation of your office space, devouring of your group meeting snacks, and co-celebrations. Without her mentorship, encouragement, and letter of recommendation, I would have never applied to CSU or met any of you wonderful folks. I am so grateful to my adopted advisor, Amy Prieto, and the Prieto group members (past and present), so while the Neilson group has my head, know you all have my heart.

Kathy Lucas, Ron Costello: the department wouldn't - *couldn't* - run without you. Thank you for answering my thousands of administrative questions and helping me fix everything that keeps breaking.

Not only have I made a community within the Chemistry Department at CSU, but the support outside my graduate work has been instrumental in keeping me happy, healthy, and balanced.

I've had the pleasure of working at the Wolverine Farm Publick House. This space has provided respite from my windowless office and allowed me to romanticize at least part of my experience in graduate school. Ally, Thomas, Rafe, Fredo, and Leo: you've encouraged the creative when all that was expected was the technical. You've helped me nurture my voice as a poet and storyteller.

I am extremely grateful to the Welsh Rabbit, my weekly sanctuary and second home. Yak, Gussy, Turner, Connor, Will, and Emily: you are family. Thank you for my Thursday night Krasno, duck pasta, tarot readings, and laughter.

My numerous dance partners, namely Ana and Elad (who have been more teacher than partner) the literal blood, sweat, and tears doled out by your Thursday night lessons encouraged me to step outside my comfort zone and enabled me to build trust and connection I didn't know was possible.

I know I would not have made it through graduate school without my friendships and there are quite frankly too many to list. We became fast and lifelong friends thanks to this tumultuous journey that is graduate school, and if that is all I gain from my Ph.D.,

I can leave content. Thank you for being my support system. You are vast, loyal, and compassionate.

"True knowledge is only obtained by knowing what you do not know." The gaps in my knowledge have become painfully clear over the course of this chapter in my life; however, I'm finding more power in that idea as the chapter comes to a close. I couldn't have done this without my resilience, my confidence, and the support I've received over the course of the last decade. Thank you to everyone, including myself, for getting me this far. Now, only the unknown awaits.

TABLE OF CONTENTS

LIST OF FIGURES

1. Introduction

Since the invention of the first blue-light emitting diode (LED),[7] there have been advancements in white light emission that have transformed society. White light in commercial sources, such as an LED, is typically achieved in two ways; with a combination of red, green, and blue light emitters, or a phosphor coated blue-light emitter.[8,9] Thinner and more flexible options such as organic light-emitting diodes (OLEDs) and polymer light-emitting diodes (PLEDs) have opportunities to be introduced into TV screens, smart phones, and a variation of other display options.[10] While having more applications over their LED counterpart, OLEDs and PLEDs do not yet have long enough lifetimes or high enough efficiencies to compete commercially.[11] All these current technologies require multiple components and combining materials can lead to color temperature instability, low efficiencies, and variations in driving current and degradation rates.[9] Broad emission ($\approx$ 400 nm to $\approx$ 700 nm) from a single material is of interest to circumvent the issues that arise from current solid-state light technologies. Perovskites are a versatile semiconducting material with applications ranging from solar cells[12] to solid-state lighting applications.[13] The intrinsic nature of their white light emission makes them advantageous for applications in solid-state lighting.[14–16]

The chemical diversity of hybrid perovskites affords an array of optical responses accessible through compositional substitution.[14,17] The three-dimensional perovskite structure, ABX_3, is comprised of corner-connected [BX_6] octahedra with an (in)organic cation in the A-site (Figure 1.1). With the addition of a large organic cation (R-NH_3^+), the three-

dimensional structure is segregated into planes, where the inorganic octahedra are segregated by the large organic cations. This change in dimensionality is achieved through synthetic tuning of the perovskite in solution.[18,19]

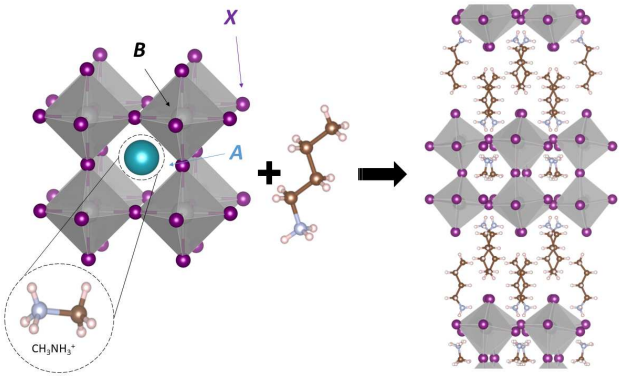

Figure 1.1: Crystal structures of (Left) the canonical ABX_3 (A = cesium, methylammonium, formamidinium, B = Sn, Pb, X = Cl, Br, or I) perovskite. The inorganic cage is comprised of $[BX_6]$ octahedra, and the (in)organic cation sits in the A-site void. (Right) With the addition of a large R-NH_3^+ containing cation (shown here is n-butylammonium, $C_4H_{12}N$) the inorganic layers split and the $(A')_2(A)_{n-1}B_nX_{3n+1}$ structure is formed where A' = large R-NH_3^+ containing cation, A = small organic cation, B = metal, X= halide.

White light emission from these layered perovskites is proposed to arise from the recombination of a self-trapped exciton.[2,16] Excitons are coulombically bound electron-hole pairs that are either delocalized (free) or localized (self-trapped) within the inorganic layer.[20,21] A self-trapped exciton (STE) is a stabilization of the free exciton (FE) excited state (Figure 1.2). The optical deformation potential (ODP) is a microscopic mechanism used to describe the formation of an STE and the observed broad emission. The compression and dilation of a single octahedron couples to the excited state, leading to the STE manifold (blue dotted line, Figure 1.2). As the relevant electronic states, specifically the self-trapped exciton, reside in the inorganic layer of layered perovskites, it is important to fully understand the influence of the inorganic layers on the observed optoelectronic properties.

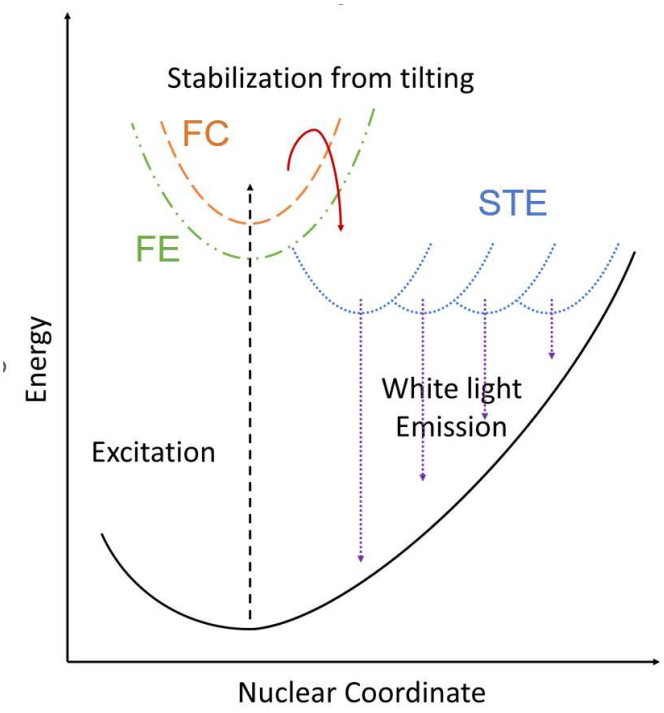

Figure 1.2: Schematic of potential energy diagram demonstrating the process by which self-trapped excitons produce broadband emission. Excitation from the ground state (black solid line), promotes electrons and holes to free carriers (FC, orange dashed line). The free carriers are then stabilized as free excitons (FE, green dashed and dotted line) through high exciton binding energies inherent to these materials. The tilting of the inorganic octahedra stabilize the free-excitons to self-trapped excitons (STE, blue dotted line).

The thickness of the inorganic layer alone influences the overall band gap and emission,[19] exciton binding energies,[3,19] carrier mobility and lifetimes,[3] and extent of octahedral tilting.[22] The out-of-plane tilting has the greatest effect on the intensity of broadband photoluminescence,[1,23] and the tilting of the inorganic octahedra reduce the overall bandwidth of the exciton and increase the ODP,[2] ultimately facilitating self-trapping. As previously mentioned, out-of-plane tilt stabilizes the excited state, and the inorganic layer tilting is dictated by the choice of organic cation.

The organic cation templates the overall structure of hybrid halide perovskites.[1,19,24,25] As the cation choice is a key factor in the overall perovskite structure, and thus the properties, it stands to investigate them thoroughly. The relevant electronic states reside in the

inorganic layer; therefore, the interactions between the organic cation and the inorganic layer are of greatest interest. The dynamics of the organic cations have been studied by means of molecular dynamics simulations,[22,26] nuclear magnetic resonance (NMR),[27] inelastic,[27,28] and quasi-elastic[4,5,28–30] neutron scattering. In this dissertation, I investigate the rotational dynamics of ammonium-containing cations within layered hybrid perovskite derivatives. I demonstrate that the structural reorientation of the inorganic structure upon photoexcitation is attributed to the rigidity of the organic spacer cation. With a further understanding of the organic cation dynamics, these fundamental principles can lead to improved design principles with regard to white light emission.

Chapter two focuses on single layer A_2PbBr$_4$ (A = R-NH$_3^+$) hybrid halide perovskite derivatives. Using quasi-elastic neutron scattering, I have found the large dynamic radius of a mobile cation occupies a larger octahedral void. Conversely, an organic cation with restricted dynamics occupies a smaller octahedral volume within the crystallographic A-site void. The apical halogens tilt in order to compensate for the lack of positive charge. This tilting induced by restricted cation dynamics leads to the observed broad emission. Time-resolved photoluminescence reveals a single-ensemble-like emission. The organic cation rotational motion is on faster timescales than exciton relaxation; therefore, the excited state can sample multiple environments. This sampling provides a mechanism to inhomogeneously broaden the white light spectrum.

Chapter three investigates the multi-layer ($d-n$BA)$_2$(MA)$_{n-1}$Pb$_n$I$_{3n+1}$ (nBA = n-butylammonium, MA = methylammonium, n = 2, 3) family of perovskite derivatives. The rotational motion of MA in the 3D derivatives is influenced by phase

transitions of the static crystal structure and influences carrier mobility and lifetimes. In the layered materials, I have found the restriction of the C_4 rotation of MA correlates to phase transitions and time-resolved microwave conductivity signals. The influence of dimensionality on the rotational dynamics provides further fundamental understanding of dynamics-structure-property relationships.

While Chapters two and three focus on changing the overall structure of the material, Chapter four explores the effect of isotopic substitution in layered perovskite derivatives. Changing the organic cation that sits in the A-site void can influence tilt angle and optoelectronic properties; therefore, by eliminating tilt angle as a variable with isotopic substitution, we can more directly compare the cation dynamics and properties. Preliminary calculations and photoluminescence data show the deuteration of the ammonium head group will have little effect on the overall dynamics. While the dynamics are not significantly affected, the narrow and broad emissions are still influenced.

Chapter five describes the influence halide substitution has on organic cation dynamics in the $(n\text{BA})_2\text{Pb}X_4$ (X = Cl, Br, I) family of layered perovskites. Fixed-window elastic neutron scattering experiments correlate a lesser extent of hydrogen motion to the materials that emit broadband white light (Cl, I congers). The hydrogen dynamics also coincide with phase transitions observed by differential scanning calorimetry. However, further studies are necessary to reach definitive conclusions about the coupling of halogen vibrational dynamics and organic cation rotational motion.

Chapter six studies the dynamics of organic cation rotational motion within solid-solutions. Solid-solutions of $(\text{BZA})_2\text{PbCl}_{4-x}\text{Br}_x$ (BZA = benzylammonium) can emit white

light at room temperature, which is advantageous for solid-state lighting applications. The tilt angle is influenced through halide substitution and studies on the three-dimensional perovskite $MAPbI_xCl_{1-x}$ show the halide substitution and mixing can influence organic cation dynamics and properties. Here, preliminary data is reported on the solid-solution series, $(BZA)_2PbCl_{4-x}Br_x$.

The final chapter discusses future experiments and remaining open questions in the field of layered hybrid perovskites with respect to the organic cation dynamics. I propose a deeper understanding of the organic cation dynamics in hybrid halide perovskites will illuminate the underlying mechanisms by which the optoelectronic properties occur. This fundamental understanding will provide design principles for new perovskite-based materials.

2. Correlating Broadband Photoluminescence with Structural Dynamics in Layered Hybrid Halide Perovskites [†]

2.1. Summary

The emission of white light from a single material is atypical and is of interest for solid-state lighting applications. Broadband light emission has been observed in some layered perovskite derivatives, A_2PbBr$_4$ (A = R-NH$_3^+$), and correlates with static structural distortions corresponding to out-of-plane tilting of the lead bromide octahedra. While materials with different organic cations can yield distinct out-of-plane tilts, the underlying origin of the octahedral tilting remains poorly understood. Using high energy resolution (e.g., quasi-elastic) neutron scattering, this contribution details the rotational dynamics of the organic cations in A_2PbBr$_4$ materials where A = n-butylammonium (nBA), 1,8-diaminooctammonium (ODA), and 4-aminobutyric acid (GABA). The organic cation dynamics differentiate (nBA)$_2$PbBr$_4$ from (ODA)PbBr$_4$ or (GABA)$_2$PbBr$_4$ in that the larger

[†]Reproduced with permission from Koegel, A. A., Mozur E. M., Oswald, I. W. H., Jalarvo, N. H., Tyagi, M., Prisk T. R., Neilson J. R. Correlating Broadband Photoluminescence with Structural Dynamics in Layered Hybrid Halide Perovskites *J. Am. Chem. Soc.* **2022**, 144, 3, 1313-1322, https://pubs.acs.org/doi/abs/10.1021/jacs.1c11217. Copyright 2022 American Chemical Society.
Author contributions: Alexandra Koegel prepared the samples, collected and analyzed the neutron scattering, X-ray diffraction, photoluminescence, differential scanning calorimetry data, and prepared the manuscript. Eve Mozur collected neutron diffraction data. Iain Oswald collected neutron diffraction data. Niina Jalarvo, Timothy Prisk, and Madhusudan Tyagi collected and analyzed neutron scattering data. James Neilson edited the manuscript and oversaw the project.

spatial extent of dynamics of nBA yields a larger effective cation radius. The larger effective volume of the nBA cation in $(n\text{BA})_2\text{PbBr}_4$ yields a closer to ideal A-site geometry, preventing the out-of-plane tilt and broadband luminescence. In all three compounds, we observe hydrogen dynamics attributed to rotation of the ammonium head group and at a timescale faster than the white light photoluminescence studied by time-correlated single photon counting spectroscopy. This supports a previous assignment of the broadband emission as resulting from a single ensemble, such that the emissive excited state experiences many local structures faster than the emissive decay. The findings presented here highlight the role of the organic cation and its dynamics in hybrid organic-inorganic perovskites and white light emission.

2.2. Introduction

Efficiently generating artificial white light for indoor lighting applications remains a challenge. White light (i.e., broadband) emission is typically achieved through the mixing of phosphors with dopants that each have a narrow emission spectrum such as a light emitting diode (LED) or diode laser.[31,32] While there are benefits to this established technology, intrinsic broadband emission in a single material, while unusual, would greatly simplify device implementation and engineering. Several layered hybrid organic-inorganic halide perovskites exhibit intrinsic broadband emission,[1,15,16,33] such as the lead halide based Ruddlesden-Popper type layered perovskite derivatives with the general formula $A_2\text{PbBr}_4$ (A = large ammonium-containing cation, and X = a halide) shown in Figure 2.1.

These “layered” structures are known for their high exciton binding energies from the quantum-well-like electronic structure, which typically results in the energetically-narrow emission from free excitons. The observed broadband emission in these materials has been attributed to both extrinsic and intrinsic self-trapped excitons (STEs), where the crystal structure deforms around and stabilizes the exciton.[1,3,15,16,34,35] This “self-trapping” is to distinguish the broadened emission from that of an exciton that interacts strongly with defect states. A mechanism that captures the primary features of STE formation and broadband photoluminescence is the interaction of an exciton with a highly localized optical phonon by way of the optical deformation potential (ODP).[2] In short, swelling and reduction of the inorganic layer from the breathing of single octahedron yields a separate excited state manifold for the STE that produces a broad emission spectrum. The broadband emission of (EDBE)$PbBr_4$ (EDBE = 2,2’-(ethylenedioxy)bis(ethylammonium)) results from a single ensemble of states, as the broadband spectrum decays uniformly in time.[36] Understanding the materials chemistry that leads to this behavior is key to tuning the emission.

Multiple factors influence the broadband emission in hybrid halide materials. For intrinsic broadband emission in layered Pb-*X* perovskite derivatives, this includes: the number of inorganic layers,[2,3] the choice of organic spacer cation,[26] and out-of-plane octahedral tilt angle (i.e., deviation from the 180° Pb-*X*-Pb bond angle).[1,37–40] The out-of-plane tilt angle is particularly sensitive to the nature of the organic spacer cations,[1] thus providing compositional control over broadband emission.[1,26] While studies have attributed broadband emission to enhanced exciton-phonon coupling that occurs from out-of-plane

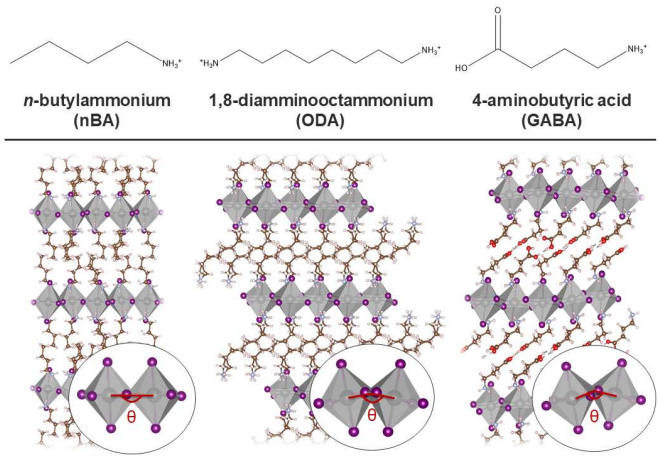

Figure 2.1: Crystal structures of lead bromide based layered perovskite derivatives for (left) $(n\text{BA})_2\text{PbBr}_4$, (middle) $(\text{ODA})\text{PbBr}_4$, and (right) $(\text{GABA})_2\text{PbBr}_4$ where nBA = n-butylammonium, ODA = 1,8-diaminooctammonium, and GABA = 4-aminobutyric acid. The schematics illustrate the cations used in this study and the arrangement of the cations in the organic layer between single layers of octahedra. The insets highlight the out-of-plane tilting attributed to the observed broadband emission.[1,2] Where the tilt angles for the compounds are $(n\text{BA})_2\text{PbBr}_4$ = 3.9°, $(\text{ODA})\text{PbBr}_4$ = 19°, $(\text{GABA})_2\text{PbBr}_4$ = 23.9°. Lead is in grey, bromide in purple, carbon in brown, nitrogen blue, and hydrogen in pink.

tilting templated by the organic cations,[35] little is understood if and how the motion of the organic moiety contributes to the observed broadband emission in hybrid halide materials.

To gain insight into the role and magnitude of the organic cations' dynamics and how they may influence broadband emission, this study describes the molecular dynamics of the organic cations of three layered hybrid perovskites $(n\text{BA})_2\text{PbBr}_4$, $(\text{ODA})\text{PbBr}_4$, and $(\text{GABA})_2\text{PbBr}_4$, where nBA = n-butylammonium, ODA = 1,8-diaminooctammonium, and GABA = 4-aminobutyric acid (Figure 2.1) using quasi-elastic neutron scattering (QENS). The spatial extent of the cation dynamics illustrates how the organic cations influence out-of-plane octahedral tilt angles, where $(n\text{BA})_2\text{PbBr}_4$ = 3.9°, $(\text{ODA})\text{PbBr}_4$ = 19°, $(\text{GABA})_2\text{PbBr}_4$ = 23.9°, such that out-of-plane tilting is required for broadband emission at low temperatures.[1] The effective dynamical radius of the ammonium head group appears to influence the A-site volume and tilt angle of the inorganic layer. Cations with more

restricted spatial motion of the ammonium group create a smaller A-site volume, thus yielding a larger out-of-plane octahedral tilt angle (ODA and GABA). Furthermore, the fast timescale of the ammonium headgroup rotation relative to the emissive decay studied by time-resolved photoluminescence experiments, provides myriad local structures for the excited state ensemble(s) to sample, thus yielding a large degree of inhomogeneous broadening to the emission. These results elucidate the interplay between organic cation dynamics and optoelectronic properties in layered hybrid halide perovskite derivatives.

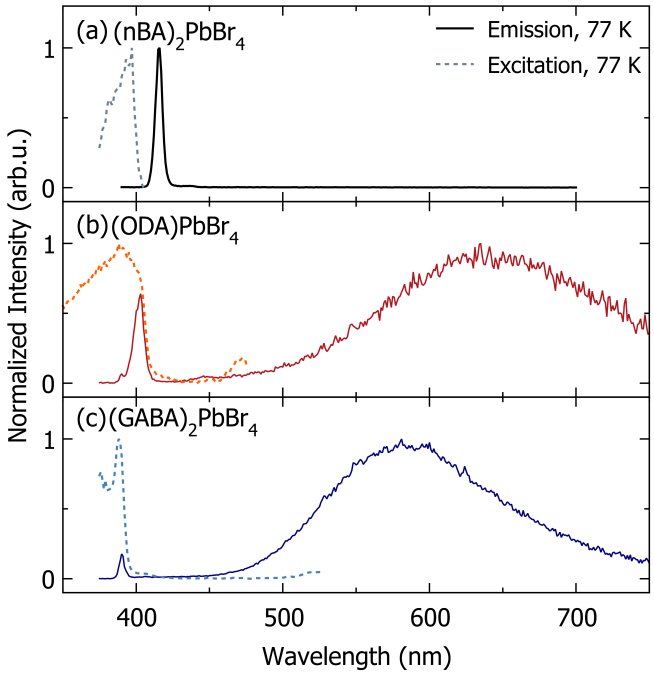

Figure 2.2: Low temperature (77 K) normalized photoluminescence spectra from excitation at 375 nm (solid lines) showing a narrow emission peak near 400 nm and (a) no or (b,c) broad emission centered near 600 nm. Also shown are excitation spectra (dotted lines) of (a) $(n\text{BA})_2\text{PbBr}_4$ (black) monitoring emission at 415 nm, (b) $(\text{ODA})\text{PbBr}_4$ (red) monitoring emission at 607 nm, and (c) $(\text{GABA})_2\text{PbBr}_4$ (blue) monitoring emission at 553 nm).

2.3. Experimental

All syntheses were performed in air at room temperature. Materials were used as received from the manufacturer. Acronyms used: nBA = n-butylammonium, ODA = 1,8-diaminooctammonium, and GABA = 4-aminobutyric acid. The starting $PbBr_2$ concentrations were determined from the molar solubility of the desired product in order to maximize yield and purity.[18]

Preparation of (nBA)$_2$PbBr$_4$: A 0.301 M solution of $PbBr_2$ was prepared by the addition of 0.689 g (3.08 mmol) PbO in 10 mL aqueous HBr (48 wt% aqueous, Alfa Aesar). To this solution, 0.610 mL (6.17 mmol) n-butylamine (Sigma Aldrich) was titrated dropwise and stirred for 20 minutes, yielding an opaque, white, microcrystalline powder. The precipitate was collected by vacuum filtration and washed with glacial acetic acid (Fisher Chemical, Certified ACS) then hexanes (Fisher Chemical, Certified ACS) and dried in air for 30 min. Phase purity was confirmed by powder X-ray diffraction. 84.1 % yield based on lead content.

Preparation of (ODA)PbBr$_4$: A 0.089 M solution of $PbBr_2$ was prepared by the addition of 0.192 g (0.860 mmol) PbO in 10 mL aqueous HBr (48% aqueous, Alfa Aesar). To this solution, 0.127 mL (0.860 mmol) 1,8-diaminooctane (Sigma Aldrich, molten via heat gun) was titrated dropwise and stirred for 20 minutes, yielding an opaque, white, microcrystalline powder. The precipitate was collected by vacuum filtration and washed with glacial acetic acid (Fisher Chemical, Certified ACS) then hexanes (Fisher Chemical, Certified ACS) and dried in air for 30 min. Phase purity was confirmed by powder X-ray diffraction. 70.6%

yield based on lead content.

Preparation of $(GABA)_2PbBr_4$: A 0.689 M solution of $PbBr_2$ was prepared by the addition of 1.52 g (6.81 mmol) PbO in 10 mL aqueous HBr (48% aqueous, Alfa Aesar). To this solution, 1.41 g (13.6 mmol) of 4-aminobutyric acid (Alfa Aesar) was added and stirred for 20 minutes. 6 mL of glacial acetic acid (60% of the total vol, Fisher Chemical, Certified ACS) was then added to the solution and let stir for a further 20 minutes, yielding opaque, white, plate-like crystals. The precipitate was collected by vacuum filtration and washed with hexanes (Fisher Chemical, Certified ACS) and dried in air for 30 min. Phase purity was confirmed by powder X-ray diffraction. 47.0% yield based on lead content.

Photoluminescence (PL): Steady state photoluminescence data were collected on a Edinburgh FS5 spectrofluorometer using a monochromated 150W Xenon lamp with slit bandwidths of 1 nm. Samples were prepared by packing powdered samples into 250 mm x 4 mm Thin Wall Quartz EPR sample tubes and inserting the sample tube into liquid nitrogen. The samples were excited with 375 nm light and monitored over a spectral range of 400-650 nm. Background data collection was collected on an empty EPR tube excited at 375 nm and monitored over a spectral range of 325-675 nm. Time correlated single photon counting (TPSPC) photoluminescence transients were collected on an Edinburgh FS5 spectrofluorometer using a 365 nm laser diode with a 5.00 nm slit bandwidth and SC-70: Liquid Nitrogen EPR Dewar sample stage. Light was pulsed at 500 ns intervals and collected at various wavelengths across the broad spectrum. Decay lifetimes were calculated with Fluoracle software using the biexponential equation: $R(t) = B_1 \exp(-t/\tau_1) + B_2 \exp(-t/\tau_2)$. The transients except those emitted at 624 nm and 650 nm of $(GABA)_2PbBr_4$ were best fit

with a biexponential model. The transients emitted at 624 nm and 650 nm were fit with a single exponential model.

Differential Scanning Calorimetry (DSC): Differential scanning calorimetry (DSC) data were collected on a TA Modulated DSC 2500 with a sub-ambient accessory. Roughly 5 mg of each compound were sealed in Tzero Aluminum Hermetic pans. Samples were cycled at 10.0 °C/min from room temperature to -90.0° C (183 K), allowed to equilibrate, and ramped at 10.0° C/min to 0.0° C (273 K) and allowed to equilibrate. This cycle was repeated three times. Features visible from 175 K to 225 K are also visible in any empty, hermetically sealed sample pan.

Powder X-ray diffraction (PXRD): Laboratory powder X-ray diffraction data were collected on a Bruker D8 Discover DaVinci powder X-ray diffractometer using Cu Kα radiation and a Lynxeye XE-T position-sensitive detector. Samples were prepared on a "zero-diffraction" Si wafer. The PXRD data were modeled with space groups of *Pbca* for (nBA)$_2$PbBr$_4$, $P2_1/c$ for (ODA)PbBr$_4$, and $P2_1/c$ for (GABA)$_2$PbBr$_4$ using previously reported structures[1] with the Rietveld method implemented in TOPAS v6 (Bruker AXS). VESTA was used to render crystal structures and to compute polyhedral volumes of experimental crystal structures.[41]

Fixed-window Elastic Neutron Scattering: Fixed window elastic scattering data were collected using the high-flux backscattering spectrometer (HFBS) at the NIST Center for Neutron Research on non-deuterated samples of (nBA)$_2$PbBr$_4$, (ODA)PbBr$_4$, and (GABA)$_2$PbBr$_4$.[42] At HFBS, the sample environment employed in this fixed-window experiment is a closed-cycle refrigerator that cools or warms the sample by helium exchange gas.

Masses of 0.917 g of $(n\text{BA})_2\text{PbBr}_4$, 0.661 g of (ODA)$\text{PbBr}_4$, and 0.853 g of $(\text{GABA})_2\text{PbBr}_4$ were used for this experiment. The cylindrical sample cell has a diameter of approximately 3 cm, and the powder sample was held against the lateral area of the sample can by enclosing it within aluminum foil pouches. The sample cell was loaded in a helium glove box and sealed with an indium O-ring. The enclosed helium ensures good thermal contact between the powder and the rest of the sample environment.

Initially, the samples were loaded into the instrument at 295 K and cooled to 5 K. Data were continuously collected at a ramp rate of 0.8 K/min with 60 sec/point. Finally, data were collected upon heating at the same nominal ramp rate and time per point. The observed scattering was normalized to the incident beam monitor. A fixed window scan is a measurement of the elastic intensity $I_{el}(Q,T)$ as a function of Q, momentum transfer, and temperature. The effective mean-squared displacement, $\langle u^2 \rangle$, of the hydrogen atoms is estimated by assuming that $I_{el}(Q,T)$ is governed by a Debye-Waller factor: $I_{el}(Q,T) = I_{el}(Q, T = 5.0\,\text{K}) \cdot \exp(-Q^2\langle u^2 \rangle/3)$.[43,44] The effective mean-squared displacement quantifies the extent of motion of the hydrogen atoms. This calculation was performed using the DAVE software.[45] Given the elastic energy resolution of 0.8 μeV on HFBS, the experimental time window is approximately 1.6 ns; motions slower than this cannot be distinguished from the static structure.

Quasi-elastic Neutron Scattering (QENS): QENS experiments were performed at the backscattering spectrometer BASIS at the Spallation Neutron Source, Oak Ridge National Laboratory and HFBS at the NIST Center for Neutron Research.[42,46] At BASIS, the center wavelength of the incident neutron beam was 6.4 Å with 60 Hz operation of the pulsed

source using the Si(111) analyzers, which yields a full width half-maximum of the energy resolution at the elastic line of 3.5 μeV over the accessible momentum transfer range Q = 0.2 to 2.0 Å^{-1}. The relaxation times were calculated from HWHM$_{\text{Lorentzian}} = \hbar/\tau$. Time-of-flight data were reduced in MANTID.[47]

The HFBS spectrometer operates with a monochromatic neutron beam with a wavelength of 6.271 Å over a Q range of 0.25 to 1.75 Å^{-1}. Data were reduced in DAVE.[45] At HFBS, vanadium spectra collected at T = 295 K were used as the IRF. At BASIS, the IRF was determined by measuring the sample itself but at base temperature (T = 20 K). Sample powders were packed in aluminum foil packets and placed in an annular aluminum cylindrical can. Sample amount yielding approximately 95% transmission of the beam was used, which minimizes multiple scattering events with the annular geometry. HFBS spectra were fit in DAVE[45] and BASIS spectra were fit in QClimax[48] in order to extract the Elastic Incoherent Structure Factor (EISF). The function: EISF $= I_{\text{elastic}}/(I_{\text{elastic}} + I_{\text{quasi-elastic}})$ was used to describe the magnitude of the QENS component where *I* is the integrated intensity of the respective elastic or quasi-elastic scattering. Spectroscopic QENS spectra were fit with an IRF, linear background, and Lorentzian functions (Figure 2.5). The experimental IRFs convolved with a δ-function centered at zero energy describe the elastic scattering while Lorentzian functions convolved with the IRF describe the quasi-elastic components. Additional Lorentzian components were added when the fit of a single Lorentzian was not sufficient to describe the data. Detector group 1 ((Q = 0.3 Å^{-1}) encompasses coherent, Bragg reflections in all samples and was removed. Additionally, detector groups 6 (Q = 1.3 Å^{-1}), 7 (Q = 1.5 Å^{-1}), 8 (Q = 1.7 Å^{-1}), and 9 (Q = 1.9 Å^{-1}) encompass coherent, multi-

ple scattering that produce elastic intensity not accounted for in the EISF; therefore, these Q-ranges were removed for all samples collected at BASIS. Detector groups 5 (Q = 0.619 Å^{-1}), 7 (Q = 0.870 Å^{-1}), 10 (Q = 1.216 Å^{-1}), 12 (Q = 1.420 Å^{-1}), 15 (Q = 1.676 Å^{-1}), and 16 (Q = 1.748 Å^{-1}) were removed for (nBA)$_2$PbBr$_4$ at 150 K EISFs to avoid contributions from coherent scattering collected at HFBS. Jump models of the molecular dynamics were fit to the EISFs, as described in the results section. These analyses implemented in python are provided as supplemental material.

2.4. Results

Solution precipitation yields (nBA)$_2$PbBr$_4$, (ODA)PbBr$_4$, and (GABA)$_2$PbBr$_4$ consistent with prior studies. In preparation for neutron scattering studies, $>$1 g of each material was prepared and yielded phase pure materials, as characterized by powder X-ray diffraction (Figure 13) and ambient temperature absorption and photoluminescence spectroscopy (Figure 2) in agreement with a previous study.[1] The photoluminescence spectra at T =77 K shown in Figure 2.2 consists of a single narrow emission peak centered near 400 nm for all compounds, consistent with the presence of free excitons. In (ODA)PbBr$_4$ and (GABA)$_2$PbBr$_4$, we observe broad emission peaks centered around 630$\pm$80 nm and 580$\pm$70 nm respectively (range refers to the full-width-at-half maximum), consistent with the previous characterization of photoluminescence from self-trapped excitons. This differs from the room-temperature data (Figure 2) in that none of the materials have broadband emission above 200 K.[1] This has been attributed to the depopulation of trapped excitonic states, as there is enough thermal energy to detrap carriers.[2] The excitation spectra in Fig-

ure 2.2 corresponding to the centers of the broadband emission illustrate that excitation of the free exciton or interband transitions gives rise to the broad emission (dashed lines, Figure 2.2), providing additional evidence for attributing these spectral features to self-trapped excitons. These specimens were used for further analysis by neutron scattering.

Mean-squared displacements (MSD) for $(n\text{BA})_2\text{PbBr}_4$, (ODA)$\text{PbBr}_4$, and $(\text{GABA})_2\text{PbBr}_4$ were calculated from fixed-window elastic scattering and quantify the extent of hydrogen motion from 5 K to 300 K (Figure 2.3), based on a Debye-Waller approximation. After normalization of the MSD trends to their values at the lowest temperatures, $(n\text{BA})_2\text{PbBr}_4$

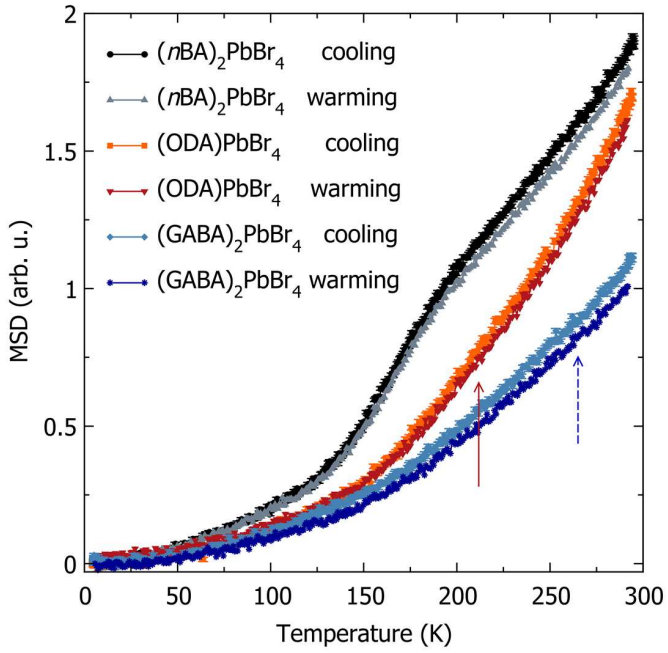

Figure 2.3: Mean squared displacements of $(n\text{BA})_2\text{PbBr}_4$ (black circles for cooling, grey triangles for warming), (ODA)PbBr_4 (red squares for cooling, red down triangles for warming), and $(\text{GABA})_2\text{PbBr}_4$ (blue diamonds for cooling, dark blue stars for warming) collected in the temperature range from 5 K to 300 K. MSD values are calculated from fixed-window elastic neutron scattering experiments (NIST, HFBS). Red solid and blue dashed vertical arrows indicate phase transitions detected from differential scanning calorimetry of (ODA)PbBr_4 and $(\text{GABA})_2\text{PbBr}_4$, respectively (Figure 2.4). No abrupt transitions are visible in the MSD. Error bars are smaller than the data point symbols. Error bars throughout the text represent one standard deviation.

exhibits the greatest extent of hydrogen motion at elevated temperatures (e.g., higher MSD) while $(GABA)_2PbBr_4$ exhibits the least.

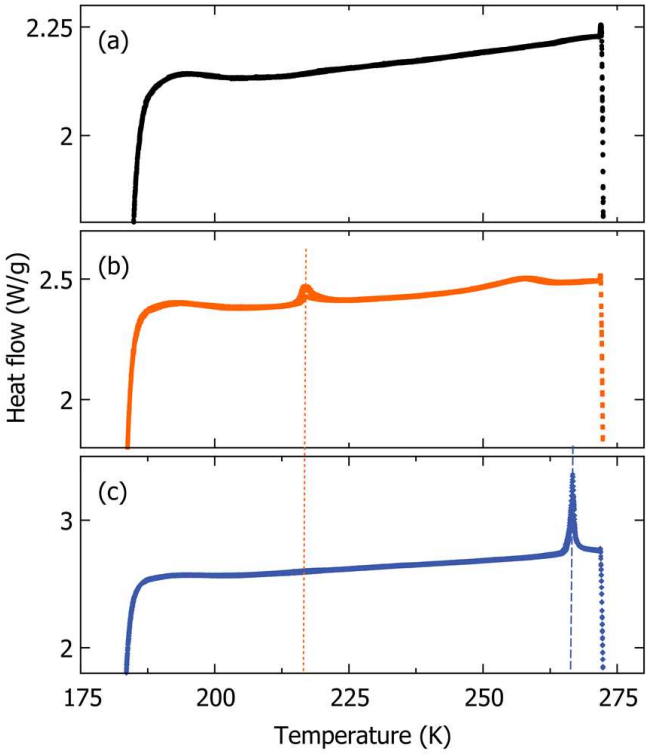

Figure 2.4: Differential scanning calorimetry (Heat flow, W/g) heating curves of (a) $(n\text{BA})_2PbBr_4$ (black circles), (b) $(ODA)PbBr_4$ (red squares, red dotted line indicates a phase transition at 215 K), and (c) $(GABA)_2PbBr_4$ (blue diamonds, blue dotted line indicates a phase transition at 265 K) from 175 K to 285 K.

The extent of hydrogen motion in the organic cations presented here is not influenced by phase transitions. Differential scanning calorimetry (DSC) data shown in Figure 2.4 show phase transitions of $(ODA)PbBr_4$ and $(GABA)_2PbBr_4$ at 215 K and 265 K, respectively. However, the MSD data do not qualitatively depict any anomalies above 150 K (Figure 2.3). The observation of phase transitions in DSC without significant discontinuities in the MSD suggest that the extent of hydrogen motion of the organic cations are not significantly affected by small changes in the inorganic framework associated with the phase transitions (e.g., octahedral tilt angles). This contrasts materials such as $(CH_3NH_3)PbX_3$

and $(CH(NH_2)_2)PbX_3$ (X = halide), in which the phase transitions are accompanied by significant changes to the molecular dynamics.[27,28,49,50]

The spatial extent of the organic cation dynamics decreases with decreasing temperature. QENS is most sensitive to the reorientations of hydrogen on μeV energy scales in nBA, ODA, and GABA owing to the large scattering cross section of hydrogen (82.02 barns) relative to the other elements (Pb = 11.118 barns, Br = 5.9 barns, C = 5.551 barns, and N = 11.53 barns; all natural abundance).[51] However, the temperature-dependent behavior does not follow classical thermally-activated motion defined by an Arrhenius relationship (see Supporting Information for a full discussion), as is also observed for $(C_8H_{17}NH_3)_2PbI_4$.[5] Quasi-elastic scattering at high temperatures reveals at least two relaxation times, as a fit to the data requires multiple Lorentzian functions (Figure 2.5(a)). At lower temperatures, the data are well described by a single relaxation (e.g., one Lorentzian), as illustrated in Figure 2.5(b).

QENS of $(n\text{BA})_2PbBr_4$ shows a larger spatial extent and shorter relaxation time of the organic cation dynamics relative to the other compounds which is in agreement with the higher MSD observed over the temperature range. QENS measurements indicate that ODA and GABA have longer relaxation times overall at lower temperatures ($T < 200$ K) relative to nBA, which has detectable QENS at all measured temperatures (Figure 5). Additionally, modeling of the QENS data indicate ODA and GABA have a smaller extent of hydrogen motion than nBA, as described below.

From the QENS data we calculate an elastic incoherent structure factor (EISF) to quantify the spatial extent of the organic cation dynamics using a jump model.[5,29,52] Qualitative

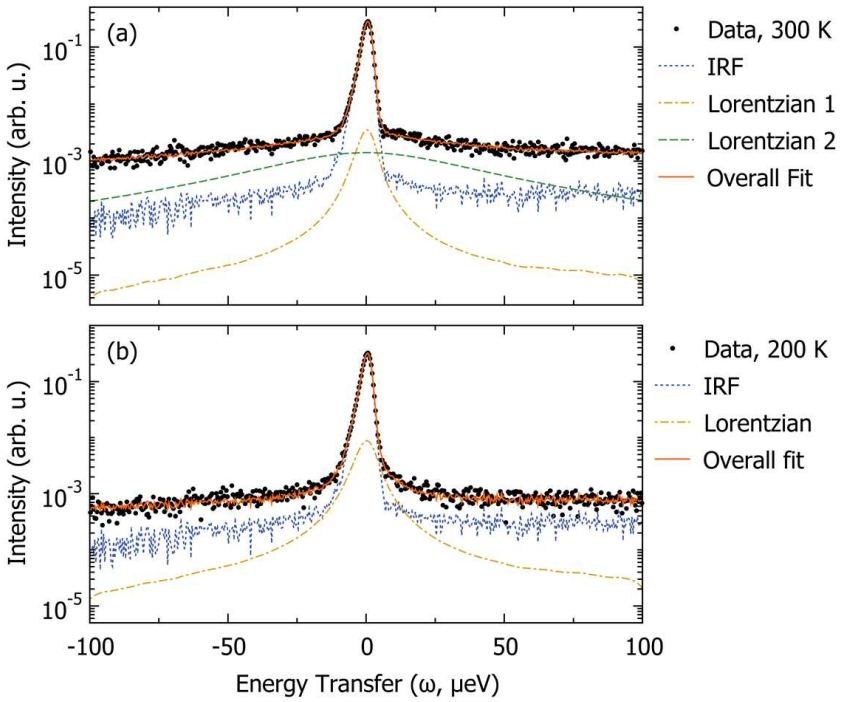

Figure 2.5: Quasi-elastic neutron scattering (ORNL, BASIS) at (a) 300 K (b) 200 K for $(n\text{BA})_2\text{PbBr}_4$. The representative spectra (Q = 0.9 Å^{-1}) are shown as black circles, with the overall fit shown as a solid orange line. The overall fit includes all functions used to describe the data. The instrument resolution function (IRF) collected for each sample at T = 20 K is convolved with a delta function and accounts for elastic scattering, shown here as a blue dotted line. The broadening from quasi-elastic scattering is fit with a Lorentzian function, shown as yellow dashed and green dash-dotted lines. At 300 K, multiple relaxations are required to describe the data (e.g., at least 2 Lorentzians), whereas at 200 K, only one relaxation is required. Note the logarithmic scale on the y-axis.

analysis of the EISF and the molecular conformation of the organic cations observed in the crystal structure illustrates that nBA has the greatest extent of hydrogen motion based on the steeper Q-dependent decay of the EISF (i.e., greater quasi-elastic scattering contribution), as illustrated in Figure 2.6(a). GABA has the least extent of hydrogen motion, as inferred from the gradual decay of the EISF as a function of Q (Figure 2.6(c)). The greater extent of quasi-elastic scattering in nBA compared to ODA and GABA in the EISF bolster the greater extent of spatial motion assessed from the fixed window elastic scattering (Figure 2.3) and agrees with the volume of the A-site void calculated from the crystallographic information below.

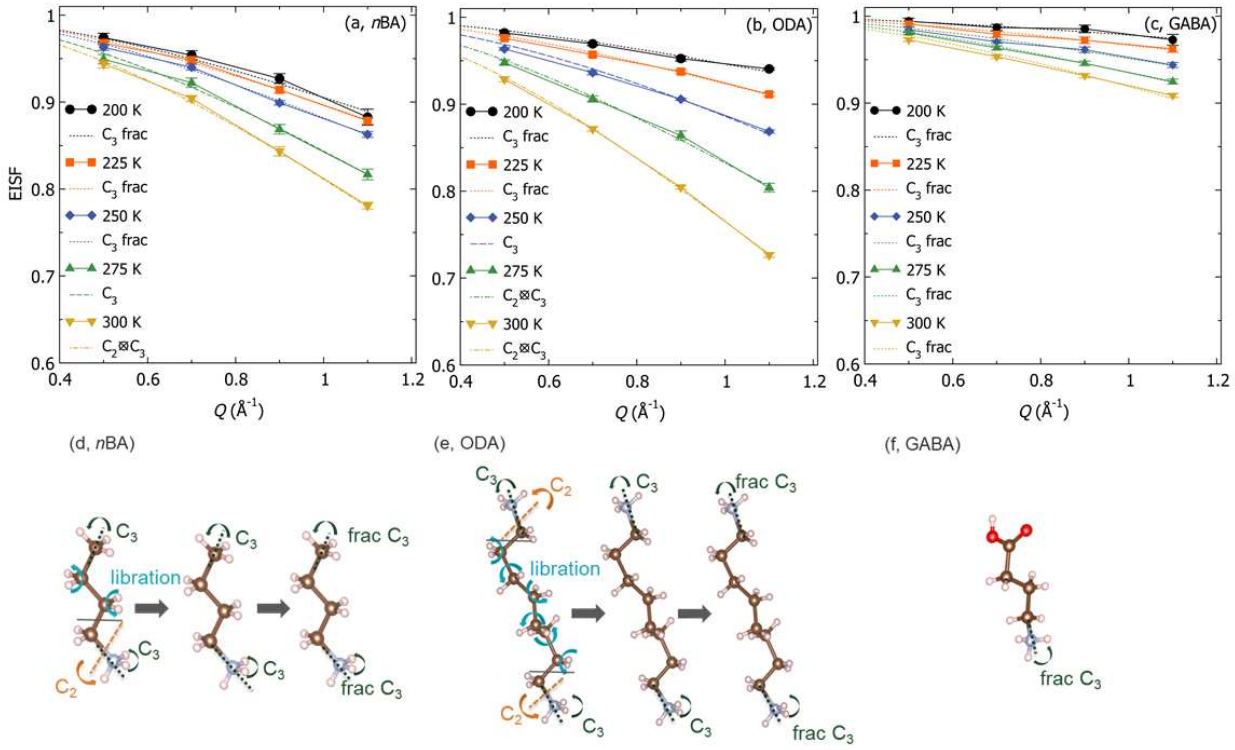

Figure 2.6: Elastic incoherent structure factors of (a) $(n\text{BA})_2\text{PbBr}_4$, (b) (ODA)$\text{PbBr}_4$, and (c) $(\text{GABA})_2\text{PbBr}_4$ from 200 K $\leq T \leq$ 300 K extracted from QENS data (ORNL, BASIS) and fit by jump models describing $C_2 \otimes C_3$ rotations (dot-dashed), C_3 rotations (dashed), and fractional C_3 rotations (dotted), as described in the narrative. Cartoons depicting the cation motions are illustrated for (d) $(n\text{BA})_2\text{PbBr}_4$, (e) (ODA)$\text{PbBr}_4$, and (f) $(\text{GABA})_2\text{PbBr}_4$. Error bars represent one standard deviation.

The temperature-dependent EISFs for each material are well described by a series of jump models partially constrained by molecular and crystallographic site point group symmetries. An extended discussion of alternative models and best fit parameters can be found in the Supplemental Information (see Figures 7 - 10, and Table 2). For all three compounds, the EISF decreases with decreasing temperature as they lose thermal energy. The cartoons in Figure 2.6(d) illustrate rotations of different functional groups and the overall temperature-dependent progression for $(n\text{BA})_2\text{PbBr}_4$. Unlike ODA and GABA, nBA does not bridge across two inorganic layers through non-covalent interactions. Specifically, at T = 300 K, the nBA cation undergoes multiple rotations, consistent with a model adopted for

$(C_8H_{17}NH_3)_2PbI_4$.[5] One motion is the direct product of $C_2 \otimes C_3$ rotations for the $-CH_2NH_3$ head group, such that the ammonium cation experiences the full $C_2 \otimes C_3$ motion, but the α-carbon only experiences the C_2 motion. The methyl group undergoes a C_3 motion, while librations of other aliphatic $-CH_2-$ hydrogens are modeled as pseudo-C_2 rotations. At T $<$ 300 K, this full model cannot accurately describe the data for $(n\text{BA})_2PbBr_4$. Instead, the data are modeled with temperature-dependent restricted C_3 motion ('C_3 frac' in Figure 2.6). In this model, the fraction of hydrogens participating in a C_3 rotation decreases as temperature decreases, assuming a static $-CH_2-$ chain. The fractional C_3 motion of nBA is similar to that of ODA (0.624, Figure 10, Table 2) suggesting a similar degree of dynamics; however, the relaxation times of nBA are the shortest as discussed below indicative of more spatial motion within the cuboctahedral void as compared to ODA and GABA.

Having two ammonium groups, ODA electrostatically bridges two inorganic sheets (Figure 2.1), which appears to restrict its motions. At $T \geq 275$ K, the data are best described by the same $C_2 \otimes C_3$ motion found in nBA but for both of the $-CH_2NH_3$ head groups as well as librations of the aliphatic $-CH_2-$ hydrogens (Figure 2.6e). The differences in the EISFs from $T = 300$ K to $T = 275$ K are accounted for by a decrease in the libration radius of the $-CH_2-$ hydrogens (1.34 Å^{-1} vs. 0.586 Å^{-1}, Figure 10b). At $T = 250$ K, the only motions required to model the data include the combination of C_3 rotations of the $-NH_3$ head groups and librations of the organic chain. Below 250 K, the $-CH_2-$ hydrogens are nominally static, and temperature-dependent fractional C_3 rotation of the $-NH_3$ head groups describes the data (see Figure 10, Table 2). There is a stronger temperature dependence of ODA than nBA, as ODA has smaller EISF values and has longer relaxation times at low

temperatures where broadband emission is observed. None of the temperature-dependent changes in the rotational motions of ODA described by the EISF coincide with the phase transition detected by DSC (T = 215 K, Figure 2.4).

With both ammonium and carboxylic acid functional groups, two GABA molecules hydrogen bond to each other forming a bridge between inorganic sheets. This bridging, along with the planar sp^2 C of the carboxylic acid group also appears to restrict the cation's motion. Shown in Figure 2.6c, the data are modeled by C_3 motion of the $-NH_3$ head group (Figure 2.6f). Inclusion of $-CH_2-$ hydrogens librations or C_2 rotations of the hydroxyl group do not improve the fit; these hydrogens are therefore assumed to be nominally static within the convoluted resolution of the experiments ($\approx$ 1 μeV or 1.31 ns). The temperature dependence of the EISF is well modeled allowing for fractional C_3 motion in which the other hydrogens are assumed static (Figure 10, Table 2) indicating increased cation rigidity relative to nBA and ODA. The phase transition detected at $T = 265$ K from DSC (Figure 2.4) does not present significant changes to the EISF.

The relaxation times for nBA motions are shorter than both ODA and GABA. Relaxation times were determined from the half-width at half-maximum (HWHM) of the Lorentzian peaks fitted to QENS spectra (Figure 2.5, $\text{HWHM}_{\text{Lorentzian}} = \hbar/\tau$). At high temperatures there are multiple Lorentzian functions and thus one relaxation time for each Lorentzian peak required to fit the spectra (Figure 2.7). As temperature decreases, there are fewer independent motions detected by QENS, as only one relaxation time is needed to describe the motions. The relaxation times become longer at low temperature; however, the temperature dependence does not follow an Arrhenius expression (see Figure 3 and related

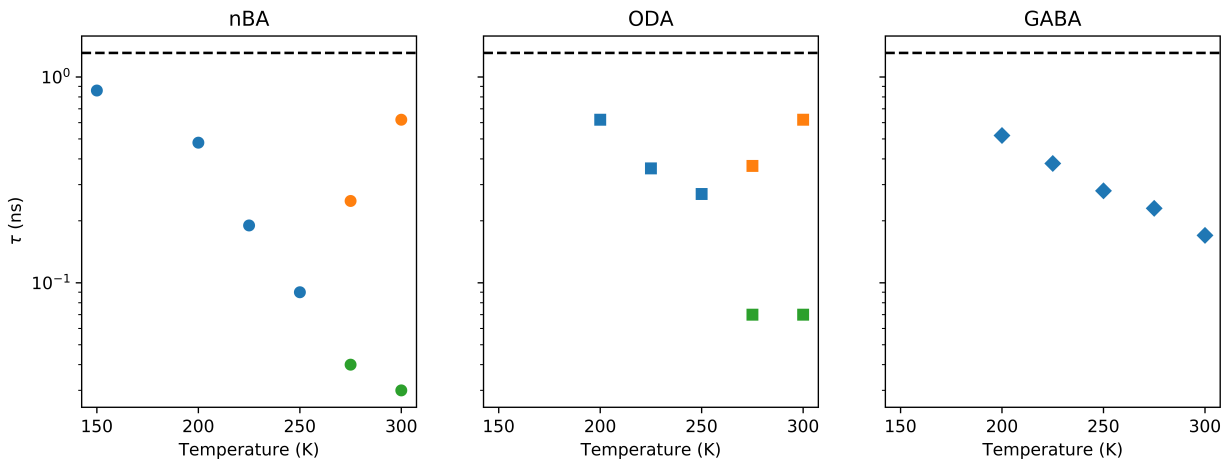

Figure 2.7: Relaxation times of hydrogen motions (τ, ns) extracted from QENS spectra of (left) (nBA)$_2$PbBr$_4$, (middle) (ODA)PbBr$_4$, and (right) (GABA)$_2$PbBr$_4$. Calculated from QENS data with $\text{HWHM}_{\text{Lorentzian}} = \hbar/\tau$. Black horizontal dashed lines indicate the instrument resolution. Blue symbols indicate a singular Lorentzian. Orange and green symbols indicate two separate Lorentzian functions used to model the QENS data.

discussion in the Supporting Information). Log-linear extrapolation of the relaxation times (Figure 11) permits estimation of the relaxation times for temperatures at which the molecular motions become sufficiently restricted as to be unresolvable from the elastic scattering (Table 8). The splitting of timescales in Figure 2.7 and Table 8 is indicative of the multiple independent rotations occurring at high temperatures and is observed in nearly all hybrid halide perovskites.[50] The C_2 rotation of the ammonium group has a longer relaxation time than that of the C_3 rotations occurring in either the methyl group (nBA) or the second amine (ODA) as seen for $(C_8H_{17}NH_3)_2PbI_4$.[5] In ODA, the freezing out of the C_2 rotation of the ammonium group occurs between 275 K and 250 K, this does not align with the phase transition at 215 K determined by DSC (Figure 2.4). Additionally, the phase transition in (GABA)$_2$PbBr$_4$ at 265 K does not correspond to a change in the QENS, as all molecular rotations are modelled by a fractional C_3 model and without temperature-dependent anomalies in the fitted parameter (Figure 10c, Table 2).

Table 2.1: Decay times calculated from time-resolved photoluminescence with $R(t) = B_1 \exp(-t/\tau_1) + B_2 \exp(-t/\tau_2)$. The data are described well by double exponential decay consisting of two components. Errors are estimated from one standard deviation.

Decay times (ns)					
Wavelength (nm)	$\tau 1_{ODA}$	$\tau 2_{ODA}$	Wavelength (nm)	$\tau 1_{GABA}$	$\tau 2_{GABA}$
402	1.7±0.1	19±1.3	391	7±0.3	34±3
550	15±0.7	269±7	550	41±4	278±16
600	17±1.3	378±13	587	49±9	304±26
635	14.5±1.7	420±15	624	-	263±4
680	20±2.3	416±21	650	-	316±7

The organic cation motions are faster than the photoluminescence decay lifetimes probed with time-resolved photoluminescence at various wavelengths over the broad emission in (ODA)$PbBr_4$ and $(GABA)_2PbBr_4$ and are well described by a biexponential decay. Normalization of the data to $\approx$ 158 ns reveals that transients have similar responses at long decay lifetimes. The low-temperature photoluminescence decay lifetimes of (ODA)$PbBr_4$ shown in Figure 2.8a are similar for all wavelengths recorded (17 ± 2 ns and 370 ± 61 ns, Table 2.1). All lifetimes are longer than the C-N rotational relaxation times observed by QENS and are well described by a biexponential decay. Figure 2.8b shows the photoluminescence decay at several wavelengths for $(GABA)_2PbBr_4$. The photoluminescence at longer wavelengths (624 nm and 650 nm) are well described by a single exponential decay. All lifetimes are $\approx$ 100 times slower than the relaxation times extrapolated from QENS.

2.5. Discussion

The organic cation dynamics differentiate $(n\text{BA})_2PbBr_4$ from (ODA)$PbBr_4$ and $(GABA)_2PbBr_4$, primarily in that the larger spatial extent of dynamics of nBA yields a larger

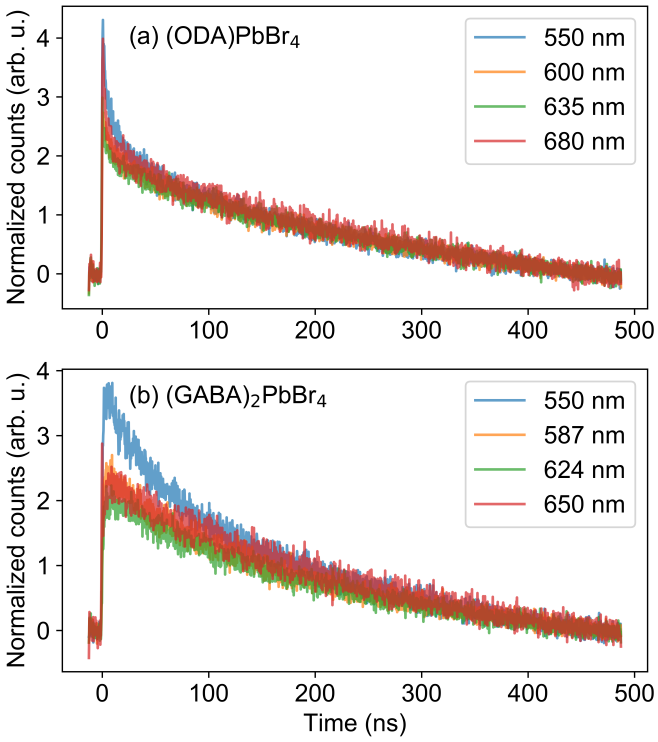

Figure 2.8: Time-resolved photoluminescence of (a) (ODA)$PbBr_4$ at 550 nm (black), 600 nm (red), 635 nm (blue), and 680 nm (green) and (b) $(GABA)_2PbBr_4$ at 550 nm (black), 587 nm (red), 624 nm (blue), and 650 nm (green) at 77 K. Data were normalized to the photoluminescence intensity at $\approx$ 158 ns.

effective cation radius. The larger effective A-site radius from the dynamic nBA cation exhibits a larger A-site volume (Figure 3.4). In-plane octahedral tilting in $(nBA)_2PbBr_4$ leads to a smaller calculated A-site volume less than the ideal 103.8 Å^3 calculated for $1/2$ of a cubeoctahedron with a tolerance factor of 1 using Pb and Br radii.[53,54] Calculations of the polyhedral volume from crystal structures within the A-site void determine the nBA A-site void is larger (84.6 Å^3) than the A-site void in GABA (79.6 Å^3), consistent with a greater spatial extent of hydrogen motion in nBA in $(n\text{BA})_2PbBr_4$ determined from QENS. In contrast, rigid cations (ODA, GABA) have smaller effective radii leading to a deviation further from the ideal 103.8 Å^3. As this could be an advantageous predictor for materials properties, we have expanded on these calculations in the Supplemental Information

(Table 3). There is a general trend in other A_2PbBr_4 materials, where a smaller A-site volume correlates to a larger out-of-plane tilt angle which is consistent with our results in this work.

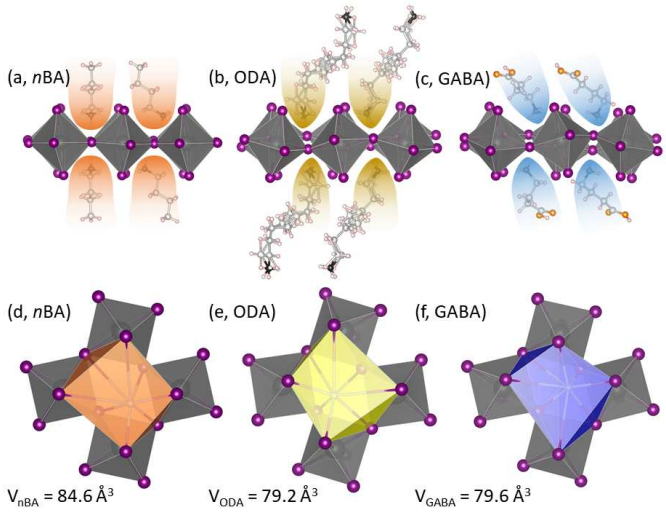

Figure 2.9: (a-c) Depiction of the effective radius in (a) $(n\text{BA})_2PbBr_4$ (b) $(ODA)PbBr_4$, and (c) $(GABA)_2PbBr_4$. The radii of ODA and GABA are smaller owing to the restricted dynamics of the cations. (d-f) A-site volume (illustrated by the $[NBr_8]$ polyhedra) determined from the 295 K crystal structures of (d) $(n\text{BA})_2PbBr_4$ (e) $(ODA)PbBr_4$ and (f) $(GABA)_2PbBr_4$.

We propose that the smaller effective cation radius drives out-of-plane octahedral tilting to compensate for the lack of evenly distributed positive charge from under-bonded apical halogens in the A-site void. The out-of-plane tilt angles directly correlate to the presence of broadband photoluminescence.[1,38] The ODP that drives exciton self-trapping increases with increasing out-of-plane tilting.[2] Therefore, the broadband emission stemming from STEs in $(ODA)PbBr_4$ and $(GABA)_2PbBr_4$ is indirectly influenced by the more restricted organic moiety dynamics in these materials. Based on the Goldschmidt tolerance factor, a larger A-site volume appears to prevent the out-of-plane tilting attributed to broadband emission.[2] This follows the trend that even larger cations occupying the A-site in the higher-dimensional Ruddlesden-Popper perovskites (where $n = 2$ and 3), such as

guanidinium, leads to compressed, distorted octahedra.[24,55] The expansion of the octahedral cage and elongation of Pb−I bonds in $(HA)_2(GA)Pb_2I_7$ and $(BA)_2(EA_xMA_{1-x})_2Pb_3I_{10}$ leads to a more distorted inorganic layer with blue shifted band gaps and additional greater inhomogeneous broadening.

While out-of-plane octahedral tilting and the ODP can lead to exciton self trapping, this mechanism cannot explain the extent of observed broadening. If the ODP arises primarily from a localized lattice vibration (on the order of THz), the phonon can only produce $\approx$ 100-200 meV of broadening.[36] This homogeneous broadening does not account for the entirety of the white-light spectrum emitted ($\approx$ 1200 meV). Therefore, another process, such as the organic cation dynamics of $(ODA)PbBr_4$ and $(GABA)_2PbBr_4$ provide a potential mechanism for additional (inhomogeneous) broadening of the broadband photoluminescence. The broad light emission in a related material, $(EDBE)PbBr_4$, has been previously described as originating from a single-ensemble of excited states, as the spectrum does not change as a function of decay time. It was found the excited state (e.g., the STE) samples "all possible local structures on a time scale that is fast compared to the emission decay time."[36] The $-NH_3$ rotations in $(ODA)PbBr_4$ and $(GABA)_2PbBr_4$ ($<$ 5 ns below 100 K) can provide such distinct local structures that contribute to the inhomogeneous broadening of the photoluminescence spectrum. While decay lifetimes differ at low wavelengths, normalization shows that after $\approx$ 158 ns, the photoluminescence transients are nearly identical (Figure 2.8, Table 2.1). If the timescale of organic motion is not significantly faster than emission decay, the emission will behave more like a multi-ensemble decay, such that the structural changes could induce spectral shifts.[36] A comparison between the time-resolved

photoluminescence decay lifetimes and extrapolated relaxation times from QENS can provide insight into whether the organic cation dynamics are locally sampled and contributing to the inhomogeneous broadening.

Here, the emission behavior in (ODA)$PbBr_4$ is single-ensemble-like owing to the similar decay at all wavelengths. The decay times at both short and long timescales in (ODA)$PbBr_4$ are not sensitive to changes in wavelength. An average of the bi-exponential decay across the broad spectrum gives 17$\pm$2 ns for τ_1 and 371$\pm$61 ns for τ_2. At 77 K, where broadband emission is observed and time-resolved photoluminescence data were collected, the ODA cation motion is extrapolated to $\approx$ 4.5 ns. The cation motion at 77 K is significantly shorter than the τ_2 decay time of 370 ns. τ_1 (17 ns) is slower than the organic motion by a factor of two and has spectral dependence. The emission behavior in $(GABA)_2PbBr_4$ is also single-ensemble-like; however, there is a subtle variation in the time-resolved data between samples. A further discussion is available in the Supplemental Information. We limit the discussion of $(GABA)_2PbBr_4$ to Figure 2.8 in the main text as the single crystal spectroscopy required to elucidate the variations between samples goes beyond the scope here. Averaging the decay lifetimes of the broad luminescence in $(GABA)_2PbBr_4$ reveal τ_1 is 45$\pm$4 ns and τ_2 is 290$\pm$21 ns. GABA has an extrapolated relaxation time of $\approx$ 2 ns for the motion of the ammonium group at 77 K which is significantly shorter than either decay lifetime presented here. Additionally, the decay times in $(GABA)_2PbBr_4$ are longer than those in (ODA)$PbBr_4$. The rotational motion of the $-NH_3$ at temperatures where broadband emission is observed could provide several local environments for the

photoexcited state to sample, owing to the faster organic cation motion relative to the calculated decay times.

2.6. Conclusions

The restricted organic cation dynamics in (ODA)$PbBr_4$ and $(GABA)_2PbBr_4$, relative to $(n\text{BA})_2PbBr_4$, lead to smaller effective dynamic radii and influence the octahedral out-of-plane tilt angle in layered hybrid halide perovskites. The increased tilt angle owing to the smaller radii correlates to the observation of broadband emission as a single ensemble. Organic cation motions are on $\approx$ 1 ns timescales as determined from QENS data, which are faster than the photoluminescence decay times determined from time-resolved photoluminescence spectroscopy. However, further studies are needed to elucidate the variations in time-resolved photoluminescence between samples. In (ODA)$PbBr_4$ and $(GABA)_2PbBr_4$, the $-NH_3$ rotations of the organic cations likely contribute to the inhomogeneous spectral broadening by providing a distribution of local structures that appear as a single ensemble on the photoluminescence time scale. This work highlights the critical role the organic cation dynamics play in the structure and subsequent optoelectronic properties of layered hybrid halide perovskites.

3. Influence of Inorganic Layer Thickness on Methylammonium Dynamics in Hybrid Perovskite Derivatives[†]

3.1. Summary

The layered Ruddlesden-Popper derivatives of $CH_3NH_3PbI_3$ have recently emerged as high-performing materials for photovoltaics with improved stability. The inclusion of organic molecules within the inorganic framework provides additional dynamic degrees of freedom which influence the optoelectronic properties. The rotational dynamics of $CH_3NH_3^+$ influence dielectric behavior and electronic excited state dynamics in $CH_3NH_3PbI_3$; however, the influence of cation dynamics on properties in the layered derivatives has not yet been determined. We employ quasi-elastic neutron scattering to study the rotational dynamics of methylammonium ($CH_3NH_3^+$, MA) and deuterated n-butylammonium ($CD_3(CD_2)_3NH_3^+$, d-nBA) in $(d{-}n\text{BA})_2(\text{MA})_{n-1}\text{Pb}_n\text{I}_{3n+1}$ (n = 2, 3). $(d{-}n\text{BA})_2(\text{MA})_2\text{Pb}_3\text{I}_{10}$ exhibits shorter residence times of the $CH_3NH_3^+$ and

[†]Reproduced with permission from Koegel, A. A, Oswald, I. W. H., Rivera, C., Miller, S. L., Fallon, M. J., Prisk T. R., Brown, C. M, Neilson J. R. Influence of Inorganic Layer Thickness on Methylammonium Dynamics in Hybrid Perovskite Derivatives. *ACS Chem. Mater.* **2022**, 34, 18, 8316–8323, https://doi.org/10.1021/acs.chemmater.2c01868. Copyright 2022 American Chemical Society.
Author Contributions: Alexandra Koegel collected and analyzed the neutron scattering and X-ray diffraction data and prepared the manuscript. Iain Oswald prepared the samples and collected the neutron scattering and nuclear magnetic resonance spectroscopy data. Chuy Rivera prepared the samples. Samantha Miller analyzed the nuclear magnetic resonance spectroscopy data. Jewels Fallon collected the nuclear magnetic resonance spectroscopy data. Timothy Prisk collected and analyzed neutron scattering data. Craig Brown collected and analyzed neutron scattering data. James Neilson edited the manuscript and oversaw the project.

$CD_3(CD_2)_3NH_3^+$ reorientational motions, which is attributed to the larger volumes that the cations occupy in the inorganic framework and to the dimensionality of the inorganic layer by way of dielectric screening between the organic cations. Discontinuities in the mean-squared displacement of overall hydrogen motion determined by fixed-window elastic neutron scattering are consistent with phase transitions observed by differential scanning calorimetry and time-resolved microwave conductivity signals. Determining how the dimensionality of the inorganic layer influences the organic cation rotational dynamics provides fundamental chemical insight into how the electronic dynamics vary between n-members.

3.2. Introduction

The field of solution-processable semiconductors has undergone rapid development owing to the discovery of hybrid halide semiconductors.[56–58] The prototypical hybrid halide semiconductor based on the perovskite structure with the formula ABX_3 (A = (in)organic cation, B = metal, X = halide) is composed of three-dimensional (3D) corner-connected $[BX_6]$ octahedra with the A-site cation filling the cuboctahedral void. The $CH_3NH_3PbI_3$ perovskite in particular has excellent charge-transport and visible light absorption.[59,60] This prototypical structure can be further modified with the incorporation of large organic cations, such as n-butylammonium (nBA) or phenylethylammonium (PEA),[61,62] which disrupt the 3D connectivity and reduce dimensionality as shown in Figure 3.1. These so-called "Ruddlesden-Popper" compounds form a homologous series of phases with the chemical formulae, $(R{-}NH_3)_2(A)_{n-1}B_nX_{3n+1}$, with the series spanning

compounds containing layers comprised of a single BX_6 octahedron ($n = 1$) up to 7 octahedra thick ($n = 7$).[63,64] This change in octahedral layer thickness drastically affects the thermodynamic stability of the materials,[6] as well as the optoelectronic properties, such as reduced band gaps and resistivity,[60,62] increased carrier lifetimes,[3] and smaller exciton binding energies at higher octahedral layer thicknesses.[3] These relationships highlight the importance of structural control of a material when targeting a specific property.

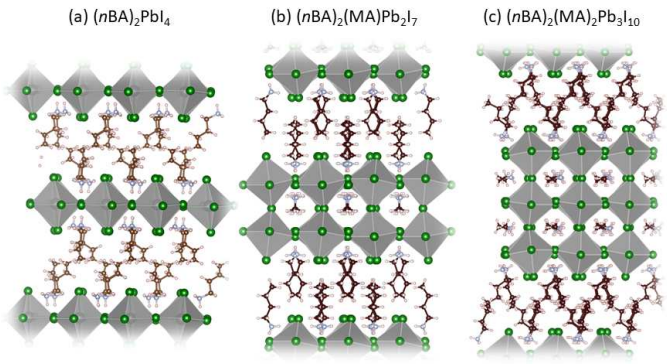

Figure 3.1: Illustrations of the crystal structures of (a) $(n\text{BA})_2\text{PbI}_4$, $n = 1$, (b) $(n\text{BA})_2(\text{MA})\text{Pb}_2\text{I}_7$, $n = 2$, and (c) $(n\text{BA})_2(\text{MA})_2\text{Pb}_3\text{I}_{10}$, $n = 3$. nBA = $CH_3(CH_2)_3NH_3^+$, MA = $CH_3NH_3^+$, gray = Pb, green = I, brown = C, blue = N, pink = H.

The incorporation of large organic cations into the perovskite structure provides access to electronic dynamics beyond those of the 3D perovskite.[3] We have previously shown the organic cation dynamics are coupled to the inorganic structure and thus optoelectronic properties in layered perovskite derivatives containing single-octahedron thick layers (e.g., $n = 1$).[65] As the inorganic framework and organic "spacers" are closely coupled, it is necessary to understand what role the organic cations play in influencing the electronic dynamics in the multi-layered ($n > 1$) perovskites. The atomistic and molecular dynamics of single-layered perovskites have been studied both computationally[26] and experimentally.[5,65–67] These neutron spectroscopy, NMR spectroscopy, and molecular dynamics simu-

lation studies reveal that organic cation rotational dynamics influence the inorganic structure, the formation of excitons (both free and self-trapped) and subsequent light emission in single layer perovskites. However, to our knowledge, the organic cation dynamics of multi-layered perovskite derivatives have only been studied computationally.[22]

Here, we report the cation rotational dynamics of $(d{-}n\text{BA})_2(\text{MA})_{n-1}\text{Pb}_n\text{I}_{3n+1}$ (d-nBA = $CD_3(CD_2)_3NH_3^+$, MA = $CH_3NH_3^+$, $n = 2$ and 3) with quasi-elastic neutron scattering (QENS) and find that $(d{-}n\text{BA})_2(\text{MA})_2\text{Pb}_3\text{I}_{10}$ has shorter residence times as described by a "jump model"[52] for organic cation reorientations. Shorter residence times of the hydrogen motions are consistent with increased dynamics. At higher temperatures, the $CD_3(CD_2)_3NH_3^+$ dynamics are restricted spatially while the smaller $CH_3NH_3^+$ contributes to the quasi-elastic scattering as described by a "jump model" with 90° motions (i.e., a pseudo-C_4 reorientations). At lower temperatures, the $CD_3(CD_2)_3NH_3^+$ dynamics are nominally static and the $CH_3NH_3^+$ reorientational motions become fractionally frozen as the temperature decreases. The spatial restriction of the $CH_3NH_3^+$ dynamics correspond to previously reported temperature-dependent phase transitions and microwave conductivity transients, implicating the organic cation dynamics in the varying electronic dynamics between samples. Density functional theory calculations of these materials with methylammonium cations frozen in different configurations reveals significant changes to the electronic properties (e.g., direct to indirect bandgap transitions, a mobility).[68] Molecular dynamics simulations using relatively simple pair-wise potentials reveals structure-dependent dynamics of the methylammonium reorientations, such that orientations become hindered for smaller "n,"[22] consistent with the experimental results provided here.

The neutron scattering results described in this contribution illustrate that increased layer thickness decreases the residence times of organic cation reorientations in layered hybrid halide perovskites and that the temperature-dependent rotational motion corresponds to longer time-resolved microwave conductivity lifetimes.

3.3. Experimental

All syntheses were performed in air at room temperature. Materials were used as received from the manufacturer. Acronyms used: nBA = n-butylammonium, d-nBA = n-butylamine-d_{11} deuteriochloride, MACl = methylammonium chloride. The starting PbI_2 concentrations were determined from the molar solubility of the desired product in order to maximize yield and purity.[18]

Preparation of (nBA)$_2$(MA)Pb$_2$I$_7$:[18] A 0.48 M solution of PbI_2 was prepared by the addition of 0.536 g (2.4 mmol) PbO in 5 mL aqueous HI (57 wt% in H_2O, $<$1.5% H_2PO_2). To this solution, 0.081 g (1.2 mmol) of MACl (98 %, Beantown Chemical) was dissolved followed by the addition of 0.238 mL (2.4 mmol) n-butylamine (Sigma Aldrich) titrated dropwise and stirred for 20 minutes. 3 mL of glacial acetic acid (60% of the total volume, Fisher Chemical, Certified ACS) was then added to the solution and let stir for a further 20 minutes, yielding opaque, red, microcrystalline powder. The precipitate was collected by vacuum filtration and washed with glacial acetic acid (Fisher Chemical, Certified ACS) and hexanes (Fisher Chemical, Certified ACS) and dried in air for 30 min. Phase purity was confirmed by powder X-ray diffraction.

Preparation of (nBA)$_2$(MA)$_2$Pb$_3$I$_{10}$:[18] A 0.48 M solution of PbI_2 was prepared by the ad-

dition of 0.536 g (2.4 mmol) PbO in 5 mL aqueous HI (57 wt% in H_2O, $<$1.5% H_2PO_2). To this solution, 0.108 g (1.6 mmol) of MACl (98 %, Beantown Chemical) was dissolved followed by the addition of 0.158 mL (1.6 mmol) n-butylamine (Sigma Aldrich) titrated dropwise and let stir for 20 minutes, yielding an opaque, purple, microcrystalline powder. 3 mL of glacial acetic acid (60% of the total volume, Fisher Chemical, Certified ACS) was then added to the solution and let stir for a further 20 minutes, yielding opaque, purple, microcrystalline powder. The precipitate was collected by vacuum filtration and washed with hexanes (Fisher Chemical, Certified ACS) and dried in air for 2 hours. Phase purity was confirmed by powder X-ray diffraction.

Preparation of deuterated compounds: Deuterated $(d{-}n\text{BA})_2(\text{MA})\text{Pb}_2\text{I}_7$ and $(d{-}n\text{BA})_2(\text{MA})_2\text{Pb}_3\text{I}_{10}$ were prepared similarly to above where d-nBA (n-butylamine-d_{11} deuteriochloride, 98 atom % Sigma Aldrich) was added to the PbI_2 solution prior to the addition of glacial acetic acid. Yields were similar to undeuterated compounds. Samples were prepared in air and stored in an Argon glove box. Phase purity was confirmed by powder X-ray diffraction.

Powder X-ray diffraction (PXRD): Laboratory powder X-ray diffraction data were collected on a Bruker D8 Discover DaVinci Powder X-ray Diffractometer using Cu Kα radiation and a Lynxeye XE-T position-sensitive detector. Samples were prepared on a zero-diffraction Si wafer. The PXRD data were modeled with space groups of *Cc2m* for $(n\text{BA})_2(\text{MA})\text{Pb}_2\text{I}_7$ and *C2ce)* for $(n\text{BA})_2(\text{MA})_2\text{Pb}_3\text{I}_{10}$ using previously reported structures[62] with the Rietveld method implemented in TOPAS v6 (Bruker AXS). VESTA was used to render crystal structures and to compute polyhedral volumes of experimental crystal struc-

tures.[41]

Nuclear Magnetic Resonance (NMR) Spectroscopy: Proton NMR spectra were collected at 25 °C using a Varian Agilent 400 MHz spectrometer operating at 9.4 T. The $(d{-}n\text{BA})_2(\text{MA})\text{Pb}_2\text{I}_7$ analyte was mixed with a d-DMSO lock solvent by dissolving 50 mg of $(d{-}n\text{BA})_2(\text{MA})\text{Pb}_2\text{I}_7$ in d-DMSO and heating gently for 10 minutes until all crystallites dissolved prior to collecting scans. All NMR spectra were processed in MestreNOVA (MNOVA, ver. 12.0.4-22023).[69] The size of the direct NMR FIDs was 16,381 data points. All spectra were zero-filled to twice the number of data points and apodized with a 1.00 Hz exponential weighting function during data processing. Individual peaks were fitted with the appropriate Lorentzian-Gaussian lineshapes in the MNOVA. Integrated intensities were used to analyze the constituent peaks. Tetramethylsilane (TMS) was used as a standard chemical shift reference.

Fixed-window elastic neutron scattering: Fixed-window elastic scattering data were collected using the High Flux Backscattering Spectrometer (HFBS) at the National Institute of Standards and Technology Center for Neutron Research (NIST, NCNR) on samples of $(d{-}n\text{BA})_2(\text{MA})\text{Pb}_2\text{I}_7$ and $(d{-}n\text{BA})_2(\text{MA})_2\text{Pb}_3\text{I}_{10}$.[42] At HFBS, the sample environment employed in this Fixed-window experiment is a closed-cycle refrigerator (CCR) that cools or warms the sample by thermal conduction in the presence of helium exchange gas. A mass of 3.260 g of $(d{-}n\text{BA})_2(\text{MA})\text{Pb}_2\text{I}_7$ and 3.157 g of $(d{-}n\text{BA})_2(\text{MA})_2\text{Pb}_3\text{I}_{10}$ were used for this experiment. The cylindrical sample cell has a diameter of approximately 3 cm, and the powder sample was held against the lateral area of the sample can by enclosing it within aluminum foil pouches. The sample cell was loaded in a helium glove box and sealed with

an indium O-ring. The enclosed helium ensures good thermal contact between the powder and the rest of the sample environment. Fixed-window scans were performed according to the following protocol. Initially, the samples were loaded into the CCR at 295 K and cooled to 5 K. Data were continuously collected at a ramp rate of 0.7 K/min with 60 sec/point. Finally, data were collected upon heating at the same nominal ramp rate and time per point for $(d{-}n\text{BA})_2(\text{MA})_2\text{Pb}_3\text{I}_{10}$. The $(d{-}n\text{BA})_2(\text{MA})\text{Pb}_2\text{I}_7$ sample was heated faster than it was cooled at 1.3 K/min. This may contribute to the increased the hysteresis observed in the Fixed-window scan for the $(d{-}n\text{BA})_2(\text{MA})\text{Pb}_2\text{I}_7$ sample. The observed scattering was normalized to the incident beam monitor. A Fixed-window scan is a measurement of the elastic intensity $I_{el}(Q,T)$ as a function of Q, momentum transfer, and temperature, T. The effective mean-squared displacement, $\langle u^2 \rangle$, of the hydrogen atoms is estimated by assuming that $I_{el}(Q,T)$ is governed by a Debye-Waller factor: $I_{el}(Q,T) = I_{el}(Q, T = 5.0 \text{ K}) \cdot \exp(-Q^2\langle u^2 \rangle/3)$.[43,44 43,44] The temperature-dependence of the effective mean-squared displacement quantifies the extent of motion of the hydrogen atoms within the time window determined by the instrumental elastic resolution function of $\approx$ 0.8 μeV. This calculation was performed using the DAVE software.[45]

Quasi-elastic neutron scattering (QENS): QENS measurements were collected using the time-of-flight Disc Chopper Spectrometer (DCS) at the NCNR.[70] The DCS operated in low resolution mode with a neutron beam with a wavelength of 4.8 Å^{-1} over a Q range of 0.2 Å^{-1} to 2.5 Å^{-1} at a chopper speed of 20,000 rpm. The hydrogen residence times were calculated from $\text{HWHM}_{\text{Lorentzian}} = \hbar/\tau$. The samples from Fixed-window scan measurements were enclosed in a cylindrical 10 cm x 1.5 cm aluminium sample can with an

indium O-ring. Temperature-dependent QENS measurements were collected upon cooling at temperatures identified from Fixed-window elastic scans. The instrument resolution function (IRF) was collected at 4 K for both samples and convolved with a delta function to describe the elastic interactions within the samples. A background aluminium scan was collected at 100 K at a wavelength of 4.8 $Å^{-1}$. The scattering intensity was normalized to both the incident beam monitor and the aluminum background. This places the measured scattering at all Q upon a common arbitrary intensity scale. The constant instrumental background was subtracted from the scattering. Data were reduced and analyzed in DAVE in order to extract the Elastic Incoherent Structure Factor (EISF).[45] The function: $\text{EISF} = I_{\text{elastic}}/(I_{\text{elastic}} + I_{\text{quasi-elastic}})$ was used to describe the magnitude of the QENS component where *I* is the integrated intensity of the respective elastic or quasi-elastic scattering. QENS spectra were fit with an IRF, linear background, and a single Lorentzian function (Figure 16). The experimental IRFs convolved with a δ-function centered at zero energy describe the elastic scattering and instrumental function while Lorentzian functions convolved with the IRF describe the quasi-elastic components. Jump models of the molecular dynamics were fit to the EISFs, as described in the results section. These analyses implemented in python are provided as supplemental material.[5,29,52] Detector groups that encompassed Bragg reflections were removed for the EISF analysis.

3.4. Results

Samples of $(d{-}n\text{BA})_2(\text{MA})\text{Pb}_2\text{I}_7$ and $(d{-}n\text{BA})_2(\text{MA})_2\text{Pb}_3\text{I}_{10}$ were confirmed phase pure by powder X-ray diffraction (PXRD, Figure 13).[62] A nuclear magnetic resonance (NMR)

spectrum shown in Figure 14 confirms the complete deuteration of the aliphatic carbons in ($d-n$BA)$_2$(MA)Pb$_2$I$_7$, as indicated by the absence of stray peaks between 0.8 ppm and 1.4 ppm.[6] A complete discussion of the NMR spectroscopy of the dissolved crystal and mother liquor from synthesis is available in the Supplemental Information.

The mean-squared displacements (MSD, Figure 3.2) of the two materials with different octahedral layer thicknesses show similar spatial extent of hydrogen motion in methylammonium ($CH_3NH_3^+$) and d-nBA ($CD_3(CD_2)_3NH_3^+$). The MSDs are calculated from the Q-dependent intensity of fixed-window elastic incoherent neutron scattering. Here, the neutron scattering is most sensitive to the rotational dynamics of $CH_3NH_3^+$ and the ammonium headgroup of d-nBA, due to the large relative microscopic scattering cross section of hydrogen (82.02 barns) relative to the other elements. This represents approximately 79% and 83% of the total macroscopic cross section for ($d-n$BA)$_2$(MA)Pb$_2$I$_7$ and ($d-n$BA)$_2$(MA)$_2$Pb$_3$I$_{10}$, respectively (C = 5.551 barns, Pb = 11.118 barns, Deuterium = 7.64 barns, I = 3.81 barns, N = 11.51 barns; all natural abundance except deuterium).[51] The deuteration of the n-butylammonium cations minimizes its contribution to the quasi-elastic scattering, thus allowing us to directly monitor the methylammonium hydrogen dynamics. The discontinuities in ($d-n$BA)$_2$(MA)Pb$_2$I$_7$ occur at 278 K, 203 K, ≈183 K, and ≈148 K as shown in Figure 3.2a. ($d-n$BA)$_2$(MA)$_2$Pb$_3$I$_{10}$ has similar discontinuities at 277 K, 186 K, ≈183 K, and ≈148 K (Figure 3.2b). Values at 183 K and 148 K are approximated from previous measurements.[3] The discontinuities in the MSD at ≈183 K in both samples are representative of a significant decrease in organic cation dynamics and correspond to the previously measured transitions upon cooling.[3] Hysteresis of the MSD is larger in

$(d{-}n\text{BA})_2(\text{MA})\text{Pb}_2\text{I}_7$ and likely results from the faster heating ramp rate as detailed in the methods. The hysteresis in the MSD at 203 K upon heating in $(d{-}n\text{BA})_2(\text{MA})\text{Pb}_2\text{I}_7$ and 186 K upon heating in $(d{-}n\text{BA})_2(\text{MA})_2\text{Pb}_3\text{I}_{10}$ is brought on by phase transitions restricting organic cation motion observed previously by differential scanning calorimetry (DSC).[3] Transitions coincide with the discontinuities in the MSDs highlighted by dashed lines in Figure 3.2. Temperature-dependent quasi-elastic neutron scattering spectra illustrate that these phase transitions reduce the cation spatial and temporal dynamics, as described below.

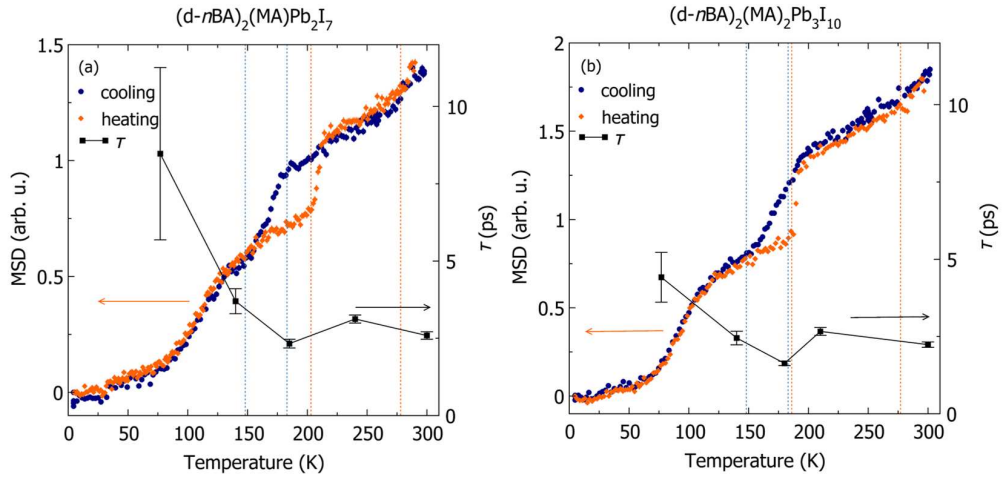

Figure 3.2: Mean-squared displacements (MSD, left axis) and residence times (τ, ps, right axis) of hydrogen motion in (a) $(d{-}n\text{BA})_2(\text{MA})\text{Pb}_2\text{I}_7$ and (b) $(d{-}n\text{BA})_2(\text{MA})_2\text{Pb}_3\text{I}_{10}$. MSDs upon cooling (blue) and heating (orange) were collected from 5 K to 300 K. Phase transitions determined from differential scanning calorimetry[3] values are highlighted with dashed lines (orange for heating, blue for cooling) at (a) $T = 278$ K, 203 K, ≈183 K, and ≈148 K for $(d{-}n\text{BA})_2(\text{MA})\text{Pb}_2\text{I}_7$ and (b) $T = 277$ K, 186 K, ≈183 K, and ≈148 K for $(d{-}n\text{BA})_2(\text{MA})_2\text{Pb}_3\text{I}_{10}$. Residence times of hydrogen rotations (black squares, right y-axis) from 77 K to 300 K determined from the half-width-at-half-maximum of quasi-elastic neutron spectra and show shorter residence times for $(d{-}n\text{BA})_2(\text{MA})_2\text{Pb}_3\text{I}_{10}$. There is a decrease in the residence times of both samples, as the CH_3NH_3^+ cation C_4 rotational motion becomes spatially restricted at ≈183 K. Error bars represent one standard deviation.

The analysis of the incoherent and quasi-elastic scattering contributions between the two samples supports the similar spatial extent of organic dynamics seen in the MSDs. Q-dependent QENS spectra are well fit with an instrument resolution function (IRF) con-

volved with a δ-function to describe any elastic scattering (Figure 16) and a Lorentzian function to describe the remaining quasi-elastic scattering ascribed to molecular rotations. After partitioning the scattering into elastic and quasi-elastic contributions, we calculate the elastic incoherent structure factor (EISF) and residence time (τ) of hydrogen motions as discussed below.

The energetically broader quasi-elastic scattering contributions in ($d-n$BA)$_2$(MA)$_2$Pb$_3$I$_{10}$ (Figure 16) reveals shorter residence times relative to ($d-n$BA)$_2$(MA)Pb$_2$I$_7$ as shown in Table 8 and Figure 3.2. The residence times, τ, of principle hopping motions were calculated from the half-width-at-half-maximum of the Lorentzian function describing the quasi-elastic scattering
(HWHM $= \hbar/\tau$). Generally, the residence times increase as a function of decreasing temperature as thermal motion is stunted. However, there is a decrease in the residence times at T = 185 K and 180 K for ($d-n$BA)$_2$(MA)Pb$_2$I$_7$ and ($d-n$BA)$_2$(MA)$_2$Pb$_3$I$_{10}$, respectively, indicated by asterisks in Table 8. The decrease in the residence times at $T =$ 185 K and 180 K coincides with the large discontinuities seen in the MSDs (Figure 3.2, dashed lines) and transitions observed previously by differential scanning calorimetry.[3] These decreases in the residence times in both samples are explained by a phase transition that restricts the C_4 methylammonium rotational motion.

The EISFs for each n-member are well modeled by the rotations of $CH_3NH_3^+$ and d-nBA constrained by symmetry-adapted motions derived from the room temperature crystal structures. $CH_3NH_3^+$ is constrained by the C_3 symmetry along the C-N axis of the molecule and can rotate about the $-NH_3^+$ and $-CH_3$. The $CH_3NH_3^+$ is further constrained within

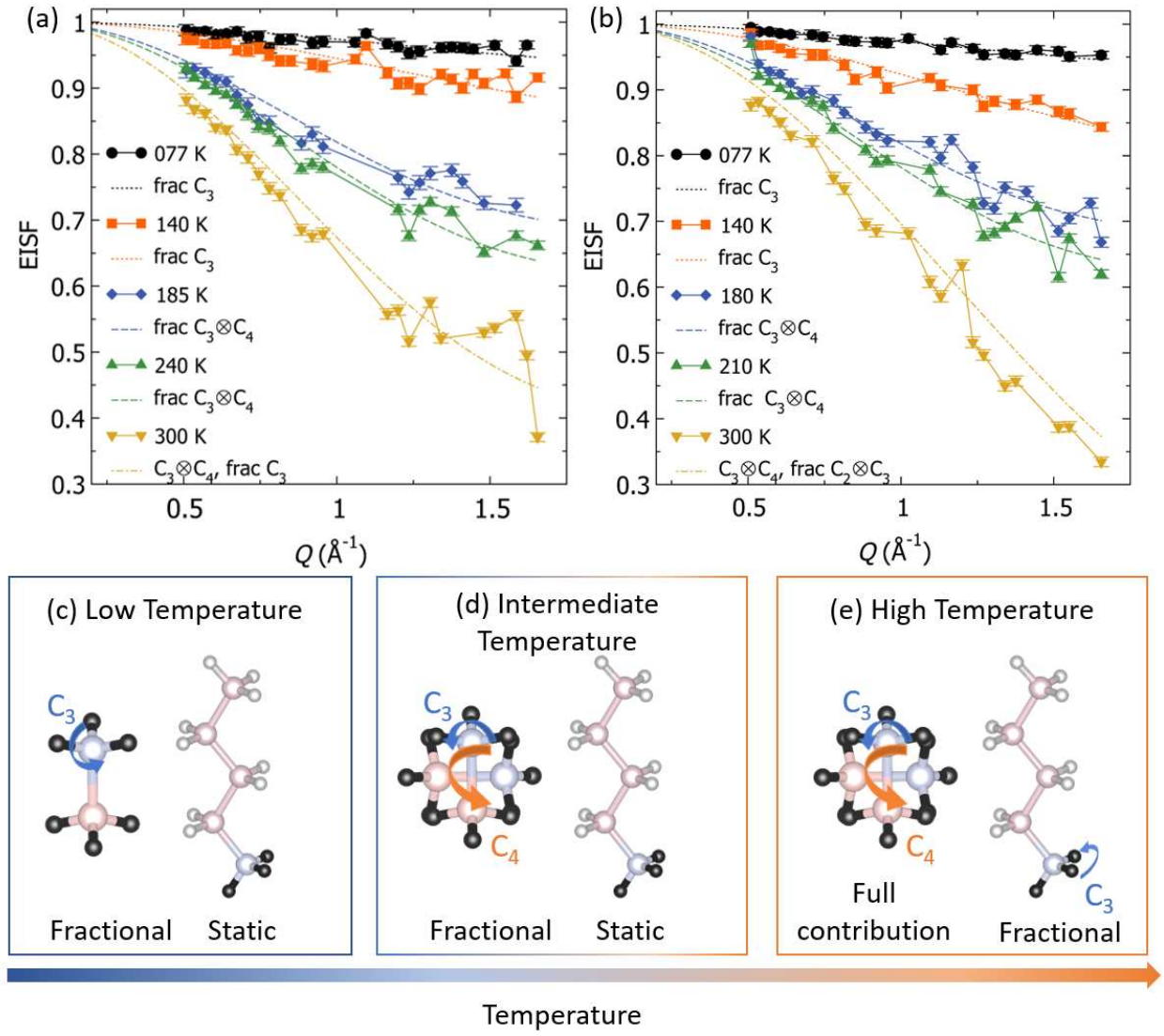

Figure 3.3: Top: Elastic Incoherent Structure Factors of (a) $(d{-}n\text{BA})_2(\text{MA})\text{Pb}_2\text{I}_7$ and (b) $(d{-}n\text{BA})_2(\text{MA})_2\text{Pb}_3\text{I}_{10}$ at 77 K to 300 K extracted from QENS data (DCS, NIST) with jump models describing $C_3{\otimes}C_4$ motion of $CH_3NH_3^+$ with fractional C_3 motion of the $d{-}n$BA $-NH_3$ headgroup (dot-dashed), $C_3{\otimes}C_4$ of $CH_3NH_3^+$ only (dashed), and fractional $CH_3NH_3^+$ C_3 rotations (dotted). The differences in quasi-elastic contributions separate into three distinct regimes: 300 K ; 240K - 180 K ; 140 K -77 K. Bottom: Organic cation rotations modeled in the three different temperature regimes as described in the narrative. (c) Temperatures $\leq$ 140 K where there is only fractional C_3 rotational motion of the $CH_3NH_3^+$ cation, described by blue arrows, and the d-nBA motions are nominally static. (d) Temperature range from 180 K $\leq T \leq$ 240 K where there is fractional $C_3 \otimes C_4$ tumbling of the $CH_3NH_3^+$ in the cuboctahedral void, where the C_4 is described by orange arrows and C_3 is described by blue arrows, and the d-nBA motions are nominally static. (e) $T = 300$ K where there is a full contribution of $C_3 \otimes C_4$ $CH_3NH_3^+$ tumbling and fractional C_3 rotation of the d-nBA$-NH_3$ headgroup in the organic layer, where the C_3 is described by blue arrows. Hydrogen atoms that are observable are colored black. Pale pink = C, pale blue = N, gray = D.

the pseudo-C_4 symmetry of the cuboctahedral void it occupies.[29] Since the d-nBA only contains H on the ammonium head group, its neutron scattering signature is well constrained by C_3 symmetry along the C-N axis.[5,65] These models are then fit to the temperature-dependent EISFs to describe the type of motion occurring at each respective measured temperature. The EISF data separates into three distinct temperature ranges punctuated by the known phase transitions for both materials: "high" temperature at 300 K, "intermediate" temperatures from 240 K to 180 K, and "low" temperatures below 140 K. Each of these temperature regimes appear qualitatively different in Figure 3.3 and are best described with different rotational models shown in Figure 3.3 and discussed below. Alternative models that do not adequately describe the EISFs are described in the supporting information.

In both samples at $T = 300$ K, the EISFs are well described by the combination of the full, symmetry-adapted rotational contribution from $CH_3NH_3^+$ and fractional rotational contribution from d-nBA. The $CH_3NH_3^+$ cation undergoes a 120° convolved with a 90° ($C_3 \otimes C_4$) tumbling in the organic cation site (A-site void, Figure 3.3). This $C_3 \otimes C_4$ tumbling of $CH_3NH_3^+$ is modeled in conjunction with a fractional 120° (C_3, Figure 3.3) rotational contribution from the d-nBA $-NH_3$ headgroup at $T = 300$ K. The d-nBA rotational motion is best described purely by C_3 rotations of the ammonium headgroup. In contrast, the rotational motion of long-chain aliphatic ammonium cations has been previously described with a combined $C_2 \otimes C_3$ motion of the $-CD_2NH_3$ head group rather than just C_3 rotation of the ammonium;[5,65] however, such a $C_2 \otimes C_3$ model is inconsistent with the EISFs presented here (Figures 18 and 19). The model presented here describing the

d-nBA motion for the compounds with multiple octahedral layers (e.g., $n \geq 2$) is consistent with molecular dynamics simulations.[22] For 240 K $\geq T \geq$ 180 K, the d-nBA C_3 $-NH_3$ headgroup motions are nominally static within the resolution of the instrument for both materials and the only motion that best describes the EISF is a fractional contribution of $CH_3NH_3^+$ $C_3 \otimes C_4$ reorientations (Figure 3.3, green and blue dashed lines). The fractional motion is described as a linear combination of some fraction of the molecules experiencing the motion and the other fraction are modeled as static; the fractional contribution is a fitted parameter. When included in the model, a C_3 rotation of the $-NH_3$ headgroup in d-nBA, in combination with a full $C_3 \otimes C_4$ tumbling of the $CH_3NH_3^+$, models too significant a quasi-elastic contribution to the EISF to describe the data for $T <$ 300 K (Figure 20). At temperatures $\leq$ 140 K, the $CH_3NH_3^+$ reorientational motion is described by fractional contributions of the $CH_3NH_3^+$ C_3 rotation (Figure 3.3) as the $C_3 \otimes C_4$ motions become static and the d-nBA motions remain static in both materials. Here, the fractional contribution assumes that some fitted fraction of molecules experience this motion and the remaining molecules are static. As the temperature decreases, the fraction of reorienting hydrogen (frac C_3) decreases.

The restriction of the d-nBA rotations correlates with the transitions at $T =$ 278 K and 277 K observed by MSD (Figure 3.2) and differential scanning calorimetry,[3] leaving only the $C_3 \otimes C_4$ tumbling of the $CH_3NH_3^+$ in the cuboctahedral void to be modeled from $T =$ 240 K to 180 K. The same model of fractional $C_3 \otimes C_4$ MA rotations with static d-nBA, is used to describe the data at $T =$ 240 K and 185 K in $(d{-}n\text{BA})_2(\text{MA})\text{Pb}_2\text{I}_7$ and 210 K and 180 K in $(d{-}n\text{BA})_2(\text{MA})_2\text{Pb}_3\text{I}_{10}$. The differences in the EISFs are explained by a reduction

of the fractional contribution of $C_3 \otimes C_4$ motion (Figure 22, Table 6). Table 6 lists the reduction in the modeled $C_3 \otimes C_4$ fraction as a function of temperature. The fraction of $C_3 \otimes C_4$ motion decreases from 0.77 to 0.64 in ($d-n$BA)$_2$(MA)Pb$_2$I$_7$, and from 0.57 to 0.47 in ($d-n$BA)$_2$(MA)$_2$Pb$_3$I$_{10}$. Further, complete restriction of $C_3 \otimes C_4$ motion in both samples corresponds to transitions reported by differential scanning calorimetry at $\approx$ 183 K and is also seen in the MSD (Figure 3.2).[3]

At $T \leq$ 140 K, the model describing exclusively fractional C_3 motion of methylammonium is used to describe the data; however, the differences between the EISFs is again due to a decrease in the relative fraction of methylammonium C_3 motion occurring. The values listed in Table 7 for ($d-n$BA)$_2$(MA)Pb$_2$I$_7$ characterize a decrease in the C_3 fraction from 0.36 at $T =$ 140 K to 0.17 at $T =$ 77 K. The values for ($d-n$BA)$_2$(MA)$_2$Pb$_3$I$_{10}$ also show a decrease from 0.37 at $T =$ 140 K to 0.13 $T =$ 77 K in the fraction of C_3 motion.

3.5. Discussion

The shorter residence times in ($d-n$BA)$_2$(MA)$_2$Pb$_3$I$_{10}$ relative to ($d-n$BA)$_2$(MA)Pb$_2$I$_7$ follow trends in the the crystallographic site volume and screening effects of having higher inorganic dimensionality. The organic cation site (i.e., A-site void) volumes are very similar between the two samples. The A-site voids were calculated by connecting [NI$_{12}$] polyhedra for $CH_3NH_3^+$ (MA) and [NI$_8$] polyhedra for d-nBA (i.e., nitrogen centered polyhedra).[65] The calculated volumes for the MA sites in (nBA)$_2$(MA)$_2$Pb$_3$I$_{10}$ are larger than those of (nBA)$_2$(MA)Pb$_2$I$_7$ using the $T =$ 298 K crystal structures ($CH_3NH_3^+{}_{vol} \approx$ 209 Å^3 vs 207 Å^3, Figure 3.4). The somewhat structurally-confined A-site correlates with the longer resi-

dence times and more spatially restricted $CH_3NH_3^+$ reorientations in $(n\text{BA})_2(\text{MA})\text{Pb}_2\text{I}_7$ as seen in the single layered lead bromides, $(R{-}\text{NH}_3)_2\text{PbBr}_4$.[65] However, the different polyhedral volumes are within two Å^3 of one another; therefore, we also consider additional explanations for the reduced residence times in $(n\text{BA})_2(\text{MA})_2\text{Pb}_3\text{I}_{10}$.

It was previously concluded that an increased number of inorganic layers leads to greater rotational freedom of the $CH_3NH_3^+$ cation. Previous molecular dynamics simulations support and highlight the differences in cation dynamics as a function of dimensionality observed in this present study.[22] Time-dependent rotational autocorrelation functions (ACF) of the $CH_3NH_3^+$ and nBA cation rotations in layered $(d{-}n\text{BA})_2(\text{MA})_{n-1}\text{Pb}_n\text{I}_{3n+1}$ (n = 1,2,3,4,∞) perovskite derivatives show the $CH_3NH_3^+$ reorientations are more restricted in the $n = 2$ compound relative to $n = 3$. With a thicker inorganic layer, there is also increased rotational freedom for the nBA cation, consistent with the competing dipole interactions between nBA and $CH_3NH_3^+$. The MA in $(d{-}n\text{BA})_2(\text{MA})\text{Pb}_2\text{I}_7$ is "flanked by two nBA layers on each side". This "flanking" leads to an electrostatic repulsion between the nBA and $CH_3NH_3^+$ cations that restricts the rotational motion of $CH_3NH_3^+$. Curiously, methylammonium rotations appear to be the least hindered when $n = 3$ at the lowest simulation temperature ($T = 50$ K), which is argued to relate to the nature of octahedral tilting. Together, these simulation results support the conclusions drawn here that the methylammonium residence time is longer in $(d{-}n\text{BA})_2(\text{MA})\text{Pb}_2\text{I}_7$ than $(d{-}n\text{BA})_2(\text{MA})_2\text{Pb}_3\text{I}_{10}$, as previously attributed to the screening effects provided by thicker inorganic layers.

The inhibition of the $CH_3NH_3^+$ C_4 reorientational motions measured in this study correlates with changes in previously measured changes in the mobility and carrier lifetime in

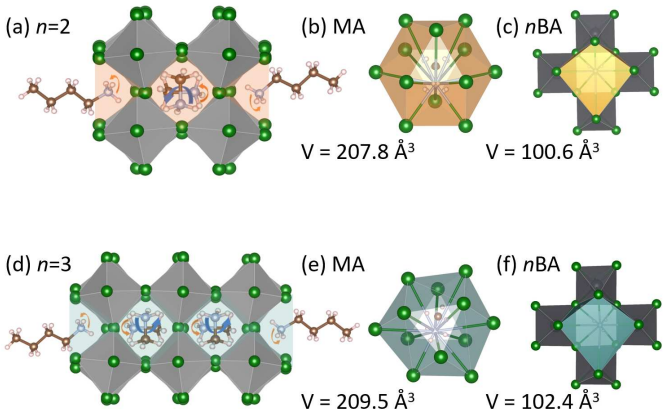

Figure 3.4: A-site voids calculated by connecting [NI_{12}] polyhedra for $CH_3NH_3^+$ (MA) and [NI_8] polyhedra for nBA. (a) $(n\text{BA})_2(\text{MA})\text{Pb}_2\text{I}_7$ ($n = 2$) with polyhedral volumes of (b) MA (207.8Å^3) and (c) nBA (100.6 Å^3) highlighted in orange. (d) $(n\text{BA})_2(\text{MA})_2\text{Pb}_3\text{I}_{10}$ ($n = 3$) with polyhedral volumes of (e) MA (209.5 Å^3) and (f) nBA (102.4 Å^3) highlighted in teal. Only one void is shown here as they are symmetry related.

the same compounds. Pulse-radiolysis time-resolved microwave conductivity (PR-TRMC) measurements were performed to determine the mobility of free carriers in a series of $(n\text{BA})_2(\text{MA})_{n-1}\text{Pb}_n\text{I}_{3n+1}$ ($n = 1 - 5$) perovskites; in summary, the thicker layers yield higher charge mobilities, as correlated with the decreased effective carrier masses.[3] In those studies, the carrier mobility and the half-lifetime of the microwave transient increase below the temperature at which we observe the methylammonium C_4 reorientations freeze out ($T < 180$ K). The temperature dependence of the PR-TRMC determined mobility follows a decrease in electron-phonon scattering. We propose that upon freezing of the methylammonium C_4 reorientations, the phonons largely responsible for carrier scattering soften, resulting in a phase transition. The absence of those low-energy inorganic vibrations then permits more mobile carriers. This is also consistent with the observation of photo-induced changes in Kerr responses in $CsPbBr_3$ and $MAPbBr_3$ on picosecond time scales[71] that is directly related to the symmetry of the inorganic phase,[72] wherein a more

dynamic cation has a higher effective radius to retain a higher-symmetry, perovskite with less octahedral tilting, as we previously noted.[65]

Density functional theory (DFT) calculations reveal how the methylammonium rotational dynamics influence the electronic band structure in layered methylammonium lead iodide perovskite materials. Most DFT calculations on these hybrid materials use structures of idealized, frozen orientations of the dynamic organic cations, yet the organic cation orientations can have significant indirect effects on the frontier electronic states.[73] In the layered hybrid perovskite derivatives, the valence band maximum has contributions from lead 6p orbitals and does not change significantly as a function of methylammonium reorientation. Yet, the conduction band minimum is has contributions from iodide 5p orbitals that can be pulled or pushed by the methylammonium molecular orientation via hydrogen bonding.[68] The methylammonium cation rotations changes the nature of the fundamental band gap from direct or indirect through coupling to the iodide orbitals by changing the degree of orbital overlap with lead.[68] This effect also produces differences in the electronic transport properties. In the case of the thermoelectric behavior, the Seebeck coefficient of the layered perovskite is more favorable for when methylammonium cations are symmetrically aligned. Additionally, the carrier mobility changes by two orders of magnitude through different methylammonium orientations, which provides an opportunity for engineering and switching by control of the organic cation orientation (e.g., with an electric field).

The results reported here provide strong experimental corroboration of molecular dynamics (MD) simulations. Molecular dynamics simulations constrained by pair-wise po-

tentials of interacting partial charges sometimes fail to capture complex phase behavior in covalent materials. Yet, these simulations capture the behavior observed in these materials. From the autocorrelation functions (ACF) of the methylammonium orientations in MD simulations of $(n\text{BA})_2(\text{MA})_{n-1}\text{Pb}_n\text{I}_{3n+1}$ (n = 2,3) reveal relaxation times of $\approx$ 2.5 ps at 300 K and $\approx$ 3.0 ps at 140 K.[22] These values are comparable to those reported here (Fig. 3.2). Further, calculations of n-butylammonium cation motion also correlate to what is modelled in the QENS data (Figure 3.3). Here, the nBA cation N-C and C-H motions are modeled as static at T $<$ 300K, akin to the plateauing of its respective ACF before 5 ps in the MD simulations.[22] The validation of modern simulation methods can enable the prediction of future materials and a deeper understanding of electronic properties.

3.6. Conclusions

Neutron scattering from the incoherent, organic cation dynamics of methylammonium and deuterated n-butylammonium in $(d{-}n\text{BA})_2(\text{MA})\text{Pb}_2\text{I}_7$ and $(d{-}n\text{BA})_2(\text{MA})_2\text{Pb}_3\text{I}_{10}$ (d-nBA = $\text{CD}_3(\text{CD}_2)_3\text{NH}_3^+$ and MA = CH_3NH_3^+) Ruddlesden-Popper perovskites reveals shorter residence times of the cations in $(d{-}n\text{BA})_2(\text{MA})_2\text{Pb}_3\text{I}_{10}$ relative to $(d{-}n\text{BA})_2(\text{MA})\text{Pb}_2\text{I}_7$. Previous computational reports corroborate the shorter residence times for CH_3NH_3^+ reorientations in $(d{-}n\text{BA})_2(\text{MA})_2\text{Pb}_3\text{I}_{10}$. The relatively static dynamics of d-nBA in these materials provides the CH_3NH_3^+ with a set of preferred orientations; however, the interactions between d-nBA and CH_3NH_3^+ are decreased upon an increase of inorganic layers leading to shorter CH_3NH_3^+ residence times. Mean-squared displacements have significant discontinuities that coincide with transitions previously reported

by differential scanning calorimetry, showing a coupling between crystal structure and organic cation dynamics. The phase transitions at $T < \approx$ 183 K in these layered materials directly correlate to a restriction of the $CH_3NH_3^+$ dynamics, where the C_4 tumbling is frozen out. The reduced $CH_3NH_3^+$ rotational dynamics also coincide with a decrease in the residence times and longer microwave conductivity decay times as is seen in the 3D counterpart, $CH_3NH_3PbI_3$. This work highlights the effect of organic cation dynamics as a geometric consideration in influencing the inorganic frameworks in hybrid semiconductors.

4. Excited State Dynamics in Isotopically Substituted Layered Perovskites[†]

4.1. Summary

The broadband emission in layered hybrid halide perovskites is attributed to the formation of self-trapped excitons within the inorganic framework. The magnitude of trapping and emission changes as a function of tilt angle. We have previously shown the organic cation dynamics influence the inorganic tilt angle. However, by eliminating tilt angle as a variable in these materials, we can more closely look at the relationship between organic cation dynamics and emission. Here, we discuss the implications of isotopic substitution in the layered hybrid halide perovskite, $(GABA)_2PbBr_4$ (GABA = 4-aminobutyric acid) that emits white light at temperatures below 200 K.

4.2. Introduction

Intrinsic white light emission has been reported in a variety of two-dimensional lead perovskites,[14,15,23,74] with the composition A_2PbX_4 where A is a NH_3^+-containing organic cation and X is a halide. This emission is theorized to arise from the broad distribution of emissive states through radiative recombination of self-trapped excitons (STEs).[2,16,34] The relevant electronic states contributing to exciton trapping reside in the inorganic layer and

[†]Author Contributions: Alexandra Koegel prepared the samples, collected and analyzed the photoluminescence data. James Neilson edited the manuscript and oversaw the project.

are affected primarily by static connectivity and out-of-plane tilting.[2,23,38] Inorganic octahedral tilting effects the capacity to self-trap excitons and produce broadband emission.[2] The static effects of the sublayers contribute to the optoelectronic properties, therefore it stands to study how their dynamics also affect properties.

Computational and experimental studies show a spatial and temporal decrease in organic cation dynamics correlates to an increase in radiative recombination of charge carriers in layered perovskites.[26,66] However, the static out-of-plane tilt angle of the inorganic octahedra is a significant variable that is unaccounted for in these studies. We eliminate tilt angle as a variable by deuterating the organic cation, 4-aminobutyric acid (GABA, d_6). By deuterating the organic cation, the speed of the dynamics of the organic cation are decreased without compromising the static structure. Thus, we can make a direct comparison between organic dynamics and broadening of the white light emission.

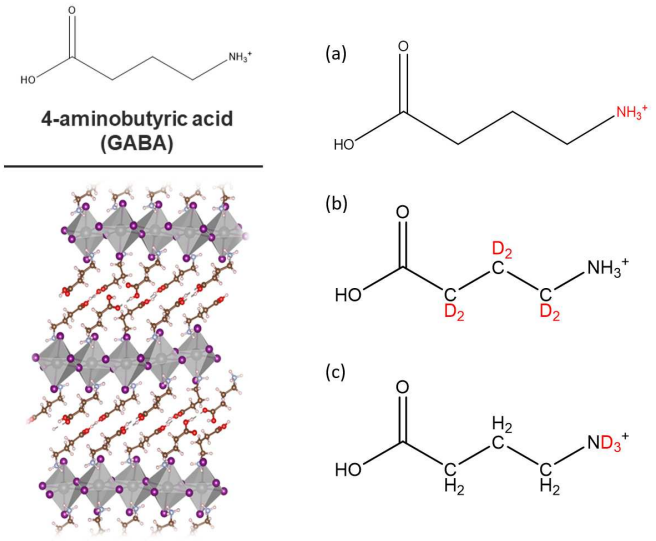

Figure 4.1: Left: Illustration of $(GABA)_2PbBr_4$ presented in this chapter. Right: (a) $(GABA)_2PbBr_4$, no deuteration, (b) $(d_6{-}GABA)_2PbBr_4$ with the carbon backbone deuterated, (c) $(GABA{-}ND_3{}^+)_2PbBr_4$ with the ammonium head group deuterated.

Here, we discuss the effects of isotope exchange on broadband photoluminescence in $(GABA)_2PbBr_4$ (Figure 4.1). We show that the slower dynamics inherent to the deuterated material lead to a slightly broader white light emission and reduced free exciton emission intensity when compared to the non-deuterated sample. The decay lifetimes are similar between the two samples and exhibit single-ensemble-like emission, where the lifetimes are not wavelength dependent after normalization to $\approx$ 170 ns. Using a harmonic oscillator calculation, we approximate the organic cation relaxation time of the deuterated material to be $\approx$ 2.8 ns, which is not significantly lengthened from the non-deuterated sample at 1.98 ns. The extrapolation of the relaxation time of the deuterated sample deuterons indicates the molecular dynamics will not be on a timescale slow enough to significantly change the excited state dynamics in layered perovskite derivatives.

4.3. Experimental

All syntheses were performed in air at room temperature. Materials were used as received from the manufacturer. Acronyms used: GABA = 4-aminobutyric acid, d-GABA = deuterated (d_6) 4-aminobutyric acid. The starting $PbBr_2$ concentrations were determined from the molar solubility of the desired product in order to maximize yield and purity.[18]

Preparation of $(GABA)_2PbBr_4$: A 0.689 M solution of $PbBr_2$ was prepared by the addition of 1.52 g (6.81 mmol) PbO in 10 mL aqueous HBr (48 wt% aqueous, Alfa Aesar). To this solution, 1.41 g (13.6 mmol) of 4-aminobutyric acid (Alfa Aesar) was added and let stir for 20 minutes. 6 mL of glacial acetic acid (60% of the total vol, Fisher Chemical, Certified ACS) was then added to the solution and let stir for a further 20 min, yielding opaque,

white, plate-like crystals. The precipitate was collected by vacuum filtration and washed with hexanes (Fisher Chemical, Certified ACS) and dried in air for 30 min. Phase purity was confirmed by powder X-ray diffraction.

Preparation of ($d-$GABA)$_2$PbBr$_4$: A 1.28 M solution of $PbBr_2$ was prepared by the addition of 2.8145 g (12.6 mmol) PbO in 10 mL aqueous HBr (48 wt% aqueous, Alfa Aesar). From this stock solution, 200 μL was extracted and added to 0.0544 g (0.498 mmol) deuterated 4-aminobutyic acid (d_6, CDN Isotopes) and let stir for 20 min. 60% of the total volume of glacial acetic acid (Fisher Chemical, Certified ACS) was then added to the solution and let stir for a further 20 min, yielding opaque, white, plate-like crystals. The precipitate was collected by vacuum filtration and washed with hexanes (Fisher Chemical, Certified ACS) and dried in air for 30 min. Phase purity was confirmed by powder X-ray diffraction.

Photoluminescence: Steady state photoluminescence data were collected on a Edinburgh FS5 spectrofluorometer using a monochromated 150W Xenon lamp with slit bandwidths of 1 nm. Samples were prepared by packing powdered samples into 250 mm x 4 mm Thin Wall Quartz EPR sample tubes and inserting the sample tube into liquid nitrogen. The samples were excited with 365 nm light and monitored over a spectral range of 385-750 nm. Background data collection was collected on an empty EPR tube excited at 365 nm and monitored over a spectral range of 385-750 nm. Time correlated single photon counting (TPSPC) photoluminescence transients were collected on an Edinburgh FS5 spectrofluorometer using a 365 nm laser diode with a 5.00 nm slit bandwidth and SC-70: Liquid Nitrogen EPR Dewar sample stage. Light was pulsed

at 500 ns intervals and collected at various wavelengths across the broad spectrum. Decay lifetimes were calculated with Fluoracle software using the biexponential equation: $R(t) = B_1 \exp(-t/\tau_1) + B_2 \exp(-t/\tau_2)$.

Powder X-ray diffraction (PXRD): Laboratory powder X-ray diffraction data were collected on a Bruker D8 Discover DaVinci powder X-ray diffractometer using Cu Kα radiation and a Lynxeye XE-T position-sensitive detector. Samples were prepared on a "zero-diffraction" Si wafer. The PXRD data were modeled with $P2_1/c$ space group for $(GABA)_2PbBr_4$ with the Rietveld method implemented in TOPAS v6 (Bruker AXS).[1]

4.4. Results and Discussion

The two $n = 1$ bromide compounds $(GABA)_2PbBr_4$ and (d−$GABA)_2PbBr_4$ (where d−GABA = $H_3N(CD_2)_3COOH_3$, Figure 4.1b) were prepared as previously described.[18] Both materials were determined phase-pure by powder X-ray diffraction (Figure 23). The materials exhibit ambient low temperature steady-state photoluminescence (PL) shown in Figure 4.2 and are comparable to those in literature for $(GABA)_2PbBr_4$.[1] There is a free exciton (FE) peak centered at $\approx$ 414 nm for both materials with no broadband emission as expected.

At $T = 77$ K, the FE emission becomes much sharper and shifts to $\approx$ 390 nm in both materials. The non-deuterated $(GABA)_2PbBr_4$ has a more intense FE peak than the deuterated material. The presence of broadband emission is observed at temperatures below 200

K[1] and is theorized to arise due to self-trapped excitons (STEs).[16] The broad STE emission is centered at ≈ 560 nm and is more intense than the FE emission.

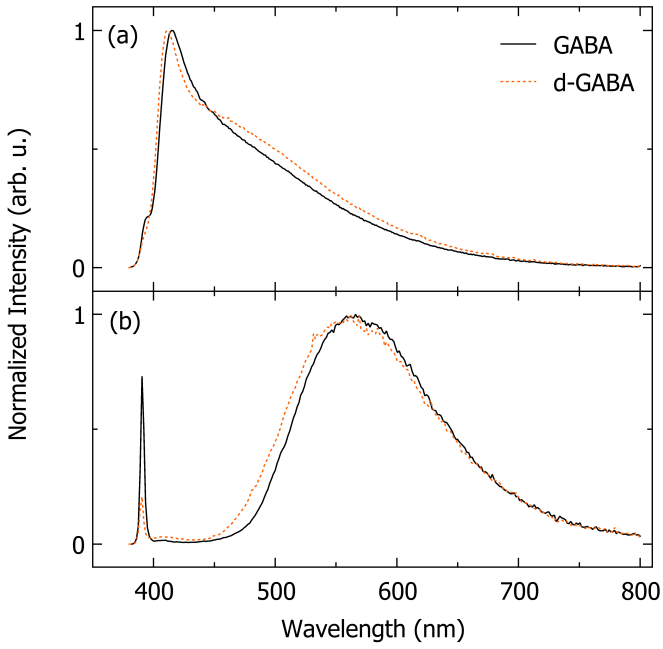

Figure 4.2: Steady-state photoluminescence at (a) 295 K and (b) 77 K of $(GABA)_2PbBr_4$ (black solid lines) and $(d{-}GABA)_2PbBr_4$ (red dashed lines). There is no broadband emission at 295 K. There is broad emission centered at ≈ 560 nm at 77 K in both samples.

A decrease in thermal population into the FE excited state explains the decrease in FE intensity at lower temperatures (Figure 24). The self-trapped excitonic (broad) emission intensity in the non-deuterated sample is relatively the same as the deuterated sample; however, the width of the deuterated sample is slightly larger than the non-deuterated sample. Single-ensemble emission from time-resolved photoluminescence is explained by an exchange between excited states;[36] where the excited state samples the rotational motion of the ammonium headgroup.[4] Multi-ensemble emission is described by no exchange between excited states (i.e., static local structures) that can be imitated by a deuterated

ammonium headgroup. However, the broadening in the deuterated material is larger than that of the non-deuterated sample, contrary to this hypothesis.

The time-resolved photoluminescence spectra are shown in Figure 4.3. While there are differences between wavelengths in relaxation times at short time scales, normalization after $\approx$ 170 ns across all wavelengths measures describes a single ensemble emission in both samples.[36] Decay lifetimes are well described by a biexponential model discussed in the methods (10).

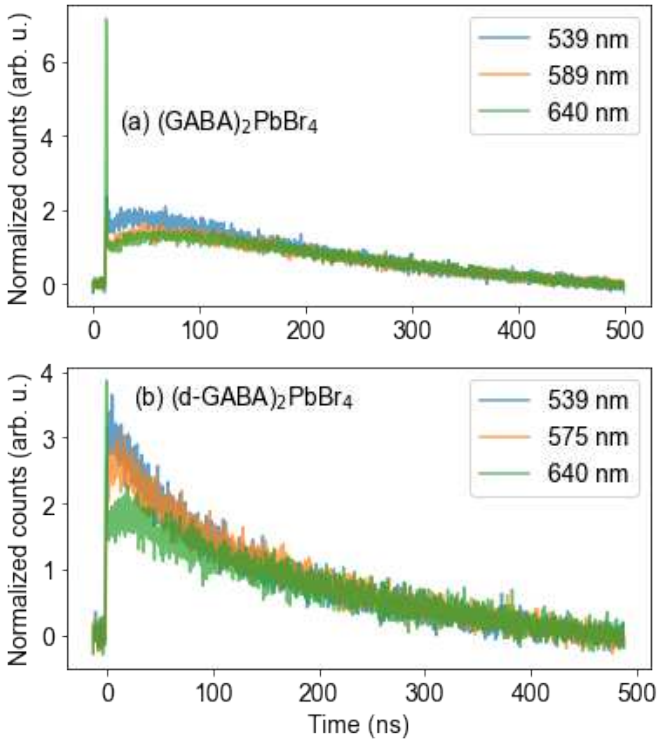

Figure 4.3: (a) Time resolved photoluminescence of (a) (GABA)2PbBr4 at 539 nm (blue), 589 nm (orange), and 640 nm (green) and (b) (d-GABA)2PbBr4 at 539 nm (blue), 575 nm (orange), and 640 nm (green) at 77 K. Data were normalized to the photoluminescence intensity at $\approx$ 170 ns.

With nominally similar excited state dynamics, we assume the molecular dynamics of 4-aminobutyric acid with a deuterated carbon backbone (Figure 4.1b) are also similar; however, it is not possible to determine them using quasi-elastic neutron scattering. The

incoherent cross section of deuterium is 2.05 barns compared to the cross section of hydrogen which is 80.2 barns, therefore the motions of deuterons will be difficult to discern via neutron scattering.[51] Additionally, deuterating the backbone does not reduce the dynamics of the ammonium headgroup that is closely coupled to the inorganic structure. We can infer the deuterated material has inherently slower dynamics; therefore, we would expect the broad emission to be narrower *if* the deuterated ammonium group rotations are significantly slower than the emission decay lifetimes.[4,36]

We can estimate the change in τ (i.e., the relaxation time of the deuterated ammonium group rotations (Figure 4.1c)) in the deuterated material by using a harmonic oscillator expression:

$$\omega_1 = \omega_2\sqrt{2}$$

to compare the masses and determine how the frequency (τ) changes based on a doubling of mass. From QENS analysis we know that τ is defined as:

$$\tau = \frac{\hbar}{\omega}$$

Therefore,

$$\tau_2 = \tau_1\sqrt{2}$$

From previous quasi-elastic neutron scattering measurements, we have extrapolated a residence time of 2 ns for GABA (τ_1).[4] Entering this into the above equation we end up with a τ_2 = 2.82 ns for GABA$-ND_3^+$. This is not significantly slower than the non-

deuterated material or the decay lifetimes; therefore, the deuteration of the organic cation will not play a large role in changing the excited state dynamics of this specific material.

4.5. Conclusions

The dynamics of the organic cation are responsible for changes in the static inorganic structure and thus the broadband emission in layered perovskite derivatives. By eliminating tilt angle as a variable by isotopically substituting deuterium for hydrogen in $(GABA)_2PbBr_4$ (GABA = 4-aminobutyric acid (d_6), we find that there is little change in the excited state dynamics. We hypothesize this is likely due to the similar rotational timescales of the ammonium headgroups that are closely coupled to the inorganic structure. Understanding of the exciton nature and effect on properties in these materials is of critical importance in guiding their further applications.

5. Organic-Inorganic Coupling Effects on Broadband Emission through Halide Substitution in Layered Perovskites[†]

5.1. Summary

Three-dimensional and layered perovskites have highly tunable structures which is advantageous for accessing specific optoelectronic properties. Although the electronic states of the organic cation are not relevant to the broadband emission observed in these materials; their arrangement with the A-site void dictates the inorganic structure and relevant electronic states. Previous experiments have ascribed the tilting of the inorganic octahedra to the organic cation dynamics that change with A-site cation substitution. However, the inorganic layer is also easily chemically substituted. Halide substitution provides an easy way to change the bandgap. In the three-dimensional $MAPbI_3$, halide substitution changes the organic cation dynamic relaxation dynamics. Crystallography and photoluminescence spectroscopy describes the red-shifting of the broadband photoluminescence that occur with halide substitution. Neutron scattering provides an explanation for the observed white light emission in the chloride and iodide analogs. The larger extent of hydrogen spatial dynamics of the bromide material occupies a larger A-site volume within

[†]Author Contributions: Alexandra Koegel prepared the samples, collected and analyzed the X-ray diffraction data and analyzed the neutron scattering data. Madhusudan Tyagi collected the neutron scattering data. Daniel Bates collected the differential scanning calorimetry data. James Neilson edited the manuscript and oversaw the project.

the octahedral framework. This satisfies the apical bromines and no tilting is required, and thus, no broadband emission is observed. The trends in A-site volume and hydrogen dynamics follow what we have previously discussed when changing the A-site cation and provide design principles for this family of layered perovskites. This work describes the role of halide substitution on cation dynamics and photoluminescence in the $(n\text{BA})_2\text{Pb}X_4$ (X = cl, Br, I) family of layered perovskites.

5.2. Introduction

Intrinsic broadband emission has been observed in (001)-layered hybrid halide perovskites.[1,14,15,39] These perovskites are comprised of single layers of inorganic octahedra templated by a large amine containing organic cation. The organic cation that sits between the inorganic octahedra influence the tilt angles of the octahedra,[1,4] which in turn influences the optoelectronic properties, and specific to this study: the broadband photoluminescence.[2] Changing the organic cation within the organic substructure influences the overall structure and thus the properties. Our previous work on $(n\text{BA})\text{PbBr}_4$, $(\text{ODA})\text{PbBr}_4$, and $(\text{GABA})_2\text{PbBr}_4$, ($n$BA = n-butylammonium, GABA = 4-aminobutyric acid, ODA = 1,8-diaminooctammonium) involving quasi-elastic neutron scattering and photoluminescence spectroscopy demonstrates how restricted organic cation dynamics induce octahedral tilting and influence the broad emission.[4] The fast ammonium rotations of the organic cations enable inhomogeneous broadening by providing multiple environments for the excited state to sample. While organic molecules template the overarching structure of these phases, it is not yet clear how the molecules influence the halogen vibrational dynamics. It

is theorized within the literature that the halide vibrations are largely responsible for the formation of self-trapped excitons within the inorganic layer of the the layered perovskites and thus the broadband emission.[2] In $MAPbI_3$, partial and complete substitution of chloride at the halide site shortens C_3 relaxation times in the low-temperature orthorhombic phase;[30] this is attributed to the shorter relaxation times from weaker H-bonding between methylammonium and the halide atoms. However, these relationships regarding the organic cation dynamics as a function of halide substitution have not yet been studied in the layered perovskites.

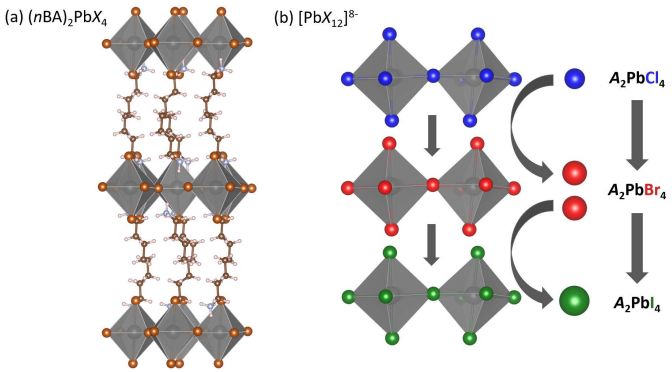

Figure 5.1: (a) Crystal structure of $(n\text{BA})_2\text{Pb}X_4$ at 298 K where nBA = n-butylammonium, Pb = gray, X = rust, N = blue, C = brown, H = pink. (b) Cartoon depiction of inorganic substructure for $(n\text{BA})_2\text{Pb}X_4$ where X = Cl (blue), Br (orange), I (green). The halide site is synthetically substituted via solution-processing by changing the lead salt that is formed in solution.

Here, we report preliminary photoluminescence spectroscopy and elastic neutron scattering data of the $(n\text{BA})_2\text{Pb}X_4$ layered perovskite derivatives, where nBA = n-butylammonium and X = Cl, Br, or I. The chloride and iodide congeners exhibit broadband "white" photoluminescence (PL) at temperatures below 200 K whereas the Br congener does not display any broadband PL. Mean-squared displacements (MSDs) calculated from fixed-window elastic neutron scattering describe the spatial extent of hydrogen dynamics. $(n\text{BA})_2\text{PbBr}_4$ has the greatest spatial extent of hydrogen dynamics, and $(n\text{BA})_2\text{PbCl}_4$ has

the least spatial extent of hydrogen dynamics at temperatures where relevant optoelectronic properties occur ($<$ 200 K). Discontinuities in the MSDs correspond to phase transitions observed by differential scanning calorimetry, illustrating that the organic cation dynamics are coupled to the phase transitions. Further experiments are necessary to definitively conclude how halide substitution influences the molecular jump relaxations of the organic cation.

5.3. Experimental

All syntheses were performed in air at room temperature. Materials were used as received from the manufacturer. Acronyms used: nBA = n-butylammonium. The starting PbX_2 concentrations were determined from the molar solubility of the desired product in order to maximize yield and purity.[18]

Synthesis of (nBA)$_2$PbCl$_4$: A 0.16 M solution of $PbCl_2$ was prepared by the addition of 3.5643 g (15.9 mmol) PbO in 100 mL aqueous HCl (Alfa Aesar). To this solution, 1.578 mL (15.9 mmol) n-butylamine (Sigma Aldrich) was titrated dropwise and stirred for 20 minutes. 60% of the total volume of glacial acetic acid (Fischer Chemical, Certified ACS) was then added to the solution and let stir for a further 20 minutes, yielding a white, opaque, microcrystalline powder. The precipitate was collected by vacuum filtration and washed with glacial acetic acid (Fischer Chemical, Certified ACS) and hexanes (Fischer Chemical, Certified ACS) and dried in air for 30 min. Phase purity was confirmed by powder X-ray diffraction.

Preparation of (nBA)$_2$PbBr$_4$:[4]A 0.301 M solution of $PbBr_2$ was prepared by the addition

of 0.689 g (3.08 mmol) PbO in 10 mL aqueous HBr (48 wt% aqueous, Alfa Aesar). To this solution, 0.610 mL (6.17 mmol) n-butylamine (Sigma-Aldrich) was titrated dropwise and stirred for 20 min, yielding an opaque, white, microcrystalline powder. The precipitate was collected by vacuum filtration and washed with glacial acetic acid (Fisher Chemical, Certified ACS), then hexanes (Fisher Chemical, Certified ACS), and dried in air for 30 min. Phase purity was confirmed by powder X-ray diffraction.

Preparation of (nBA)$_2$PbI$_4$:[18] A 0.48 M solution of PbI_2 was prepared by the addition of 0.536 g (2.4 mmol) PbO in 5 mL aqueous HI (57 wt% in H_2O, $<$1.5% H_3PO_2). To this solution, 0.238 mL (2.4 mmol) n-butylamine (Sigma Aldrich) was titrated dropwise and stirred for 20 minutes. 3 mL of glacial acetic acid (60% of the total vol, Fischer Chemical, Certified ACS) was then added to the solution and let stir for a further 20 min, yielding opaque, orange, microcrystalline powder. The precipitate was collected by vacuum filtration and washed with glacial acetic acid (Fischer Chemical, Certified ACS) and hexanes (Fischer Chemical, Certified ACS) and dried in air for 30 min. Phase purity was confirmed by powder X-ray diffraction.

Powder X-ray diffraction (PXRD): Laboratory powder X-ray diffraction data were collected on a Bruker D8 Discover DaVinci Powder X-ray Diffractometer using Cu Kα radiation and a Lynxeye XE-T position-sensitive detector. Samples were prepared on a zero-diffraction Si wafer. The PXRD data were modeled with Pbca space groups for all compounds (Figure 25) by the Rietveld method implemented in TOPAS v6 (Bruker AXS).

Photoluminescence (PL): Steady state photoluminescence data were collected on a Edinburgh FS5 spectrofluorometer using a monochromated 150W Xenon lamp with slit

bandwidths of 1 nm. Samples were prepared by packing powdered samples into 250 mm x 4 mm Thin Wall Quartz EPR sample tubes and inserting the sample tube into liquid nitrogen. The samples were excited with 350 nm light and monitored over a spectral range of 375-800 nm. Background data collection was collected on an empty EPR tube excited at 350 nm and monitored over a spectral range of 325-675 nm.

Differential scanning calorimetry (DSC): Differential scanning calorimetry (DSC) data were collected on a TA Modulated DSC 2500 with a sub-ambient accessory. Roughly 5 mg of each compound were sealed in Tzero Aluminum Hermetic pans. Samples were cycled at 10.0 °C/min from room temperature to -90.0° C (183 K), allowed to equilibrate, and ramped at 10.0° C/min to 30° C (303 K) and allowed to equilibrate. This cycle was repeated three times.

Fixed-window elastic scattering: Fixed-window elastic scattering data were collected using the high flux backscattering spectrometer (HFBS) at the NIST Center for Neutron Research on samples of nBA$_2$PbCl$_4$, nBA$_2$PbBr$_4$, and nBA$_2$PbI$_4$.[42] At HFBS, the sample environment employed in this experiment is a closed-cycle refrigerator that cools/warms the sample by helium exchange gas. The cylindrical sample cell has a diameter of approximately 3 cm, and the powder sample was held against the lateral area of the sample can by enclosing it within aluminum foil pouches. The sample cell was loaded in a helium glove box and sealed with an indium O-ring. The enclosed helium ensures good thermal contact between the powder and the rest of the sample environment. Fixed window scans were performed according to the following protocol. Initially, the samples were loaded into the sample at 295 K and cooled to 5 K. Data were continuously collected at a ramp rate of 0.7

K/min with 60 sec/point. Finally data were collected upon heating at the same nominal ramp rate and time per point. The observed scattering was normalized to the incident beam monitor. A fixed window scan is a measurement of the elastic intensity $I_{el}(Q,T)$ as a function of *Q*, momentum transfer, and temperature. The effective mean-squared displacement, $< u^2 >$, of the hydrogen atoms is estimated by assuming that $I_{el}(Q,T)$ is governed by a Debye-Waller factor: $I_{el}(Q,T) = I_{el}(Q,T=5.0K)x\exp((\frac{-Q^2<u^2>}{3}))$.[43,44] The effective mean-squared displacement quantifies the mobility of the hydrogen atoms over the experimental time window of HFBS. Given the elastic energy resolution of 0.8 μeV, the long-time limit of experimental time window is approximately 1.5 ns. This calculation was performed using the DAVE software.[45]

5.4. Results and Discussion

Samples were synthesized through solution-processing as described in the methods and confirmed phase-pure through powder X-ray diffraction (PXRD, Figure 25). Low-temperature photoluminescence measurements are shown in Figure 5.2. (nBA)$_2$PbBr$_4$ has no broadband photoluminescence at any temperature measured as previously described in literature,[1,4] with free exciton emission centered at ≈ 410 nm.

This is in between the free exciton emission of the Cl and I as expected from the band gaps. The Cl and I congener both have broadband photoluminescence centered at ≈ 510 nm and ≈ 675 nm, respectively. The broadband photoluminescence of (nBA)$_2$PbI$_4$ is red-shifted relative to (nBA)$_2$PbCl$_4$. This is in agreement with the molecular orbital di-

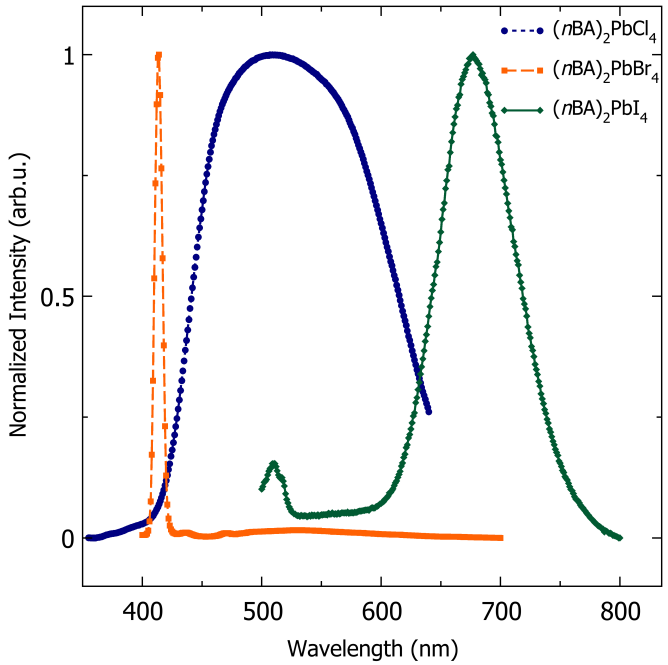

Figure 5.2: Low-temperature (77 K) normalized photoluminescence spectra from excitation at 350 nm showing broad emission centered at ≈ 525 nm for $(n\text{BA})_2\text{PbCl}_4$ (blue) and at ≈ 700 nm for $(n\text{BA})_2\text{PbI}_4$ (green). $(n\text{BA})_2\text{PbBr}_4$ (orange) does not exhibit any broadband photoluminescence at low temperatures as previously reported.[1]

agrams (Figure 5.3), the conduction band minimum (CBM) orbitals are metal p orbitals with poorer orbital overlap. The valence band maximum (VBM) is comprised of metal s and halide p orbitals and has antibonding character.[75,76] Halide substitution of iodide for chloride will change the electronic structure by lowering the VBM and increasing the bandgap. In other words, the trends in the emission follow the orbital diagram depiction, therefore, $(n\text{BA})_2\text{PbI}_4$ emission is red-shifted relative to $(n\text{BA})_2\text{PbCl}_4$. As the excited state dynamics in these materials is complex, we must take octahedral tilting into account. The increase in out-of-plane tilt stabilizes the antibonding character of the valence band gap maximum,[77] and increases the bandgap through a lowering of the valence band frontier states. The out-of-plane tilting is likely greatest in the iodide (4.4°) and the least in the bromide (2.8°); however, the tilt angle of the chloride is not known. Therefore, the degree

of out-of-plane tilting further corroborates the red-shifted $(n\text{BA})_2\text{PbI}_4$ emission relative to $(n\text{BA})_2\text{PbCl}_4$. We can assume the out-of-plane tilting in $(n\text{BA})_2\text{PbCl}_4$ is larger than that of the bromide congener due to the red-shifted broadband photoluminescence observed relative to the bromide. The out-of-plane tilting may be explained by hydrogen spatial dynamics of the nBA cation that sits in the A-site void.[4] Fixed-window elastic neutron scattering data were collected to determine the extent of hydrogen spatial dynamics in the halide-substituted series.

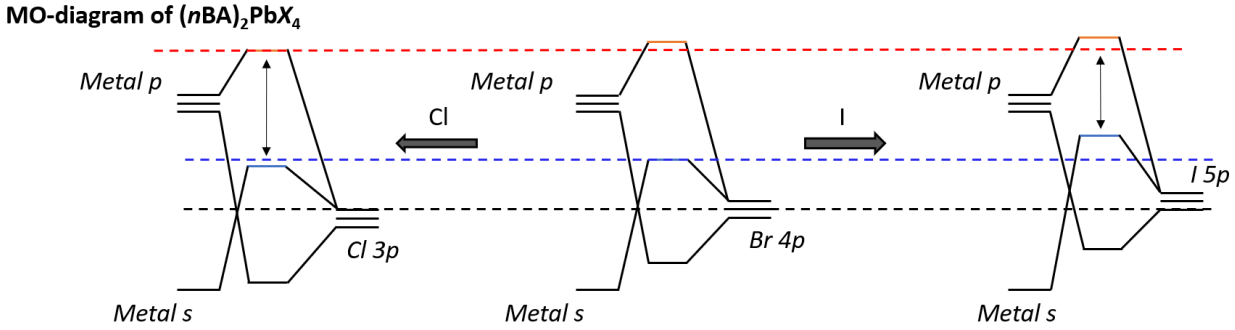

Figure 5.3: Schematic energy level diagrams, showing how halide substitution effects the valence and conduction bands in (left) $(n\text{BA})_2\text{PbCl}_4$, (middle) $(n\text{BA})_2\text{PbBr}_4$, and (right) $(n\text{BA})_2\text{PbI}_4$. The conduction band (orange dashed line) is comprised of metal and halide p orbitals and a valence band (blue dashed line) comprised of metal s and halide p orbitals. The band gap of $(n\text{BA})_2\text{PbI}_4$ is smaller than that of $(n\text{BA})_2\text{PbCl}_4$, explaining the red-shifted emission of $(n\text{BA})_2\text{PbI}_4$. The black dashed line guides the eye to orbital energy levels of the halogens.

Calculated mean-squared displacements (MSDs) from fixed-window elastic scans describe the extent of thermal motion of the nBA hydrogens (Figure 5.4) from 5 K to 300 K. $(n\text{BA})_2\text{PbBr}_4$ has the greatest spatial extent of dynamics at temperatures below $\approx$ 250 K, while $(n\text{BA})_2\text{PbCl}_4$ has the least extent of hydrogen motion at all temperatures. The extent of hydrogen motion in the organic cations in $(n\text{BA})_2\text{PbI}_4$ presented here is strongly influenced by phase transitions. There is a large discontinuity at 275 K to 250 K in the $(n\text{BA})_2\text{PbI}_4$, indicative of a large change in the dynamics of n-butylammonium cation.

Differential scanning calorimetry (Figure 27) shows phase transitions at 250 K in the $(n\text{BA})_2\text{PbI}_4$ that coincide with the discontinuity and hysteresis in the MSD (Figure 5.4).

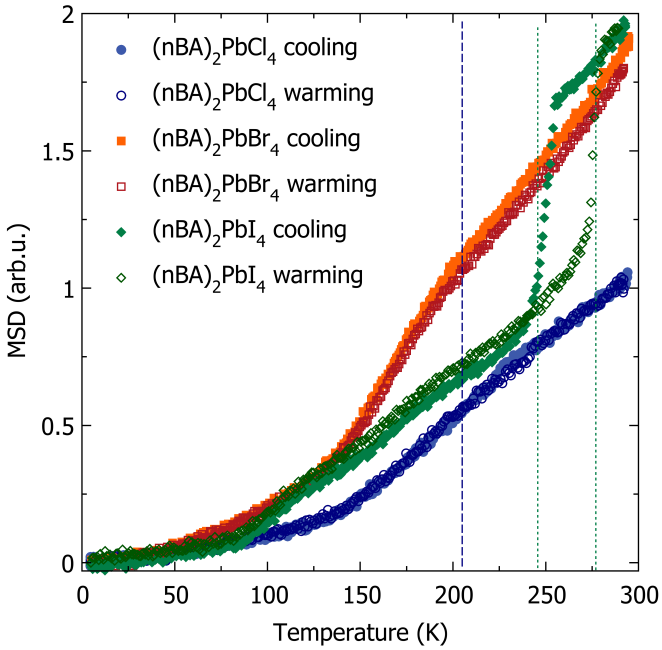

Figure 5.4: Mean squared displacements of $(n\text{BA})_2\text{PbCl}_4$ (blue), $(n\text{BA})_2\text{PbBr}_4$ (orange), and $(n\text{BA})_2\text{PbI}_4$ (green) collected from 5 K to 300 K. There is a significant discontinuity in the iodide congener, indicating the n-butylammonium dynamics change significantly upon a phase transition. Green dotted and blue dashed lines indicate transitions monitored by DSC for the I and Cl congener, respectively (Figures 27 and 26). MSD values are calculated from fixed-window elastic neutron scattering experiments (NIST, HFBS).

The A-site volumes, calculated from the [NX_8] polyhedra, determined from the 295 K crystal structures of $(n\text{BA})_2\text{PbCl}_4$, $(n\text{BA})_2\text{PbBr}_4$, and $(n\text{BA})_2\text{PbI}_4$ are 103.9 Å^3, 84.6 Å^3, and 101.9 Å^3, respectively. The $(n\text{BA})_2\text{PbCl}_4$ A-site volume is calculated from the .cif generated in TOPAS v6 from a refinement of the iodide crystal structure with the halide sites replaced. At 295 K, the $(n\text{BA})_2\text{PbI}_4$ has a greater extent of hydrogen motion indicated in the MSD relative to the $(n\text{BA})_2\text{PbBr}_4$. This agrees with our previous assignment of larger polyhedral volumes corresponding to a greater extent of hydrogen dynamics;[4] however, the chloride has the largest polyhedral volume with the least extent of hydrogen dynamics.

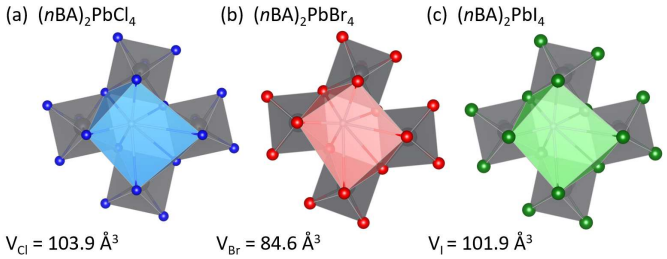

Figure 5.5: A-site volume (illustrated by the [NX_8] polyhedra) determined from the 295 K crystal structures of (a) $(n\text{BA})_2\text{PbCl}_4$, 103.9 Å^3 (b)$(n\text{BA})_2\text{PbBr}_4$, 84.6 Å^3, and (c) $(n\text{BA})_2\text{PbI}_4$, 101.9 Å^3.

5.5. Conclusions

The lesser extent of cation hydrogen spatial dynamics in $(n\text{BA})_2\text{PbCl}_4$ and $(n\text{BA})_2\text{PbI}_4$ relative to $(n\text{BA})_2\text{PbBr}_4$ correspond to broadband emission at temperatures where relevant optoelectronic properties occur ($<$ 200 K). The extent of hydrogen spatial dynamics at 295 K align with previous reports where larger polyhedral volumes correspond to more dynamic organic cations. The phase transitions occurring between 275 K and 250 K affect the nBA cation dynamics in $(n\text{BA})_2\text{PbI}_4$ as shown in the mean-squared displacement. Further studies are needed to reach definitive conclusions about the role of the halide on hydrogen spatial dynamics in layered hybrid halide perovskites. Quasi-elastic neutron scattering (QENS) studies will inform on the type and timescale of rotational dynamics of nBA as a function of temperature and halide species. Low-temperature single crystal studies on $(n\text{BA})_2\text{PbCl}_4$ will provide data to calculate tilt angles and polyhedral volumes to compare to the Br and I analogs. Finally, time-resolved photoluminescence data on all three compounds will demonstrate how the excited state dynamics of the self-trapped exciton behave when the halide is substituted in the structure. This work highlights the critical

role chemical substitution plays on organic cation dynamics and subsequent optoelectronic properties of layered hybrid halide perovskites.

6. Structural Dynamics in Broadband Emitting Solid Solutions[†]

6.1. Summary

White light in layered materials is typically only observed at temperatures below 200 K. There are instances where cation selection can induce the correct structure to emit white light at room temperature. Furthermore, solid-solutions of mixed halide layered perovskites have bee shown to emit white light at room temperatures. How the organic cation dynamics of these materials are playing a role is not understood.

6.2. Introduction

Broadband white light emission at room temperature is rare and of interest for numerous solid-state lighting applications. White light emission is typically observed at temperatures below 200 K. However there are a few cations that can emit white light at room temperature.[34] Furthermore, solid solutions of halides can also induce white light emission at ambient temperatures. The extent of white light emission is typically dictated by the octahedral tilt angle (deviation from 180 bond). By inducing a larger tilt or forcing corrugation of the octahedra, white light can be observed. We have previously shown the

[†]Author Contributions: Alexandra Koegel prepared the samples, collected and analyzed the X-ray diffraction and photoluminescence data, and analyzed the neutron scattering data. Madhusudan Tyagi collected the neutron scattering data. James Neilson edited the manuscript and oversaw the project.

dynamics influence the inorganic structure and thus the optoelectronic properties. The hydrogen dynamics of benzylammonium have not been investigated in the solid solution series $(BZA)_2PbCl_{4-x}Br_x$ (Figure 6.1) with their reported optoelectronic properties. The hydrogen dynamics of the organic cations in the halide solution series of $(BZA)_2PbCl_{4-x}Br_x$ are reported here.

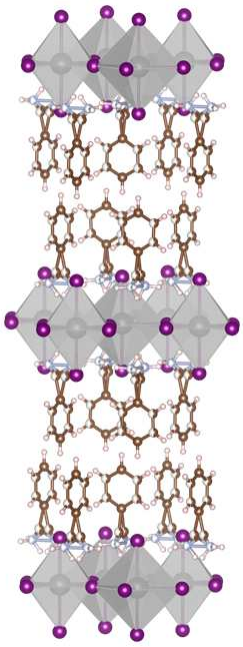

Figure 6.1: Crystal structure of $(BZA)_2PbCl_{4-x}Br_x$at 298 K where BZA = benzylammonium, Pb = gray, X = purple, N = blue, C = brown, H = pink. The halide site is synthetically substituted via solution-processing by changing the lead salt that is formed in solution. The solid solution is formed via solid-state synthesis.

6.3. Experimental

All syntheses were performed in air at room temperature. Materials were used as received from the manufacturer. Acronyms used: BZA = benzylammonium. The starting PbX_2 concentrations were determined from the molar solubility of the desired product in order to maximize yield and purity.[18]

Preparation of $(BZA)_2PbCl_4$:[78] A 0.106 M solution of $PbCl_2$ was prepared by the addition of 0.2359 g (1.06 mmol) PbO in 10 mL aqueous HCl (Alfa Aesar). To this solution, 0.230 mL benzylammonium (Sigma Aldrich) was titrated dropwise and stirred for 20 min. 60% of the total volume of glacial acetic acid (Fischer Chemical, Certified ACS) was then added to the solution and let stir for a further 20 min, yielding a white, opaque, microcrystalline powder. The precipitate was collected by vacuum filtration and washed with glacial acetic acid (Fischer Chemical, Certified ACS) and hexanes (Fischer Chemical, Certified ACS) and dried in air for 30 min. Phase purity was confirmed by powder X-ray diffraction.

Preparation of $(BZA)_2PbBr_4$:[78] A 0.106 M solution of $PbBr_2$ was prepared by the addition of 0.2343 g (1.05 mmol) PbO in 10 mL aqueous HBr (48 wt% aqueous, Alfa Aesar). To this solution, 0.230 mL benzylammonium (Sigma-Aldrich) was titrated dropwise and stirred for 20 min, yielding an opaque, white, microcrystalline powder. The precipitate was collected by vacuum filtration and washed with glacial acetic acid (Fisher Chemical, Certified ACS), then hexanes (Fisher Chemical, Certified ACS), and dried in air for 30 min. Phase purity was confirmed by powder X-ray diffraction.

Synthesis of $(BZA)_2PbBr_2Cl_2$:[78] A solid solution of $(BZA)_2PbBr_4$ and $(BZA)_2PbCl_4$ was prepared by grinding a 1:1 ratio (0.1082 g $(BZA)_2PbCl_4$, 0.1423 g $(BZA)_2PbBr_4$) of the pure end members in a mortar and pestle. This powder was then pressed into pellet and sealed in 10x12 quartz tube. The sealed tube with the pellet was placed in a box furnace and set to a ramp rate at 10 °C/min to reach a set temperature of 200 °C. The pellet was held at 200 °C for 12 hrs and slow cooled to room temperature. Phase purity confirmed by powder X-ray diffraction.

Powder X-ray diffraction (PXRD): Laboratory powder X-ray diffraction data were collected on a Bruker D8 Discover DaVinci Powder X-ray Diffractometer using Cu Kα radiation and a Lynxeye XE-T position-sensitive detector. Samples were prepared on a zero-diffraction Si wafer. The Rietveld method implemented in TOPAS v6 (Bruker AXS).

Photoluminescence (PL): Steady state photoluminescence data were collected on a Edinburgh FS5 spectrofluorometer using a monochromated 150W Xenon lamp with slit bandwidths of 1 nm. Samples were prepared by packing powdered samples into 250 mm x 4 mm Thin Wall Quartz EPR sample tubes and inserting the sample tube into liquid nitrogen. The samples were excited with 350 nm light and monitored over a spectral range of 385-750 nm. Background data collection was collected on an empty EPR tube excited at 350 nm and monitored over a spectral range of 325-675 nm.

Fixed-window elastic scattering: Fixed-window elastic scattering data were collected using the high flux backscattering spectrometer (HFBS) at the NIST Center for Neutron Research on samples of $(BZA)_2PbCl_4$, $(BZA)_2PbBr_4$, and $(BZA_2PbCl_2Br_2$.[42] At HFBS, the sample environment employed in this experiment is a closed-cycle refrigerator that cools/warms the sample by helium exchange gas. The cylindrical sample cell has a diameter of approximately 3 cm, and the powder sample was held against the lateral area of the sample can by enclosing it within aluminum foil pouches. The sample cell was loaded in a helium glove box and sealed with an indium O-ring. The enclosed helium ensures good thermal contact between the powder and the rest of the sample environment. Fixed window scans were performed according to the following protocol. Initially, the samples were loaded into the sample at 295 K and cooled to 5 K. Data were continuously collected at a ramp rate of

0.7 K/min with 60 sec/point. Finally data were collected upon heating at the same nominal ramp rate and time per point. The observed scattering was normalized to the incident beam monitor. A fixed window scan is a measurement of the elastic intensity $I_{el}(Q,T)$ as a function of *Q*, momentum transfer, and temperature. The effective mean-squared displacement, $< u^2 >$, of the hydrogen atoms is estimated by assuming that $I_{el}(Q,T)$ is governed by a Debye-Waller factor: $I_{el}(Q,T) = I_{el}(Q,T=5.0K)x\exp((\frac{-Q^2<u^2>}{3}))$.[43,44] The effective mean-squared displacement quantifies the mobility of the hydrogen atoms over the experimental time window of HFBS. Given the elastic energy resolution of 0.8 μeV, the long-time limit of experimental time window is approximately 1.5 ns. This calculation was performed using the DAVE software.[45]

6.4. Results and Discussion

End-members and the 50:50 solid solution were confirmed phase pure by PXRD (Figures 28, 29, 30). The photoluminescence (PL) measured at room temperature (Figure 6.2, left panel), shows white light emission from the mixed halide solid solution at 500 nm centered with the chloride conger free exciton emission. The free exciton peaks of the bromide is red shifted relative to the mixed halide. The bromide has no broad emission until cooled to 77 K. At low temperatures (Figure 6.2, right panel), the bromide and mixed halide congers have sharp free exciton peaks centered at 405 and 390 nm, respectively. All materials exhibit broadband emission with the bromide emission (600 nm) being red-shifted relative to the mixed halide (525 nm). The chloride has less defined broad emission centered at roughly 500 nm. The broadband emission at room temperature of the mixed halide is

reported in the literature,[78] as being caused by the increased octahedral tilting that arises with halide mixing.

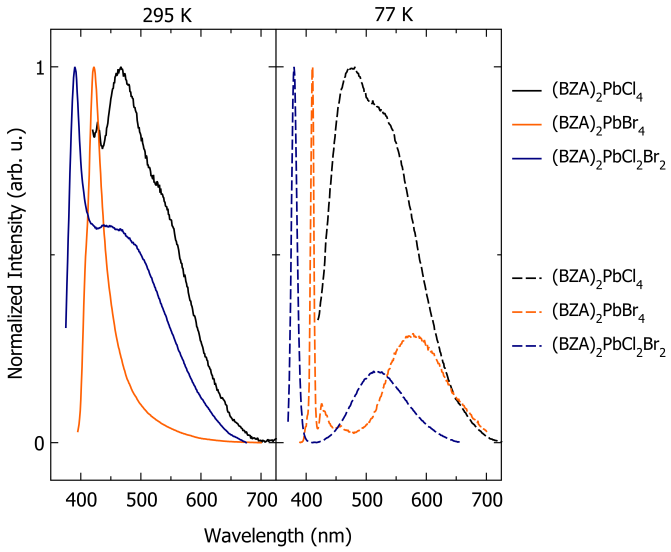

Figure 6.2: (Left) Ambient (295 K) and (Right) Low-temperature (77 K) normalized photoluminescence spectra from excitation at 350 nm for $(BZA)_2PbCl_4$ (black), $(BZA)_2PbBr_4$ (orange), and $(BZA)_2PbCl_{4-x}Br_x$ (blue).

The mean-squared displacements (MSDs) (Figure 6.3) show the solid solution has the greatest extent of hydrogen motion and the bromide the least at room temperature. At lower temperatures where broad emission is observed in all materials ($\leq$ 200 K) the bromide hydrogen spatial motion increases and the chloride and mixed halide are relatively similar. The mixed halide material exhibiting the greatest amount of hydrogen dynamics is contradictory to what we have previously found in white light emitting materials.[4] The material with the largest tilt angle (mixed halide) has the greatest extent of hydrogen motion.

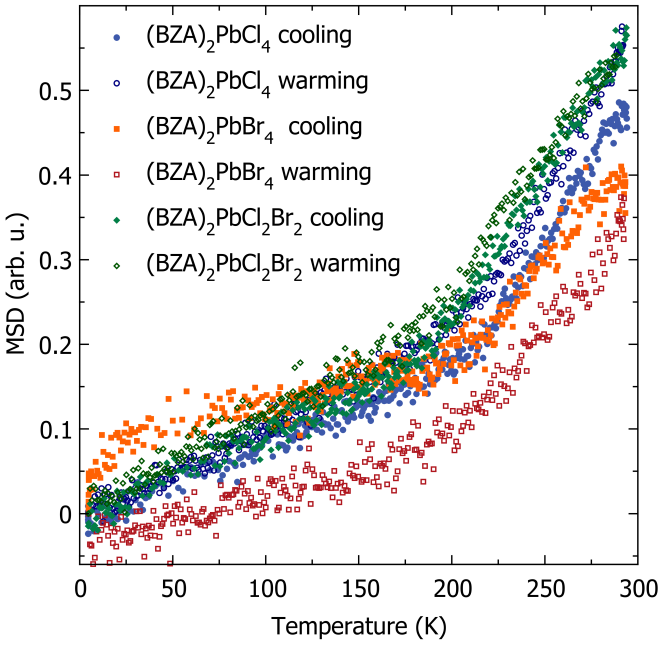

Figure 6.3: Mean squared displacements of $(BZA)_2PbCl_4$ (blue), $(BZA)_2PbBr_4$ (orange), and $(BZA)_2PbCl_{4-x}Br_x$ (green) collected from 5 K to 300 K. There are no significant discontinuities in the MSD, indicating the benzylammonium dynamics do not change significantly upon a phase transition. The extent of dynamics do not follow previous trends,[4] in that the material with broad emission at ambient temperatures does not have the least extent of dynamics at 300 K. MSD values are calculated from fixed-window elastic neutron scattering experiments (NIST, HFBS).

6.5. Conclusions

The solid solution series $(BZA)_2PbCl_{4-x}Br_x$ x = 0, 0.5, 1 has been prepared and characterized by powder X-ray diffraction, photoluminescence, and fixed-window neutron scattering. The mixed halide solid solution exhibit the reported broadband photoluminescence at room temperature. The mixed halide solution has the largest tilt angle and the greatest extent of hydrogen dynamics of the three samples, which is contradictory to our previous findings. Further neutron scattering studies will be needed to confirm the role of the organic cation in the A-site void in the $(BZA)_2PbCl_{4-x}Br_x$ series.

7. Conclusion

7.1. Summary

Structure-property-dynamics relationships influence design principles for applications in materials science. Optoelectronic properties and organic cation dynamics are coupled in three-dimensional perovskites but have not been studied in depth in layered perovskites. The conclusions reached in this dissertation describe how the cation dynamics influence the inorganic structure and observed properties in $(A')_2(A)_{n-1}B_nX_{3n+1}$ perovskite derivatives. General trends reported here show how the restricted cation dynamics, characterized by quasi-elastic neutron scattering, correlate to smaller calculated crystallographic A-site volumes in the inorganic layer. Furthermore, the organic cation dynamics were found to influence the excited state and properties, namely, broadband emission. The rotational dynamics are on faster timescales than the excited state recombination; allowing for the excited state to sample multiple electronic environments which causes to inhomogeneous broadening. The dynamics become more complex upon the introduction of multiple layers and the addition of a second organic cation. The cation rotational dynamics, while similar in their type of motion, are faster in materials with more inorganic layers. The screening effects seen when a greater number of cations are introduced with the additional octahedra and larger A-volume are attributed to the shorter residence times. The restriction of the C_4 rotational dynamics of the smaller organic cation correlate to phase transitions

observed by differential scanning calorimetry and time-resolved microwave conductivity signals.

The optoelectronic properties are also heavily influenced by substitution of the individual substructures, which is easily achieved via solution chemistry. To avoid tilt angle as a competing variable, isotopic substitution can be utilized to allow for a more direct comparison between the cation dynamics and emission. The broad emission is still influenced when isotopic substitution of the ammonium headgroup is implemented, even though experimentally derived calculations reveal there is little influence on the cation dynamics when isotopes are introduced. Halide substitution in Chapters five and six is characterized with quasi-elastic neutron scattering. These studies describe opposite trends; where in the fully substituted materials, the dynamics are restricted in materials with broad emission, following general trends of previous chapters. Conversely, in solid-solutions, the organic cations in materials with white light emission have the greatest extent of hydrogen dynamics.

7.2. Outlook

As previously mentioned,[79] the fluorimeter in the Analytical Resource Core only has the ability for liquid nitrogen and room temperature measurements. Temperature-dependent photoluminescence would increase our understanding of cation dynamics. The dynamics of the cations in the solid-solutions of $(BZA)_2PbCl_xBr_{1-x}$ (BZA = benzylammonium) could be probed with Raman spectroscopy as a function of x and correlated to the distribution of emmissive states seen with variations of halide substitution. Preliminary

mean-squared displacement and photoluminescence data have been collected and analyzed on $(n\text{BA})_2\text{Pb}X_4$ (n-butylammonium, X = Cl,Br,I). The neutron beamtime proposal (ID# 28190) has been accepted as of July 2021 for 2.0 days on NG-4, DSC, Disk-chopper time-of-flight spectrometer (DSC) to collect QENS data. The analysis and publication of the dynamics in $(n\text{BA})_2\text{Pb}X_4$ (X = Cl,Br,I) was delayed owing to a shutdown of the research reactor on the National Institute of Standards and Technology campus in Gaithersburg, Maryland. According to their website (and emails received via the beam allocation committee) the reactor will remain in shutdown status "until the cause of the elevated radiation level is determined and corrected." As these experiments will be delayed, single-crystal X-ray diffraction of $(n\text{BA})_2\text{PbCl}_4$ at room and low temperatures will provide the necessary data to calculate tilt angles and polyhedral volumes to compare to the Br and I analogs. Finally, time-resolved photoluminescence data on all halide substituted compounds will demonstrate how the excited state dynamics of the self-trapped exciton behave when the halide is substituted in the inorganic substructure.

7.3. Remaining Open Questions

The reduced dimensionality of the layered perovskites leaves open questions regarding their dynamic-structure-property relationships. Edge states and dangling bonds on the crystallographic perimeter of two-dimensional perovskites has implications in the underlying photophysics in these materials.[80] How the cation dynamics at the edges of the organic sublayers influence charge carrier recombination is of interest for their numerous applications in photovoltaics as stable alternatives to the three-dimensional perovskite. Further-

more, there is variation of properties between samples of the same material. Single crystal spectroscopy is required to elucidate the variations between samples.

If the dimensionality is further reduced to one-dimensional chains of inorganic octahedra surrounded by organic cations are the dynamics still coupled in the same way? There have been studies on the white light emission from 1D materials, both intrinsic and substituted;[81–83] yet, is unclear if the excitonic manifolds are still being influenced by the dynamics of the organic cation as they are no longer closely coupled. These initial studies on the correlations between structural dynamics in hybrid halide perovskites and optoelectronic properties depict a rich chemistry in need of further exploration.

Bibliography

[1] Smith, M. D.; Jaffe, A.; Dohner, E. R.; Lindenberg, A. M.; Karunadasa, H. I. Structural origins of broadband emission from layered Pb-Br hybrid perovskites. *Chemical Science* **2017**, *8*, 4497–4504.

[2] Yu, Z.-G. Optical deformation potential and self-trapped excitons in 2D hybrid perovskites. *Physical Chemistry Chemical Physics* **2019**, *21*, 22293–22301.

[3] Gélvez-Rueda, M. C.; Hutter, E. M.; Cao, D. H.; Renaud, N.; Stoumpos, C. C.; Hupp, J. T.; Savenije, T. J.; Kanatzidis, M. G.; Grozema, F. C. Interconversion between Free Charges and Bound Excitons in 2D Hybrid Lead Halide Perovskites. *The Journal of Physical Chemistry C* **2017**, *121*, 26566–26574.

[4] Koegel, A. A.; Mozur, E. M.; Oswald, I. W. H.; Jalarvo, N. H.; Prisk, T. R.; Tyagi, M.; Neilson, J. R. Correlating Broadband Photoluminescence with Structural Dynamics in Layered Hybrid Halide Perovskites. *Journal of the American Chemical Society 144*, 1313–1322, Publisher: American Chemical Society.

[5] Hu, X.; Zhang, D.; Chen, T.; Chen, A. Z.; Holmgren, E. N.; Zhang, Q.; Pajerowski, D. M.; Yoon, M.; Xu, G.; Choi, J. J.; Lee, S.-H. Crystal structures and rotational dynamics of a two-dimensional metal halide perovskite $(OA)_2PbI_4$. *The Journal of Chemical Physics* **2020**, *152*, 014703.

[6] Soe, C. M. M. et al. Structural and thermodynamic limits of layer thickness in 2D halide perovskites. *Proceedings of the National Academy of Sciences* **2018**, 58–66.

[7] Nakamura, S.; Mukai, T.; Senoh, M. Candela-class high-brightness InGaN/AlGaN double-heterostructure blue-light-emitting diodes. *Applied Physics Letters 64*, 1687–1689, Publisher: American Institute of Physics.

[8] Kido, J.; Kimura, M.; Nagai, K. Multilayer White Light-Emitting Organic Electroluminescent Device. *Science 267*, 1332–1334, Publisher: American Association for the Advancement of Science.

[9] Ye, S.; Xiao, F.; Pan, Y. X.; Ma, Y. Y.; Zhang, Q. Y. Phosphors in phosphor-converted white light-emitting diodes: Recent advances in materials, techniques and properties. *Materials Science and Engineering: R: Reports 71*, 1–34.

[10] Wong, M. Y.; Zysman-Colman, E. Purely Organic Thermally Activated Delayed Fluorescence Materials for Organic Light-Emitting Diodes. *Advanced Materials 29*, 1605444, _eprint: https://onlinelibrary.wiley.com/doi/pdf/10.1002/adma.201605444.

[11] Thejo Kalyani, N.; Dhoble, S. J. Novel materials for fabrication and encapsulation of OLEDs. *Renewable and Sustainable Energy Reviews 44*, 319–347.

[12] Kojima, A.; Teshima, K.; Shirai, Y.; Miyasaka, T. Organometal Halide Perovskites as Visible-Light Sensitizers for Photovoltaic Cells. *Journal of the American Chemical Society 131*, 6050–6051, Publisher: American Chemical Society.

[13] Gong, X.; Voznyy, O.; Jain, A.; Liu, W.; Sabatini, R.; Piontkowski, Z.; Walters, G.; Bappi, G.; Nokhrin, S.; Bushuyev, O.; Yuan, M.; Comin, R.; McCamant, D.; Kelley, S. O.; Sargent, E. H. Electron–phonon interaction in efficient perovskite blue emitters. *Nature Materials 17*, 550–556, Number: 6 Publisher: Nature Publishing Group.

[14] Dohner, E. R.; Hoke, E. T.; Karunadasa, H. I. Self-Assembly of Broadband White-Light Emitters. *Journal of the American Chemical Society* **2014**, *136*, 1718–1721.

[15] Dohner, E. R.; Jaffe, A.; Bradshaw, L. R.; Karunadasa, H. I. Intrinsic White-Light Emission from Layered Hybrid Perovskites. *Journal of the American Chemical Society* **2014**, *136*, 13154–13157.

[16] Hu, T.; Smith, M. D.; Dohner, E. R.; Sher, M.-J.; Wu, X.; Trinh, M. T.; Fisher, A.; Corbett, J.; Zhu, X. Y.; Karunadasa, H. I.; Lindenberg, A. M. Mechanism for Broadband White-Light Emission from Two-Dimensional (110) Hybrid Perovskites. *The Journal of Physical Chemistry Letters* **2016**, *7*, 2258–2263.

[17] Xing, G.; Mathews, N.; Lim, S. S.; Yantara, N.; Liu, X.; Sabba, D.; Grätzel, M.; Mhaisalkar, S.; Sum, T. C. Low-temperature solution-processed wavelength-tunable perovskites for lasing. *Nature Materials 13*, 476–480, Number: 5 Publisher: Nature Publishing Group.

[18] Oswald, I. W. H.; Koegel, A. A.; Neilson, J. R. General Synthesis Principles for Ruddlesden–Popper Hybrid Perovskite Halides from a Dynamic Equilibrium. *Chemistry of Materials* **2018**, *30*, 8606–8614.

[19] Stoumpos, C. C.; Cao, D. H.; Clark, D. J.; Young, J.; Rondinelli, J. M.; Jang, J. I.; Hupp, J. T.; Kanatzidis, M. G. Ruddlesden–Popper Hybrid Lead Iodide Perovskite 2D Homologous Semiconductors. *Chemistry of Materials 28*, 2852–2867, Publisher: American Chemical Society.

[20] Pelant, I.; Valenta, J. *Luminescence Spectroscopy of Semiconductors*; Oxford University Press.

[21] Williams, R. T.; Song, K. S. The self-trapped exciton. *Journal of Physics and Chemistry of Solids* **1990**, *51*, 679–716.

[22] Fridriksson, M. B.; Maheshwari, S.; Grozema, F. C. Structural Dynamics of Two-Dimensional Ruddlesden–Popper Perovskites: A Computational Study. *The Journal of Physical Chemistry C* **2020**, *124*, 22096–22104.

[23] Cortecchia, D.; Neutzner, S.; Srimath Kandada, A. R.; Mosconi, E.; Meggiolaro, D.; De Angelis, F.; Soci, C.; Petrozza, A. Broadband Emission in Two-Dimensional Hybrid Perovskites: The Role of Structural Deformation. *Journal of the American Chemical Society* **2017**, *139*, 39–42.

[24] Fu, Y.; Hautzinger, M. P.; Luo, Z.; Wang, F.; Pan, D.; Aristov, M. M.; Guzei, I. A.; Pan, A.; Zhu, X.; Jin, S. Incorporating Large A Cations into Lead Iodide Perovskite Cages: Relaxed Goldschmidt Tolerance Factor and Impact on Exciton–Phonon Interaction. *ACS Central Science* **2019**, *5*, 1377–1386.

[25] Mao, L.; Wu, Y.; Stoumpos, C. C.; Wasielewski, M. R.; Kanatzidis, M. G. White-Light Emission and Structural Distortion in New Corrugated Two-Dimensional Lead Bromide Perovskites. *Journal of the American Chemical Society 139*, 5210–5215, Publisher: American Chemical Society.

[26] Ghosh, D.; Neukirch, A. J.; Tretiak, S. Optoelectronic Properties of Two-Dimensional Bromide Perovskites: Influences of Spacer Cations. *The Journal of Physical Chemistry Letters* **2020**, *11*, 2955–2964.

[27] Mozur, E. M.; Hope, M. A.; Trowbridge, J. C.; Halat, D. M.; Daemen, L. L.; Maughan, A. E.; Prisk, T. R.; Grey, C. P.; Neilson, J. R. Cesium Substitution Disrupts Concerted Cation Dynamics in Formamidinium Hybrid Perovskites. *Chemistry of Materials* **2020**, *32*, 6266–6277.

[28] Mozur, E. M.; Maughan, A. E.; Cheng, Y.; Huq, A.; Jalarvo, N.; Daemen, L. L.; Neilson, J. R. Orientational Glass Formation in Substituted Hybrid Perovskites. *Chemistry of Materials* **2017**, *29*, 10168–10177.

[29] Chen, T.; Foley, B. J.; Ipek, B.; Tyagi, M.; Copley, J. R. D.; Brown, C. M.; Choi, J. J.; Lee, S.-H. Rotational dynamics of organic cations in the $CH_3NH_3PbI_3$ perovskite. *Physical Chemistry Chemical Physics* **2015**, *17*, 31278–31286.

[30] Schuck, G.; Lehmann, F.; Ollivier, J.; Mutka, H.; Schorr, S. Influence of Chloride Substitution on the Rotational Dynamics of Methylammonium in MAPbI3–xClx Perovskites. *The Journal of Physical Chemistry C* **2019**, *123*, 11436–11446.

[31] Ye, S.; Xiao, F.; Pan, Y. X.; Ma, Y. Y.; Zhang, Q. Y. Phosphors in phosphor-converted white light-emitting diodes: Recent advances in materials, techniques and properties. *Materials Science and Engineering: R: Reports* **2010**, *71*, 1–34.

[32] George, N. C.; Denault, K. A.; Seshadri, R. Phosphors for Solid-State White Lighting. *Annual Review of Materials Research* **2013**, *43*, 481–501.

[33] Smith, M. D.; Karunadasa, H. I. White-Light Emission from Layered Halide Perovskites. *Accounts of Chemical Research* **2018**, *51*, 619–627.

[34] Yangui, A.; Garrot, D.; Lauret, J. S.; Lusson, A.; Bouchez, G.; Deleporte, E.; Pillet, S.; Bendeif, E. E.; Castro, M.; Triki, S.; Abid, Y.; Boukheddaden, K. Optical Investigation of Broadband White-Light Emission in Self-Assembled Organic–Inorganic Perovskite $(C_6H_{11}NH_3)_2PbBr_4$. *The Journal of Physical Chemistry C* **2015**, *119*, 23638–23647.

[35] Thirumal, K.; Chong, W. K.; Xie, W.; Ganguly, R.; Muduli, S. K.; Sherburne, M.; Asta, M.; Mhaisalkar, S.; Sum, T. C.; Soo, H. S.; Mathews, N. Morphology-Independent Stable White-Light Emission from Self-Assembled Two-Dimensional Perovskites Driven by Strong Exciton–Phonon Coupling to the Organic Framework. *Chemistry of Materials* **2017**, *29*, 3947–3953.

[36] Thomaz, J. E.; Lindquist, K. P.; Karunadasa, H. I.; Fayer, M. D. Single Ensemble Non-exponential Photoluminescent Population Decays from a Broadband White-Light-Emitting Perovskite. *Journal of the American Chemical Society* **2020**, *142*, 16622–16631.

[37] Li, X.; Guo, P.; Kepenekian, M.; Hadar, I.; Katan, C.; Even, J.; Stoumpos, C. C.; Schaller, R. D.; Kanatzidis, M. G. Small Cyclic Diammonium Cation Templated (110)-Oriented 2D Halide (X = I, Br, Cl) Perovskites with White-Light Emission. *Chemistry of Materials* **2019**, *31*, 3582–3590.

[38] Mao, L.; Wu, Y.; Stoumpos, C. C.; Wasielewski, M. R.; Kanatzidis, M. G. White-Light Emission and Structural Distortion in New Corrugated Two-Dimensional Lead Bromide Perovskites. *Journal of the American Chemical Society* **2017**, *139*, 5210–5215.

[39] Jung, M.-H. White-Light Emission from the Structural Distortion Induced by Control of Halide Composition of Two-Dimensional Perovskites ($(C_6H_5CH_2NH_3)_2PbBr_{4-x}Cl_x$). *Inorganic Chemistry* **2019**, *58*, 6748–6757.

[40] Booker, E. P.; Thomas, T. H.; Quarti, C.; Stanton, M. R.; Dashwood, C. D.; Gillett, A. J.; Richter, J. M.; Pearson, A. J.; Davis, N. J. L. K.; Sirringhaus, H.; Price, M. B.; Greenham, N. C.; Beljonne, D.; Dutton, S. E.; Deschler, F. Formation of Long-Lived Color Centers for Broadband Visible Light Emission in Low-Dimensional Layered Perovskites. *Journal of the American Chemical Society* **2017**, *139*, 18632–18639.

[41] Momma, K.; Izumi, F. VESTA: A Three-Dimensional Visualization System for Electronic and Structural Analysis. *Journal of Applied Crystallography - J APPL CRYST* **2008**, *41*, 653–658.

[42] Meyer, A.; Dimeo, R. M.; Gehring, P. M.; Neumann, D. A. The high-flux backscattering spectrometer at the NIST Center for Neutron Research. *Review of Scientific Instruments* **2003**, *74*, 2759–2777.

[43] Zorn, R. On the evaluation of neutron scattering elastic scan data. *Nuclear Instruments and Methods in Physics Research Section A: Accelerators, Spectrometers, Detectors and Associated Equipment* **2009**, *603*, 439–445.

[44] Zorn, R. Multiple scattering correction of neutron scattering elastic scans. *Nuclear Instruments and Methods in Physics Research Section A: Accelerators, Spectrometers, Detectors and Associated Equipment* **2007**, *572*, 874–881.

[45] Azuah, R. T.; Kneller, L. R.; Qiu, Y.; Tregenna-Piggott, P. L. W.; Brown, C. M.; Copley, J. R. D.; Dimeo, R. M. DAVE: A Comprehensive Software Suite for the Reduction, Visualization, and Analysis of Low Energy Neutron Spectroscopic Data. *Journal of research of the National Institute of Standards and Technology* **2009**, *114*, 341–358.

[46] Mamontov, E.; Herwig, K. W. A time-of-flight backscattering spectrometer at the Spallation Neutron Source, BASIS. *Review of Scientific Instruments* **2011**, *82*, 085109.

[47] Arnold, O. et al. Mantid—Data analysis and visualization package for neutron scattering and microSR experiments. *Nuclear Instruments and Methods in Physics Research Section A: Accelerators, Spectrometers, Detectors and Associated Equipment* **2014**, *764*, 156–166.

[48] Mamontov, E.; Smith, R. W.; Billings, J. J.; Ramirez-Cuesta, A. J. Simple analytical model for fitting QENS data from liquids. *Physica B: Condensed Matter* **2019**, *566*, 50–54.

[49] Mozur, E. M.; Trowbridge, J. C.; Maughan, A. E.; Gorman, M. J.; Brown, C. M.; Prisk, T. R.; Neilson, J. R. Dynamical Phase Transitions and Cation Orientation-Dependent Photoconductivity in $CH(NH_2)_2PbBr_3$. *ACS Materials Letters* **2019**, *1*, 260–264.

[50] Mozur, E. M.; Neilson, J. R. Cation Dynamics in Hybrid Halide Perovskites. *Annual Review of Materials Research* **2021**, *51*, 269–291.

[51] Sears, V. F. Neutron scattering lengths and cross sections. *Neutron News* **1992**, *3*, 26–37.

[52] Bée, M. *Quasielastic neutron scattering : principles and applications in solid state chemistry, biology, and materials science*; Adam Hilger: Bristol, England; Philadelphia, 1988; pp 194–203.

[53] Goldschmidt, V. Die Gesetze der Krystallochemie. *Naturwissenschaften* **1926**, *14*, 477–485.

[54] Shannon, R. Revised effective ionic radii and systematic studies of interatomic distances in halides and chalcogenides. *Acta Crystallographica Section A* **1976**, *32*, 751–767.

[55] Fu, Y.; Jiang, X.; Li, X.; Traore, B.; Spanopoulos, I.; Katan, C.; Even, J.; Kanatzidis, M. G.; Harel, E. Cation Engineering in Two-Dimensional Ruddlesden–Popper Lead Iodide Perovskites with Mixed Large A-Site Cations in the Cages. *Journal of the American Chemical Society* **2020**, *142*, 4008–4021.

[56] Cao, D. H.; Stoumpos, C. C.; Farha, O. K.; Hupp, J. T.; Kanatzidis, M. G. 2D Homologous Perovskites as Light-Absorbing Materials for Solar Cell Applications. *Journal of the American Chemical Society* **2015**, *137*, 7843–7850.

[57] Lee, M. M.; Teuscher, J.; Miyasaka, T.; Murakami, T. N.; Snaith, H. J. Efficient Hybrid Solar Cells Based on Meso-Superstructured Organometal Halide Perovskites. *Science* **2012**, *338*, 643.

[58] Tsai, H. et al. High-efficiency two-dimensional Ruddlesden–Popper perovskite solar cells. *Nature 536*, 312–316.

[59] Stoumpos, C. C.; Malliakas, C. D.; Kanatzidis, M. G. Semiconducting Tin and Lead Iodide Perovskites with Organic Cations: Phase Transitions, High Mobilities, and Near-Infrared Photoluminescent Properties. *Inorganic Chemistry 52*, 9019–9038.

[60] Johnston, M. B.; Herz, L. M. Hybrid Perovskites for Photovoltaics: Charge-Carrier Recombination, Diffusion, and Radiative Efficiencies. *Accounts of Chemical Research 49*, 146–154, Publisher: American Chemical Society.

[61] Mitzi, D. B.; Feild, C. A.; Harrison, W. T. A.; Guloy, A. M. Conducting tin halides with a layered organic-based perovskite structure. *Nature 369*, 467–469.

[62] Stoumpos, C. C.; Cao, D. H.; Clark, D. J.; Young, J.; Rondinelli, J. M.; Jang, J. I.; Hupp, J. T.; Kanatzidis, M. G. Ruddlesden–Popper Hybrid Lead Iodide Perovskite 2D Homologous Semiconductors. *Chemistry of Materials* **2016**, *28*, 2852–2867.

[63] Mao, L.; Kennard, R. M.; Traore, B.; Ke, W.; Katan, C.; Even, J.; Chabinyc, M. L.; Stoumpos, C. C.; Kanatzidis, M. G. Seven-Layered 2D Hybrid Lead Iodide Perovskites. *Chem* **2019**, *5*, 2593–2604.

[64] Stoumpos, C. C.; Soe, C. M. M.; Tsai, H.; Nie, W.; Blancon, J.-C.; Cao, D. H.; Liu, F.; Traoré, B.; Katan, C.; Even, J.; Mohite, A. D.; Kanatzidis, M. G. High Members of the 2D Ruddlesden-Popper Halide Perovskites: Synthesis, Optical Properties, and Solar Cells of $(CH_3(CH_2)_3NH_3)_2(CH_3NH_3)_4Pb_5I_{16}$. *Chem* **2017**, *2*, 427–440.

[65] Koegel, A. A.; Mozur, E. M.; Oswald, I. W. H.; Jalarvo, N. H.; Prisk, T. R.; Tyagi, M.; Neilson, J. R. Correlating Broadband Photoluminescence with Structural Dynamics in Layered Hybrid Halide Perovskites. *Journal of the American Chemical Society* **2022**, *144*, 1313–1322.

[66] Gong, X.; Voznyy, O.; Jain, A.; Liu, W.; Sabatini, R.; Piontkowski, Z.; Walters, G.; Bappi, G.; Nokhrin, S.; Bushuyev, O.; Yuan, M.; Comin, R.; McCamant, D.; Kelley, S. O.; Sargent, E. H. Electron–phonon interaction in efficient perovskite blue emitters. *Nature Materials* **2018**, *17*, 550–556.

[67] Dahlman, C. J.; Kennard, R. M.; Paluch, P.; Venkatesan, N. R.; Chabinyc, M. L.; Manjunatha Reddy, G. N. Dynamic Motion of Organic Spacer Cations in Ruddles-

den–Popper Lead Iodide Perovskites Probed by Solid-State NMR Spectroscopy. *Chemistry of Materials* **2021**, *33*, 642–656.

[68] Kagdada, H. L.; Gupta, S. K.; Sahoo, S.; Singh, D. K. Mobility driven thermoelectric and optical properties of two-dimensional halide-based hybrid perovskites: impact of organic cation rotation. *Physical Chemistry Chemical Physics 24*, 8867–8880.

[69] Willcott, M. R. MestRe Nova. *Journal of the American Chemical Society* **2009**, *131*, 13180–13180.

[70] Copley, J. R. D.; Cook, J. C. The Disk Chopper Spectrometer at NIST: a new instrument for quasielastic neutron scattering studies. *Chemical Physics* **2003**, *292*, 477–485.

[71] Miyata, K.; Meggiolaro, D.; Trinh, M. T.; Joshi, P.; Mosconi, E.; Jones, S.; De Angelis, F.; Zhu, X.-Y. Large polarons in lead halide perovskites. *Science Advances 3*, e1701217.

[72] Maehrlein, S. F.; Joshi, P. P.; Huber, L.; Wang, F.; Cherasse, M.; Liu, Y.; Juraschek, D. M.; Mosconi, E.; Meggiolaro, D.; Angelis, F. D.; Zhu, X.-Y. Decoding ultrafast polarization responses in lead halide perovskites by the two-dimensional optical Kerr effect. *Proceedings of the National Academy of Sciences* **2021**, *118*.

[73] Leguy, A. M. A.; Frost, J. M.; McMahon, A. P.; Sakai, V. G.; Kockelmann, W.; Law, C.; Li, X.; Foglia, F.; Walsh, A.; O'Regan, B. C.; Nelson, J.; Cabral, J. T.; Barnes, P. R. F.

The dynamics of methylammonium ions in hybrid organic–inorganic perovskite solar cells. *Nature Communications* **2015**, *6*, 7124.

[74] Deng, C.; Zhou, G.; Chen, D.; Zhao, J.; Wang, Y.; Liu, Q. Broadband Photoluminescence in 2D Organic–Inorganic Hybrid Perovskites: (C7H18N2)PbBr4 and (C9H22N2)PbBr4. *The Journal of Physical Chemistry Letters* **2020**, *11*, 2934–2940.

[75] Grote, C.; Berger, R. F. Strain Tuning of Tin–Halide and Lead–Halide Perovskites: A First-Principles Atomic and Electronic Structure Study. *The Journal of Physical Chemistry C 119*, 22832–22837, Publisher: American Chemical Society.

[76] Lee, J.-H.; Bristowe, N. C.; Lee, J. H.; Lee, S.-H.; Bristowe, P. D.; Cheetham, A. K.; Jang, H. M. Resolving the Physical Origin of Octahedral Tilting in Halide Perovskites. *Chemistry of Materials 28*, 4259–4266, Publisher: American Chemical Society.

[77] Prasanna, R.; Gold-Parker, A.; Leijtens, T.; Conings, B.; Babayigit, A.; Boyen, H.-G.; Toney, M. F.; McGehee, M. D. Band Gap Tuning via Lattice Contraction and Octahedral Tilting in Perovskite Materials for Photovoltaics. *Journal of the American Chemical Society* **2017**, *139*, 11117–11124.

[78] Jung, M.-H. White-Light Emission from the Structural Distortion Induced by Control of Halide Composition of Two-Dimensional Perovskites ($(C_6H_5CH_2NH_3)_2PbBr_{4-x}Cl_x$). *Inorganic Chemistry 58*, 6748–6757, Publisher: American Chemical Society.

[79] Mozur, E. M. ORGANIC-INORGANIC DIPOLAR AND QUADRUPOLAR COUPLING UNDERLIES THE STRUCTURE AND PROPERTIES OF HYBRID PEROVSKITES.

[80] Blancon, J.-C. et al. Extremely efficient internal exciton dissociation through edge states in layered 2D perovskites. *Science 355*, 1288–1292, Publisher: American Association for the Advancement of Science.

[81] Biswas, A.; Bakthavatsalam, R.; Shaikh, S. R.; Shinde, A.; Lohar, A.; Jena, S.; Gonnade, R. G.; Kundu, J. Efficient Broad-Band Emission from Contorted Purely Corner-Shared One Dimensional (1D) Organic Lead Halide Perovskite. *Chemistry of Materials 31*, 2253–2257, Publisher: American Chemical Society.

[82] Zhou, C.; Tian, Y.; Khabou, O.; Worku, M.; Zhou, Y.; Hurley, J.; Lin, H.; Ma, B. Manganese-Doped One-Dimensional Organic Lead Bromide Perovskites with Bright White Emissions. *ACS Applied Materials & Interfaces 9*, 40446–40451, Publisher: American Chemical Society.

[83] Wu, G.; Zhou, C.; Ming, W.; Han, D.; Chen, S.; Yang, D.; Besara, T.; Neu, J.; Siegrist, T.; Du, M.-H.; Ma, B.; Dong, A. A One-Dimensional Organic Lead Chloride Hybrid with Excitation-Dependent Broadband Emissions. *ACS Energy Letters 3*, 1443–1449, Publisher: American Chemical Society.

Appendix A

Supplemental Information for Correlating Broadband Photoluminescence with Structural Dynamics in Layered Hybrid Halide Perovskites

Preliminary Characterization

For the compounds synthesized in this study, PXRD data were modeled with space groups of *Pbca* for (nBA)$_2$PbBr$_4$, $P2_1/c$ for (ODA)PbBr$_4$, and $P2_1/c$ for (GABA)$_2$PbBr$_4$ using previously reported structures[1] with the Rietveld method implemented in TOPAS v6 (Bruker AXS). The room temperature photoluminescence spectroscopy reveals emission peaked near 415 nm (Figure 2), in agreement with a previous study.[1]

Thermal activation of motion

Activation energies vary by molecule and motion occurring within (nBA)$_2$PbBr$_4$, (ODA)PbBr$_4$, and (GABA)$_2$PbBr$_4$. The organic cation dynamics do not follow classically Arrhenius behavior as seen in Figure 3. The data presented as ln(τ) v. T^{-1} are not linear and there are multiple relaxation times observed at $T \geq$ 275 K for (nBA)$_2$PbBr$_4$ and $T \geq$ 275 K for (ODA)PbBr$_4$.

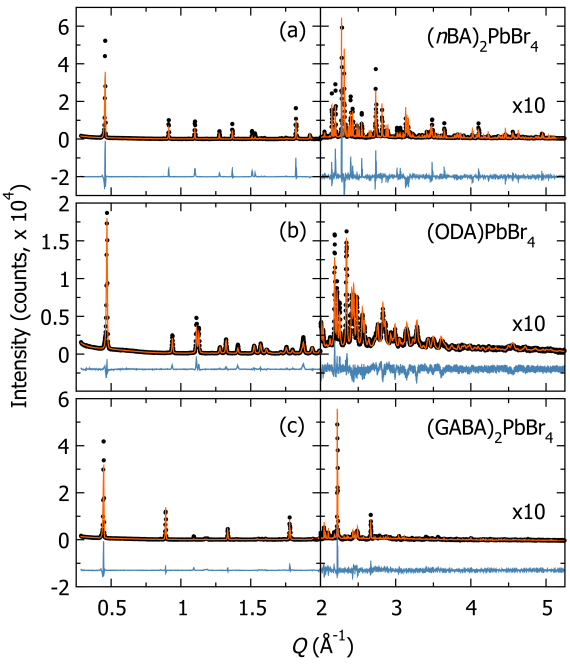

Figure 1: Powder X-ray diffraction of (a) $(n\text{BA})_2\text{PbBr}_4$, (b) $(\text{ODA})\text{PbBr}_4$, and (c) $(\text{GABA})_2\text{PbBr}_4$. Black circles, orange line, and blue line represent the data, Rietveld refinement, and difference curve, respectively.

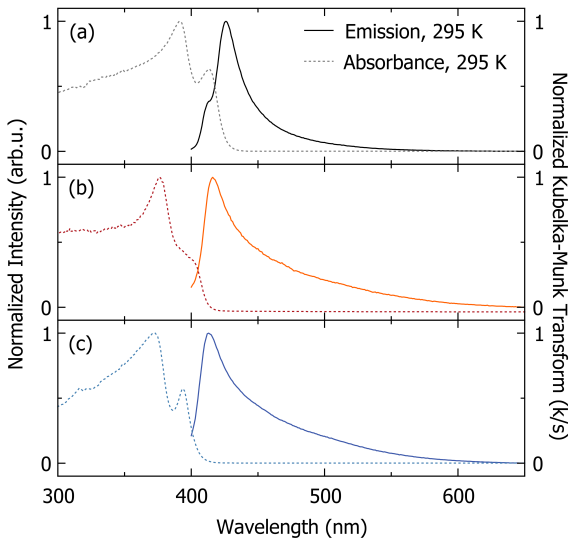

Figure 2: Ambient temperature (295 K) normalized photoluminescence intensity with excitation at 375 nm (solid lines, left axis) showing narrow emission centered at 415 nm and Kubelka-Munk transform (k/s) (dotted lines, right axis) of (a) $(n\text{BA})_2\text{PbBr}_4$ (black), (b) $(\text{ODA})\text{PbBr}_4$ (red), and (c) $(\text{GABA})_2\text{PbBr}_4$ (blue).

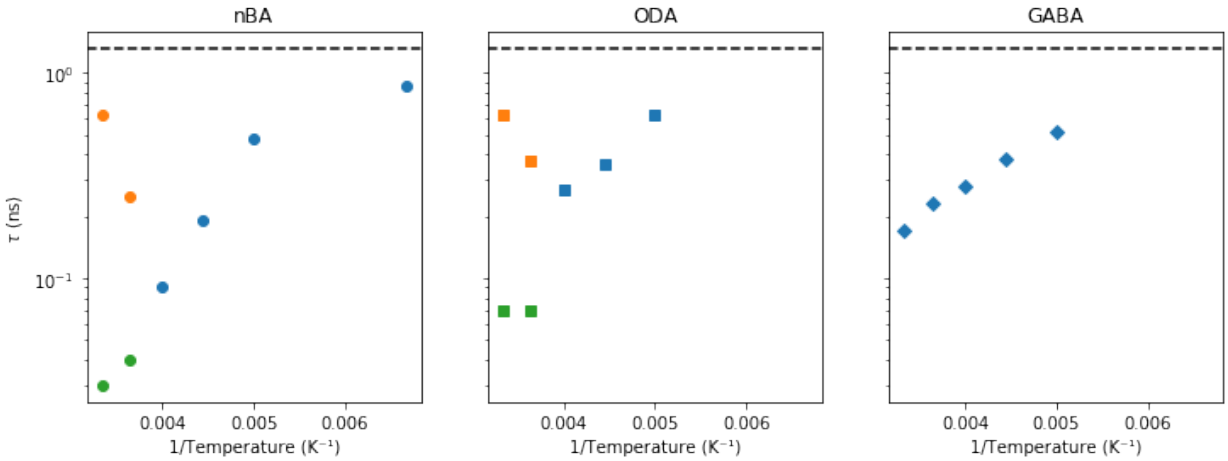

Figure 3: ln(τ) vs. T^{-1} (left) (nBA)$_2$PbBr$_4$, (middle) (ODA)PbBr$_4$, and (right) (GABA)$_2$PbBr$_4$ calculated from QENS data collected from 150 K to 300 K. Blue symbols indicate a singular Lorentzian. Orange and green symbols indicate two separate Lorentzian functions used to model the QENS data.

Quasi-elastic scattering

There is no QENS observed at liquid nitrogen temperatures (Figure 4). This lack of resolvable QENS is due to the speed of the organic cation motions occurring within the broad elastic line at low temperatures, making quasi-elastic interactions unobservable within the resolution of the instrument. At temperatures $<$ 200 K only the motions of nBA are observable and have a full width at half maximum (FWHM) of roughly 1.5 μeV (Figures 5 and 6).

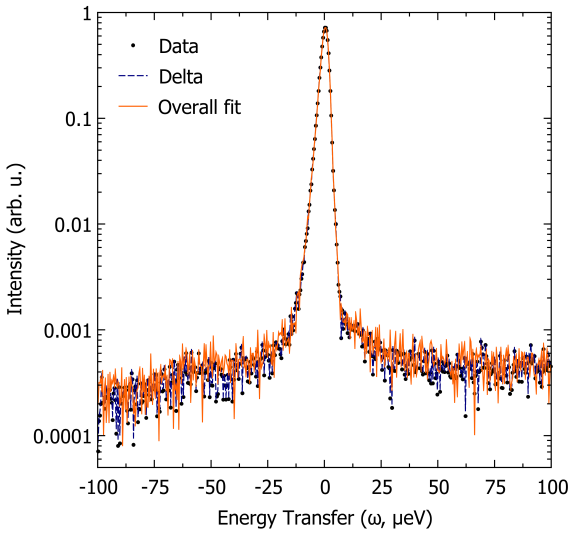

Figure 4: Representative QENS spectra of $(GABA)_2PbBr_4$ at $T = 77$ K for $Q = 1.1$ Å^{-1} collected at BASIS. The spectra are shown as black circles, with the overall fit shown as a solid red line. The data are modeled with a δ-function convolved with an instrument resolution function collected for each sample at $T = 20$ K to account for elastic scattering, shown here as a blue dashed line. There are no quasi-elastic interactions present.

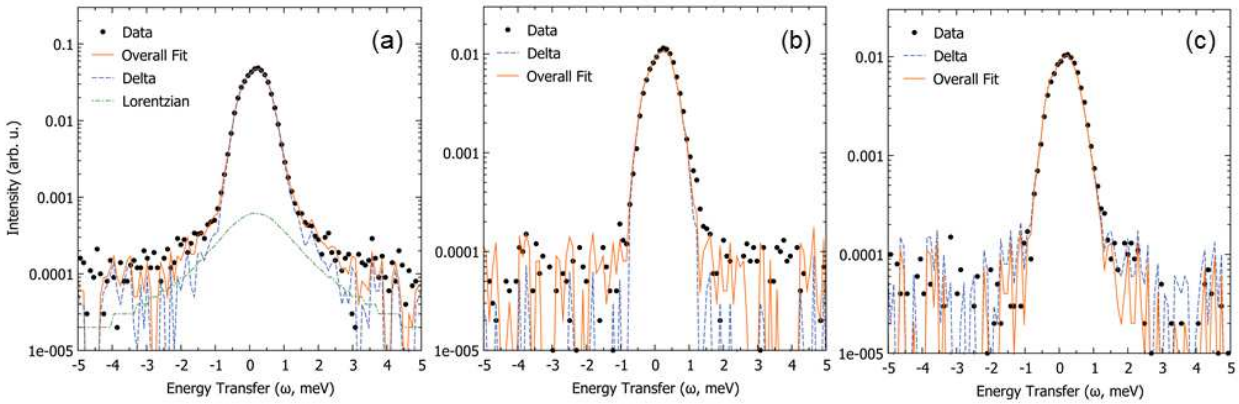

Figure 5: Quasi-elastic neutron scattering at 150 K for (a) $(n\text{BA})_2PbBr_4$ (b) $(ODA)PbBr_4$, and (c) $(GABA)_2PbBr_4$ collected at HFBS. The representative spectra are shown as black circles, with the overall fit shown as a solid red line. The data are modeled with a δ-function convolved with an instrument resolution function collected for each sample with a vanadium standard to account for elastic scattering, shown here as a blue dashed line. The broadening from quasi-elastic scattering is fit with a Lorentzian, shown as a green dash-dotted lines only in (a). Note the log scale on the y-axis.

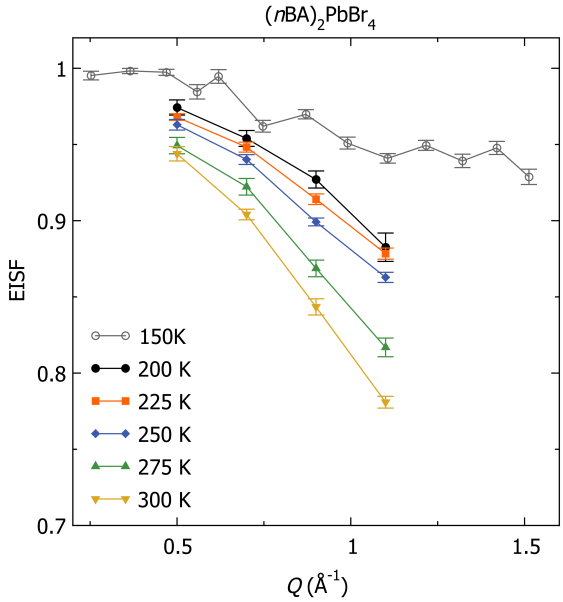

Figure 6: Elastic incoherent structure factor of $(n\text{BA})_2\text{PbBr}_4$ at 150 K to 300 K extracted from quasi-elastic neutron scattering data from HFBS (150 K) and BASIS (200 K to 300 K). Error bars represent one standard deviation.

Rotational mode analysis

Figures 8 and 9 are the molecules with either a total model (Figure 8) or C_3 model (Figure 9) applied to the data at temperatures 200 K to 300 K. Figure 8a shows the full model for (nBA)$_2$PbBr$_4$ that includes $C_2 \otimes C_3$ of the $-$NH$_3$ headgroup (a C_2 of the $-$CH$_2$ adjacent to the $-$NH$_3$ terminal group with a C_3 of the ammonium headgroup), a C$_3$ of the methyl group, and librations of the aliphatic hydrogens applied to the data at all temperatures, as depicted in Figure 7. The model describes the data at 300 K and does not describe the data for $T \leq$ 275 K. When the model is reduced to describe only the C_3 motions of the ammonium headgroup and methyl group, the model fits the data at 275 K (Figure 9). All other data has an EISF representative of a more static molecule than a C_3 model implies. Therefore, fractional motion was applied to fit data for $T <$ 275 K. The best fit parameters for fractional C_3 motion are tabulated in Table 2 and plotted in Figure 10.

Figure 8b shows the results from fitting the full dynamic model for ODA in (ODA)PbBr$_4$ that includes $C_2 \otimes C_3$ of the $-$CH$_2$NH$_3$ headgroup in conjunction with a C_2 of the$-$CH$_2$ adjacent to the $-$NH$_3$ terminal group and librations of the aliphatic hydrogens applied to the data at all temperatures depicted in Figure 7. This model only describes the data for $T \geq$ 275 K. However, when the model is changed to only describe the C_3 motion of the ammonium head groups, it is a good fit to data $T =$ 250 K, whereas the EISFs at $T \leq$ 225 K describe a more static molecule than the model. Therefore, fractional motion was applied to fit the low temperature data. The best fit parameters for fractional C_3 motion are tabulated in Table 2 and plotted in Figure 10.

Figure 8c shows the full model for $(GABA)_2PbBr_4$ that includes $C_2 \otimes C_3$ of the $-CH_2NH_3$ headgroup in conjunction with a C_2 of the $-CH_2$ adjacent to the $-NH_3$ terminal group and $-COOH$ group, and librations of the aliphatic hydrogens applied to the data at all temperatures depicted in Figure 7. This model does not describe any of the data. When the motion is reduced to a model describing only C_3 motions, the data at $T = 300$ K fits well; however, none of the other temperatures are described. Therefore, a fractional C_3 model was applied. The best fit parameters for fractional C_3 motion are tabulated in Table 2 and plotted in Figure 10.

Relaxation times of the principle hopping motions of the cations described above are listed in Table 8 and shown in Figure 11. Extrapolated relaxation times were calculated with a least squares polynomial fit in Python. The nBA cations have the shortest measured relaxation times at all temperatures except 77 K, where GABA has the shortest extrapolated relaxation time.

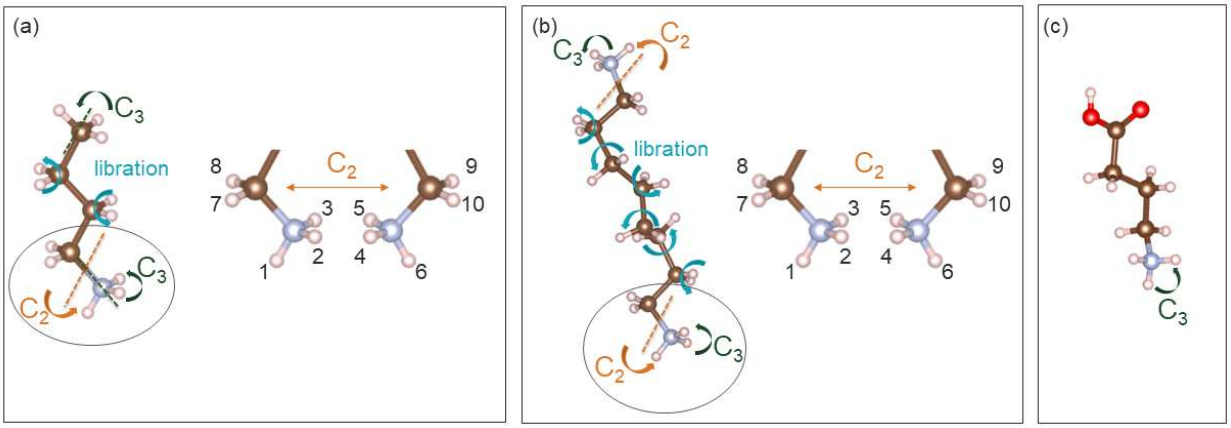

Figure 7: Visualization of rotational motions simulated in jump models in (a) $(n\text{BA})_2PbBr_4$, (b) $(ODA)PbBr_4$, and (c) $(GABA)_2PbBr_4$ at room temperature. Green arrows indicate C_3 rotations of the $-NH_3$ and CH_3 groups. Orange arrows indicate a C_2 rotation of the $-CH_2NH_3$ head group about a predetermined angle as indicated in the cartoon on the left.[5] Blue arrows indicate librations of the $-CH_2$ chain.

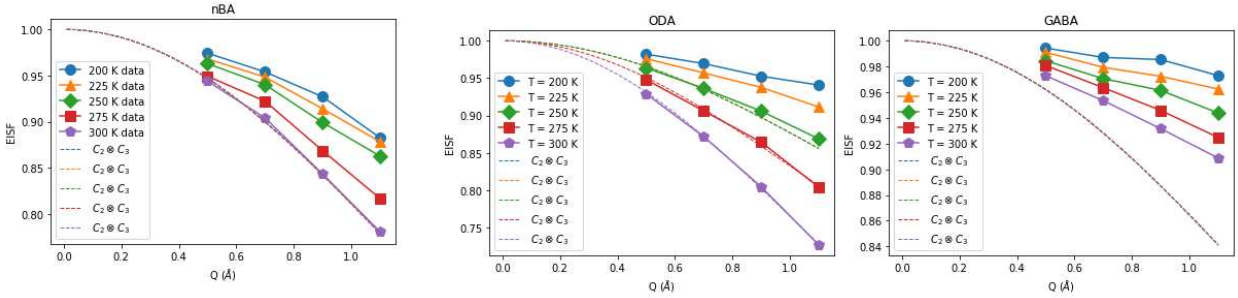

Figure 8: Elastic incoherent structure factor of (left) $(n\text{BA})_2\text{PbBr}_4$, (middle) $(\text{ODA})\text{PbBr}_4$, and (right) $(\text{GABA})_2\text{PbBr}_4$ at 200 K to 300 K extracted from QENS data at BASIS fit with a jump model labeled as $C_2 \otimes C_3$ that, depending on the molecule, includes: $C_2 \otimes C_3$ of the $-\text{CH}_2\text{NH}_3$ headgroup, C_3 of the ammonium and methyl groups, C_2 of the $-\text{CH}_2\text{CH}_3$ headgroup and $-\text{COOH}$, and librations of the CH_2 backbone, as described above. The full model does not describe all motions at all temperatures for the three molecules studied. The models for temperatures in (a) $T \leq 300$ K, (b) $T \leq 275$ K, and (c) $T \leq 300$ K are overlapping.

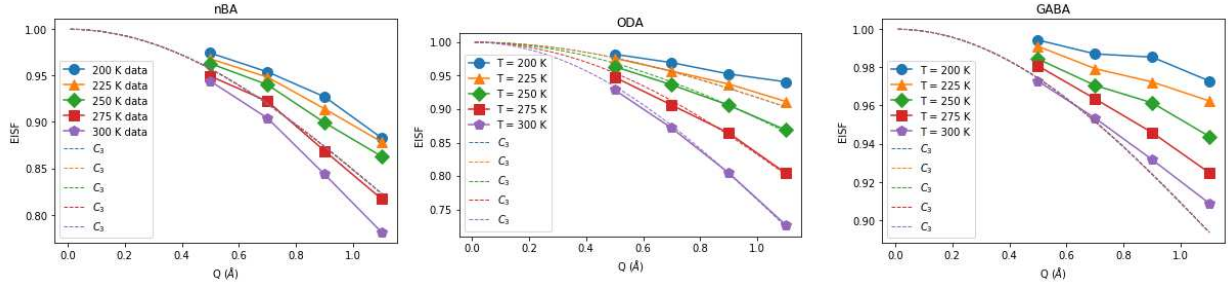

Figure 9: Elastic incoherent structure factor of (left) $(n\text{BA})_2\text{PbBr}_4$, (middle) $(\text{ODA})\text{PbBr}_4$, and (right) $(\text{GABA})_2\text{PbBr}_4$ at 200 K to 300 K extracted from QENS data at BASIS modeled by a jump model describing the C_3 rotations of the ammonium headgroup, as described in the narrative. This model does not describe all motions at all temperatures for the three molecules studied. The models for $T \leq 300$ K, (b) $T \leq 250$ K, and (c) $T \leq 300$ K are overlapping

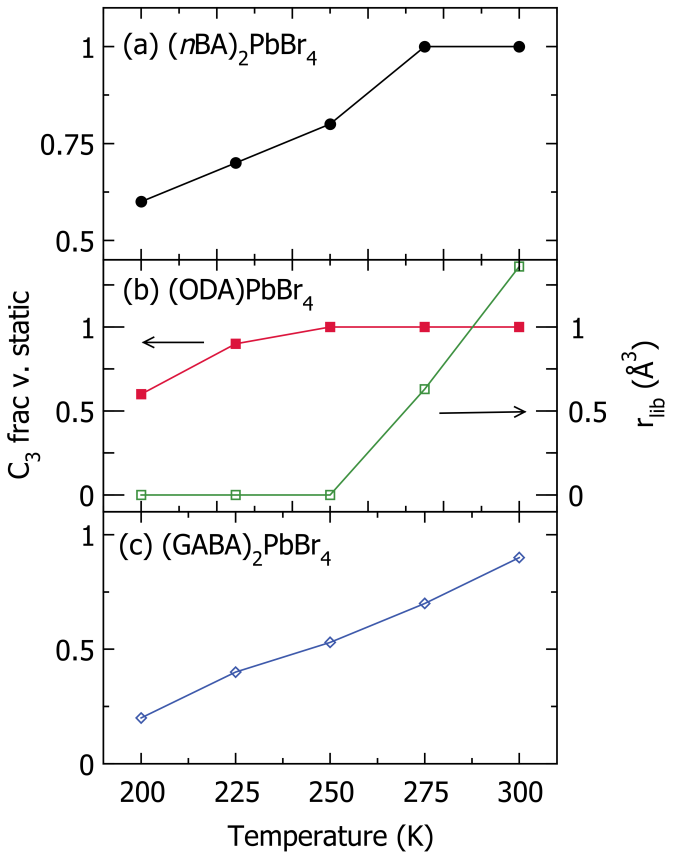

Figure 10: Fraction of C_3 motion of the organic cation in (a) $(n\text{BA})_2\text{PbBr}_4$ (black), (b) $(\text{ODA})\text{PbBr}_4$ (red), and (c) $(\text{GABA})_2\text{PbBr}_4$ (blue) at 200 K to 300 K extracted from QENS data at BASIS modeled by a jump model describing the C_3 rotations of the ammonium headgroup and methyl group, as described in the narrative. Values are listed in Table 2. (b, green) Libration radius of the of the $-\text{CH}_2-$ hydrogens in $(\text{ODA})\text{PbBr}_4$ at 200 K to 300 K extracted from QENS data at BASIS modeled by a jump model as described in the narrative. Libration radii are as follows: At T = 300 K the libration distance is 1.36 Å^{-1}, at T = 275 K the libration distance is 0.630 Å^{-1}.

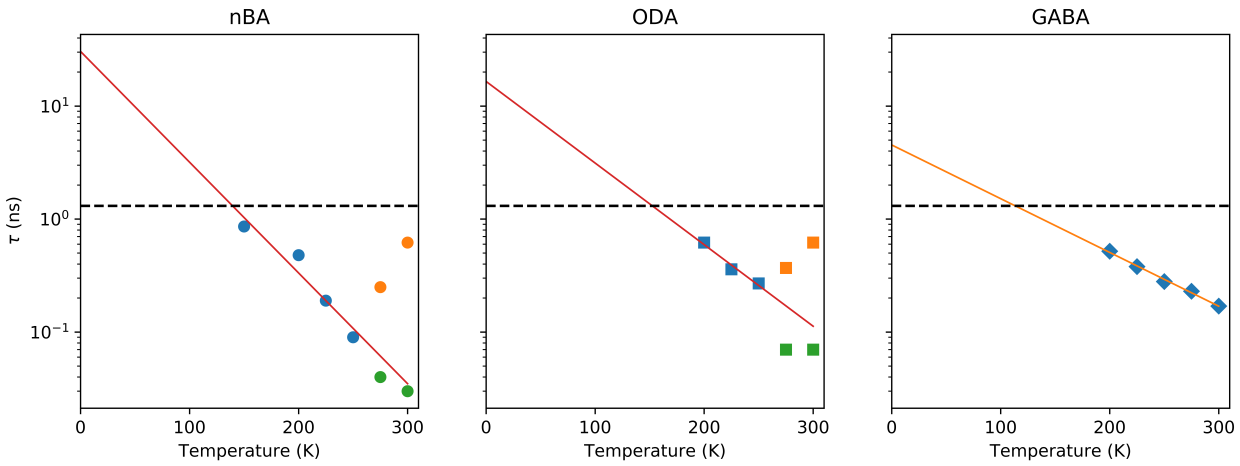

Figure 11: Extrapolated relaxation times for (left) $(n\text{BA})_2\text{PbBr}_4$, (middle) $(\text{ODA})\text{PbBr}_4$, and (right) $(\text{GABA})_2\text{PbBr}_4$. Extrapolations were done with a least squares polynomial fit in Python. Values determined from extrapolations are in Table 8. Dashed line indicates instrument resolution. Blue symbols indicate a singular Lorentzian. Orange and green symbols indicate two separate Lorentzian functions used to model the QENS data.

Table 1: Relaxation times of hydrogen motions (τ, ns) extracted from QENS spectra. Error bars represent one standard deviation.

	Relaxation times† (ns)		
Temp (K)	nBA	ODA	GABA
77	5.35*	4.59*	1.94*
150	0.86±0.1	1.36*	0.876*
200	0.48±0.02	0.62±0.009	0.52±0.05
225	0.19±0.004	0.36±0.009	0.38±0.02
250	0.09±0.002	0.27±0.004	0.28±0.01
275	0.25±0.07, 0.04±0.005	0.37±0.02, 0.07±0.003	0.23±0.005
300	0.62±0.27, 0.03±0.0008	0.62±0.07, 0.07±0.0007	0.17±0.005

† Calculated with the formula: $\text{HWHM}_{\text{Lorentzian}} = \hbar/\tau$

* Estimated extrapolated relaxation time values. Values were extrapolated assuming $\ln(\tau) = AT + B$, fitting A and B across the temperatures for which a single tau is recorded. (Figure 11).

Uncertainty calculated for nBA at 150 K used error propagation of one Q-group from DAVE.

Table 2: Best fit parameters for hydrogens undergoing fractional C_3 motion in $(n\text{BA})_2\text{PbBr}_4$, (ODA)$\text{PbBr}_4$, and $(\text{GABA})_2\text{PbBr}_4$. Errors were estimated from taking the square root of the diagonals of the covariance matrix.

C_3 Fraction			
Temperature (K)	nBA	ODA	GABA
200	0.60(2)	0.6000(6)	0.2000(3)
225	0.70(1)	0.9000(3)	0.4000(2)
250	0.80(1)	-	0.53000(4)
275	-	-	0.7000(8)
300	-	-	0.9000(7)

Table 3: A-site volumes (Å^3, calculated from the [NBr_8] polyhedra in VESTA as described in the narrative) determined from the 295 K crystal structures of $(n\text{BA})_2\text{PbBr}_4$, $(\text{ETA})_2\text{PbBr}_4$, $(\text{PEA})_2\text{PbBr}_4$, (MPenDA)$\text{PbBr}_4$, (ODA)$\text{PbBr}_4$, (BDA)$\text{PbBr}_4$, (AEA)$\text{PbBr}_4$, (HIS)$\text{PbBr}_4$, and $(\text{GABA})_2\text{PbBr}_4$.[1†]

Compound	Out-of-plane tilt angle (°)[1]	Volume (Å^3)	Observation of BBPL[1]
$(n\text{BA})_2\text{PbBr}_4$	2.8	84.6	No
$(\text{ETA})_2\text{PbBr}_4$	6.3	90.6	Yes, minimal
$(\text{PEA})_2\text{PbBr}_4$	10.4	84.2	Yes
(MPenDA)PbBr_4	17.9	78.6	Yes
(ODA)PbBr_4	19.0	79.2	Yes
(BDA)PbBr_4	20.7	80.2	Yes
(AEA)PbBr_4	22.4	61.1	Yes
(HIS)PbBr_4	22.8	59.2	Yes
$(\text{GABA})_2\text{PbBr}_4$	23.9	79.6	Yes

† Abbreviations used: nBA = n-butylammonium, ETA = ethanolammonium, PEA = phenethylammonium, MPenDA = 2-methyl-1,5-pentanediammonium, ODA = 1,8-diammoniooctammonium, BDA = butanediammonium, AEA = ammonioethylanilinium, HIS = histammonium, GABA = 4-aminobutyric acid.

Time-resolved photoluminescence of $(GABA)_2PbBr_4$

The time-resolved photoluminescence data vary between samples. The decay times were calculated from time-resolved photoluminescence data using $R(t) = B_1 \exp(-t/\tau_1) + B_2 \exp(-t/\tau_2)$ and are well described by two exponential decays. The emission behavior in $(GABA)_2PbBr_4$ (Figure 12, Table 4) is more complex; there is single-ensemble (as the spectrum does not change as a function of decay time) and multi-ensemble behavior between samples. In Figure 12 at wavelengths 500 nm, 550 nm, and 581 nm the behavior is primarily single-ensemble-like with spectrally sensitive time scales ($\approx$ 49$\pm$18 ns for τ_1 and $\approx$ 316$\pm$99.5 ns for τ_2). At wavelengths $\geq$ 610 nm, the decay time is much shorter ($\tau_1 \approx$ 10$\pm$4.5 ns and $\tau_2 \approx$ 201$\pm$82 ns) than in the other broad wavelengths probed indicative of multi-ensemble behavior. At 77 K where time-resolved data were collected for the broad spectrum the rotational motion of GABA is extrapolated to $\approx$ 1.5 ns, this is faster than the decay times across all wavelengths. This varies from Figure 8b in the main text; where the behavior is single-ensemble like across all wavelengths. As the rotational motions are not static when compared to decay times, one would expect time scales to be more spectrally independent as seen in the main text. The sample-dependent behavior is indicative of a surface or microstructure difference.[36] Performing spectroscopy on single crystals would eliminate the microstructure as a variable and provide a comprehensive study on the decay lifetimes of layered perovskites.

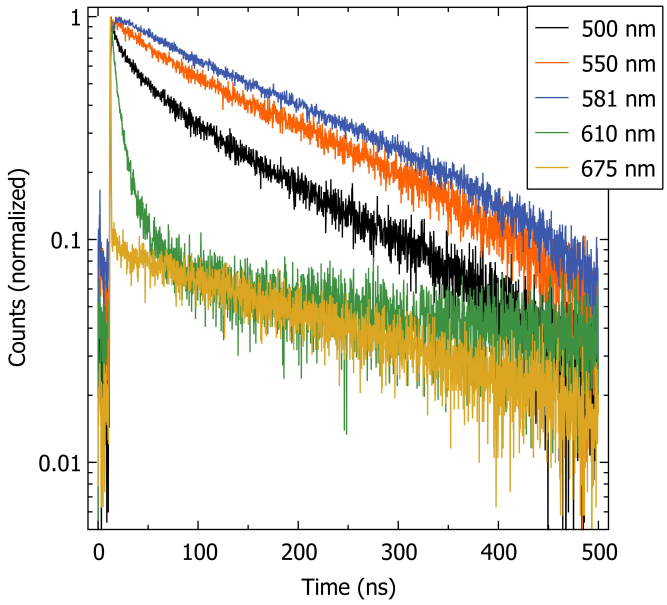

Figure 12: Time-resolved photoluminescence data for $(GABA)_2PbBr_4$. Time-resolved photoluminescence of $(GABA)_2PbBr_4$ at 500 nm (black), 550 nm (red), 581 nm (blue), 610 nm (green), and 675 nm (yellow) at 77 K. Data were normalized to the photoluminescence intensity at ≈ 158 ns. Decay times are listed in Table 4.

Table 4: Decay times of $(GABA)_2PbBr_4$ calculated from time-resolved photoluminescence with $R(t) = B_1 \exp(-t/\tau_1) + B_2 \exp(-t/\tau_2)$. The data are well described by a bi-exponential decay consisting of two components. τ_1 is shorter than τ_2 at all wavelengths measured. Error bars represent one standard deviation.

Decay times (ns)		
Wavelength (nm)	$\tau 1_{GABA}$	$\tau 2_{GABA}$
500	26±0.9	190±4
550	51±4	330±23
581	72±7	430±47
610	9.5±0.2	120±6
675	0.3±0.04	283±10

EISF jump models implemented in Python:

Preamble:

```
import numpy as np

from scipy.optimize import leastsq

from scipy import integrate
```

```
from scipy.optimize import curve_fit
from scipy.optimize import fsolve
from mpl_toolkits import mplot3d
```

```
def AY(th):
    #https://en.wikipedia.org/wiki/Rotation_formalisms_in_three_dimensions
    th = th *np.pi/180
    costh = np.cos(th)
    sinth = np.sin(th)
    M = np.array([[costh,0,sinth],[0,1,0],[-1.*sinth,0,costh]])
    return M

def AZ(ps):
    #https://en.wikipedia.org/wiki/Rotation_formalisms_in_three_dimensions
    ps = ps *np.pi/180
    cosps = np.cos(ps)
    sinps = np.sin(ps)
    M = np.array([[cosps,-1*sinps,0],[sinps,cosps,0],[0,0,1]])
    return M

def distance(a,b):
    return np.linalg.norm(a-b)
```

Hydrogen position generation and rotation:

```
j0=lambda Q,r: np.sin(Q*r)/(Q*r)

## Generate a structure, then move it with some
##  fitting parameters so everything is consistent:

# NH3 hydrogen positions (from an ideal GAMESS calculation, in angstroms)
H1 = np.array([1.0061 ,0.2389 ,1.1736   ])
H2 = np.array([-0.7100, 0.7518, 1.1736  ])
H3 = np.array([-0.2961, -0.9908, 1.1736 ])
```

```
H4 = np.array([0.2724, 0.9205, -1.0709  ])
H5 = np.array([-0.9333, -0.2243 ,-1.0709])
H6 = np.array([0.6609, -0.6961, -1.0709 ])
C1 = np.array([-0.0000, 0.0000, 0.8295  ])
N1 = np.array([-0.0000, 0.0000, -0.7032 ])
NH3 = np.zeros([5,3])
NH3[0]=H1
NH3[1]=H2
NH3[2]=H3
NH3[3]= H4  ## place holder
NH3[4]= H5  ## place holder

func = lambda x: np.dot(AZ(x),NH3.T).T[2,0]
Zangle = fsolve(func,16.8)[0]

NH3rot = np.dot(AZ(Zangle-90+180),NH3.T).T

NH3rot[3]= np.array([1.07/(2.09/np.sin(109.5*np.pi/180))*2.09, np.sin(109.5/2*np.pi/180)
    *1.07, 0.8295- np.cos(np.arcsin(1.07/(2.09/np.sin(109.5*np.pi/180))))*2.09  ])
NH3rot[4]= np.array([1.07/(2.09/np.sin(109.5*np.pi/180))*2.09, -1*np.sin(109.5/2*np.pi/180)
    *1.07, 0.8295- np.cos(np.arcsin(1.07/(2.09/np.sin(109.5*np.pi/180))))*2.09 ])

def positions(Yangle,Xoffset):
    ## Generate the shifted H positions based upon fitting parameters:
    NH3rot2 = np.dot(AY(Yangle),NH3rot.T).T
    NH3final = NH3rot2 - np.array([Xoffset,0,0])
    ## Generate second set (positions 4-6) via C2 rotation:
    NH3_C2 = np.dot(AZ(180),NH3final.T).T
    return NH3final,NH3_C2

def distances(Yangle,Xoffset,dlib):
    NH3final,NH3_C2=positions(Yangle,Xoffset)
    ## generate jump distances for EISF calculations:
```

```
    #Seung-Hun Lee OA+ C2xC3 from SI doi: 10.1063/1.5131667
    # See Table S.X.
    r0 = distance(NH3final[0],NH3final[1]) ## R1,2
    r1 = distance(NH3final[0],NH3_C2[0])   ## R1,4
    r2 = distance(NH3final[1],NH3_C2[1])   ## R2,5
    r3 = distance(NH3final[2],NH3_C2[2])   ## R3,6
    r4 = distance(NH3final[0],NH3_C2[1])   ## R1,5
    r5 = distance(NH3final[0],NH3_C2[2])   ## R1,6
    r6 = distance(NH3final[1],NH3_C2[2])   ## R2,6
    d1 = distance(NH3final[4],NH3_C2[4])   ## R7,9
    d2 = distance(NH3final[3],NH3_C2[3])   ## R8,10
    rs = [r0,r1,r2,r3,r4,r5,r6,d1,d2,dlib]
    return rs
```

Hydrogen position generation and rotation and visualization:

```
## visualize the H positions of the -CH2NH3 headgroup:


NH3final,NH3_C2=positions(fitparams[0],fitparams[1])


fig = plt.figure(figsize = (11, 7))
ax = plt.axes(projection ="3d")
ax.set_aspect('auto')
ax.set_xlim3d([-2.5,2.5])
ax.set_ylim3d([-2.5,2.5])
ax.set_zlim3d([-2.5,2.5])
# ax.set_box_aspect((1, 1, 1))
ax.view_init(15+180, 15+90)
# ax.view_init(0, 90)
ax.set_xlabel('x')
ax.set_ylabel('y')
ax.set_zlabel('z')
# Creating plot
```

```
ax.scatter3D(NH3final[:,0],NH3final[:,1],NH3final[:,2], color = "green",s=200)
ax.scatter3D(NH3_C2[:,0],NH3_C2[:,1],NH3_C2[:,2], color = "blue",s=200)

# # ## change i and j to highlight two different H's
i=3
j=4
## 3 and 4 highlight the -CH2 hydrogens
ax.scatter3D(NH3final[i,0],NH3final[i,1],NH3final[i,2], color = "black",s=400)
ax.scatter3D(NH3final[j,0],NH3final[j,1],NH3final[j,2], color = "red",s=400)
```

(nBA)2PbBr4 hydrogen position generation and rotation:

```
## then calculate EISFs based upon those structures:

def calcEISF(Q,*params):
    ## this is the full model by Lee et al.
    Yangle = params[0]
    Xoffset = params[1]
    dlib=params[2]
    r0,r1,r2,r3,r4,r5,r6,d1,d2,dlib = distances(Yangle,Xoffset,dlib)
    #Seung-Hun Lee OA+ from SI doi: 10.1063/1.5131667:
    # C2xC3, just describes the CH2NH3 headgroup.
    A_A_C2xC3 = 1/18*(3+6*j0(Q,r0)+j0(Q,r1)+j0(Q,r2)+j0(Q,r3)+2*j0(Q,r4)+2*j0(Q,r5)+2*j0(Q,
    r6))
    # C2XE for CH2 adjacent to NH3 terminal group.
    A_A_C2xE = 1/4*(2 + j0(Q,d1) + j0(Q,d2))
    ## Libration for CH2 groups:
    A_A_C2lib = 1/8 * (4+4*j0(Q,dlib))
    ## Methyl rotation:
    A_A_C3 = 1/9 * (3+6*j0(Q,r0))
    A_total = (3*A_A_C2xC3 + 2*A_A_C2xE + 4*A_A_C2lib + 3*A_A_C3)/12 ## specific to nBA
    return A_total
```

```
def calcEISF_C3lib(Q,dlib):
    ## this is just C3 motion of the -CH3 and -NH3 ends with libration
    r0 = distance(NH3rot[0],NH3rot[1])
    A_A_C3 = 1/9 * (3+6*j0(Q,r0))
    ## Libration for 6 CH2 groups:
    A_A_C2lib = 1/12 * (6+6*j0(Q,dlib))
    A_total = (6*A_A_C3 + 6*A_A_C2lib)/12 ## specific to nBA
    return A_total

def calcEISF_C3(Q):
    ## this is just C3 motion of the -CH3 and -NH3 ends
    r0 = distance(NH3rot[0],NH3rot[1])
    A_A_C3 = 1/9 * (3+6*j0(Q,r0))
    static = np.ones(np.shape(Q))
    A_total = (6*A_A_C3 + 6*static)/12
    return A_total

def calcEISF_C3_variablefrac(Q,frac):
    ## this is just C3 motion of the -CH3 and -NH3 ends with variable fraction of motion
    r0 = distance(NH3rot[0],NH3rot[1])
    A_A_C3 = 1/9 * (3+6*j0(Q,r0))
    static = np.ones(np.shape(Q))
    A_total = (6*frac*A_A_C3 + 6*(2-frac)*static)/12
    return A_total



def calcEISFs(Q,*params):
    ### this is the full motion of the Lee model, but we return all of the different
    contributions
    Yangle = params[0]
    Xoffset = params[1]
    dlib=params[2]
```

```
    r0,r1,r2,r3,r4,r5,r6,d1,d2,dlib = distances(Yangle,Xoffset,dlib)
    #Seung-Hun Lee OA+ from SI doi: 10.1063/1.5131667:
    # C2xC3, just describes the CH2NH3 headgroup.
    A_A_C2xC3 = 1/18*(3+6*j0(Q,r0)+j0(Q,r1)+j0(Q,r2)+j0(Q,r3)+2*j0(Q,r4)+2*j0(Q,r5)+2*j0(Q,
    r6))
    # C2XE for CH2 adjacent to NH3 terminal group.
    A_A_C2xE = 1/4*(2 + j0(Q,d1) + j0(Q,d2))
    ## Libration for CH2 groups:
    A_A_C2lib = 1/8 * (4+4*j0(Q,dlib))
    ## Methyl rotation:
    A_A_C3 = 1/9 * (3+6*j0(Q,r0))
    A_total = (3*A_A_C2xC3 + 2*A_A_C2xE + 4*A_A_C2lib + 3*A_A_C3)/12 ## specific to nBA
    return A_total,3/12*A_A_C2xC3,2/12*A_A_C2xE ,4/12*A_A_C2lib,3/12*A_A_C3
```

(ODA)PbBr4 hydrogen position generation and rotation:

```
def calcEISF_ODA(Q,*params):
    ## this is the full model by Lee et al.
    Yangle = params[0]
    Xoffset = params[1]
    dlib=params[2]
    r0,r1,r2,r3,r4,r5,r6,d1,d2,dlib = distances(Yangle,Xoffset,dlib)
    #Seung-Hun Lee OA+ from SI doi: 10.1063/1.5131667:
    # C2xC3, just describes the CH2NH3 headgroup.
    A_A_C2xC3 = 1/18*(3+6*j0(Q,r0)+j0(Q,r1)+j0(Q,r2)+j0(Q,r3)+2*j0(Q,r4)+2*j0(Q,r5)+2*j0(Q,
    r6))
    # C2XE for CH2 adjacent to NH3 terminal group.
    A_A_C2xE = 1/4*(2 + j0(Q,d1) + j0(Q,d2))
    ## Libration for CH2 groups:
    A_A_C2lib = 1/24 * (12+12*j0(Q,dlib))
    A_total = (6*A_A_C2xC3 + 4*A_A_C2xE + 12*A_A_C2lib )/22 ## specific to ODA
    return A_total
```

(GABA)2PbBr4 hydrogen position generation and rotation:

```
def calcEISF_GABA(Q,*params):
    ## this is the full model by Lee et al.
    Yangle = params[0]
    Xoffset = params[1]
    dlib=params[2]
    djump=params[3]
    r0,r1,r2,r3,r4,r5,r6,d1,d2,dlib = distances(Yangle,Xoffset,dlib)
    #Seung-Hun Lee OA+ from SI doi: 10.1063/1.5131667:
    # C2xC3, just describes the CH2NH3 headgroup.
    A_A_C2xC3 = 1/18*(3+6*j0(Q,r0)+j0(Q,r1)+j0(Q,r2)+j0(Q,r3)+2*j0(Q,r4)+2*j0(Q,r5)+2*j0(Q,
    r6))
    # C2XE for CH2 adjacent to NH3 terminal group.
    A_A_C2xE = 1/4*(2 + j0(Q,d1) + j0(Q,d2))
    ## Libration for CH2 groups:
    A_A_C2lib = 1/24 * (12+12*j0(Q,dlib))
    A_COOH = 1/2*(1+j0(Q,djump))  ### for C2 jumps in a circle
    A_total = (3*A_A_C2xC3 + 2*A_A_C2xE + 4*A_A_C2lib + A_COOH )/10 ## specific to GABA
    return A_total
```

Appendix B

Supplemental Information for Influence of Inorganic Layer Thickness on Methylammonium Dynamics in Hybrid Perovskite Derivatives

NMR Analysis

Rietveld refinements (Figure 13) confirm the phase purity of ($d-n$BA)$_2$(MA)Pb$_2$I$_7$ and ($d-n$BA)$_2$(MA)$_2$Pb$_3$I$_{10}$. Table 5 lists the refined lattice parameters with the addition of the deuterated n-butylammonium cation. All other parameters are as in the reference structure.[62] Nuclear magnetic resonance (NMR) spectroscopy confirms the full deuteration of the d-nBA backbone owing to the absence of a triplet at 0.8 ppm, a sextet at 1.2 ppm, and quintet at 1.4 ppm in the crystal (Figure 14).[6] The broad singlet at 7.521 ppm is indicative of the amine groups in $CD_3(CD_2)_3NH_3^+$ and $CH_3NH_3^+$. The singlet at 3.288 ppm is indicative of water. The complex multiplets highlighted in the inset of Figure 14 are representative of hexanes from rinsing the final powder product (quintet centered at 2.465 ppm) and the methyl group on methylammonium (quartet centered at 2.3415 ppm).[6] The supernatant of the crystal growth solution consists of HI, H_2O, acetic acid, hexanes, Pb^{2+}, and I^-. The supernatant does not contain any paramagnetic species or nuclei and would not cause any $J_{couplings}$. The broad singlet at 7.578 ppm in Figure 15

(inset (a)) is indicative of the amine groups on both $CD_3(CD_2)_3NH_3^+$ and $CH_3NH_3^+$. The satellite peak at 7.486 ppm is from hydroiodic acid hydrogens. The singlet at 5.870 ppm is from acetic acid hydrogens. The singlet at 4.737 ppm is water hydrogen. Inset (b) in Figure 15 shows the quintet and quartet associated with hexane and methylammonium methyl hydrogens. The singlet at 1.853 ppm is the d-DMSO residual peak with satellite peaks at 2.012 ppm and 1.690 ppm.

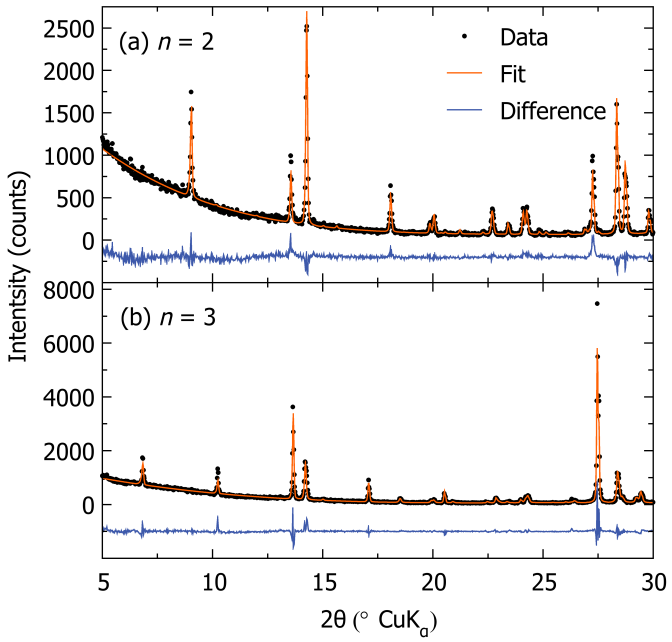

Figure 13: Powder X-ray diffraction data for (a) $(d{-}n\text{BA})_2\text{MAPb}_2\text{I}_7$ and (b) $(d{-}n\text{BA})_2\text{MA}_2\text{Pb}_3\text{I}_{10}$ samples. Data are shown as black dots with the overall Rietveld refinements as red lines and difference curve as blue lines.

Table 5: Structural Parameters and Refinement Statistics for $(d{-}n\text{BA})_2(\text{MA})\text{Pb}_2\text{I}_7$, $n = 2$ and $(d{-}n\text{BA})_2(\text{MA})_2\text{Pb}_3\text{I}_{10}$, $n = 3$ from Powder X-ray Diffracton at $T = 295$ K.

	$(d{-}n\text{BA})_2(\text{MA})\text{Pb}_2\text{I}_7$	$(d{-}n\text{BA})_2(\text{MA})_2\text{Pb}_3\text{I}_{10}$
a (Å)	8.9572(1)	8.929(2)
b (Å)	39.3138(3)	52.0163(2)
c (Å)	8.8744(0)	8.8771(2)
Volume (Å^3)	3125.4(6)	4122.9(1)
Space Group	*Cc2m*, #40, setting 5	*C2ce*, #41, setting 4

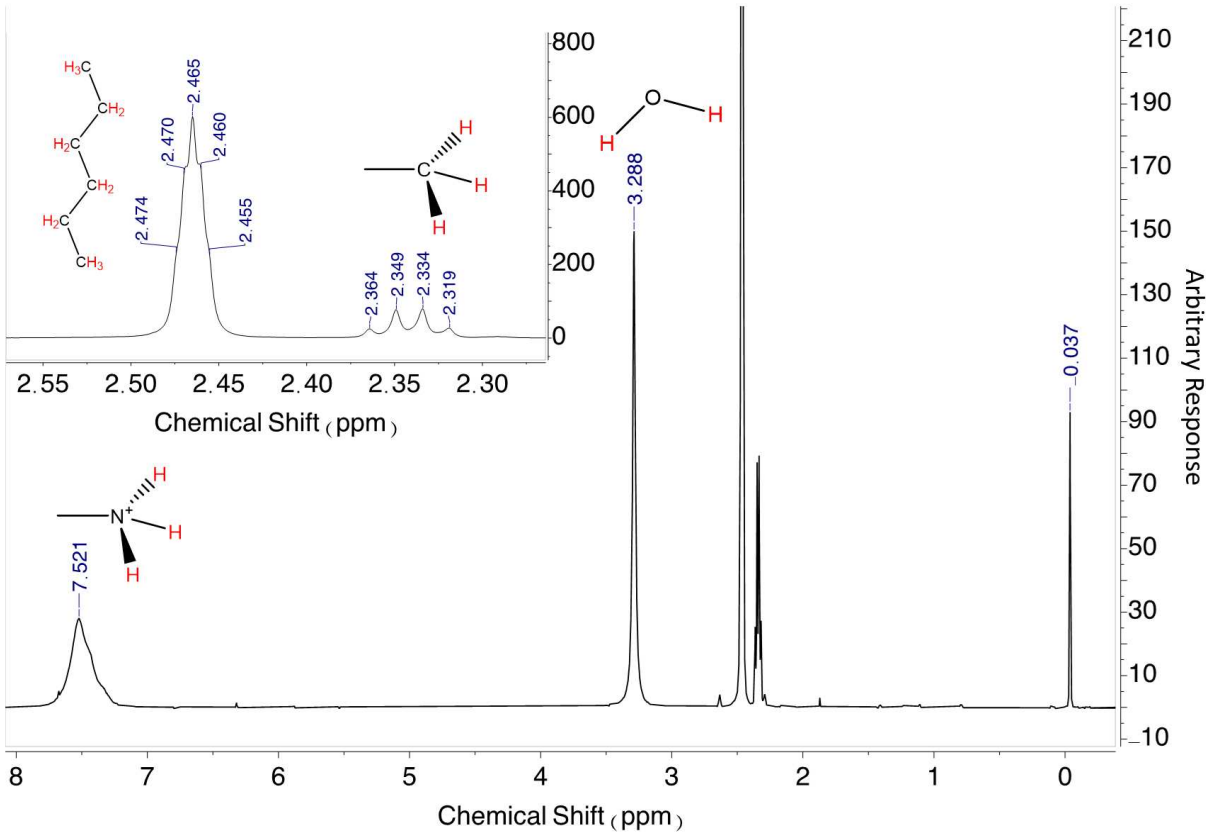

Figure 14: Nuclear magnetic resonance spectroscopy of $(d{-}n\text{BA})_2(\text{MA})\text{Pb}_2\text{I}_7$ crystals dissolved in d-DMSO. The absence of strong peaks at 0.8 ppm, 1.2 ppm, and 1.4 ppm indicate the $\text{CD}_3(\text{CD}_2)_3\text{NH}_3{}^+$ carbon backbone is fully deuterated.[6] Singlets at 7.521 ppm and 3.288 ppm are ammonium and water hydrogens, respectively. (Inset) the multiplet peaks centered at 2.465 ppm and 2.3415 ppm are hexanes and methylammonium methyl hydrogens, respectively.

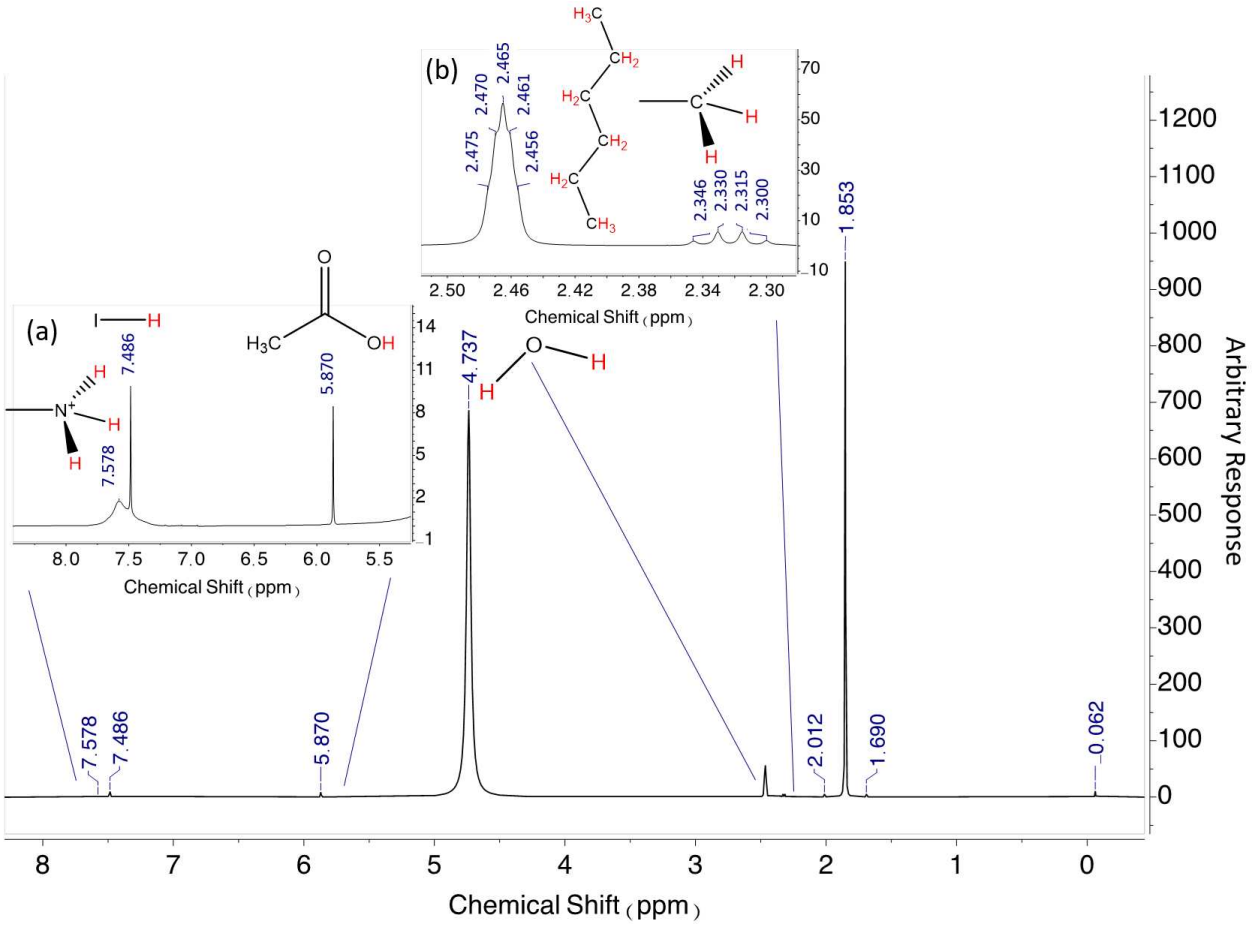

Figure 15: Nuclear magnetic resonance spectroscopy of the supernatant from the $(d{-}n\text{BA})_2(\text{MA})\text{Pb}_2\text{I}_7$ precipitation reaction revealing the presence of HI, H_2O, acetic acid, hexanes, Pb^{2+}, and I^- in d-DMSO. Inset (a) is indicative of the ammonium groups on both $CD_3(CD_2)_3NH_3^+$ and $CH_3NH_3^+$. The satellite peak at 7.486 ppm is hydroiodic acid hydrogen. The singlet at 5.870 ppm is acetic acid hydrogen. Inset (b) quintet and quartet associated with hexane and methylammonium methyl hydrogens. Singlets at 4.737 ppm and 1.853 ppm are water and d-DMSO hydrogen, respectively.

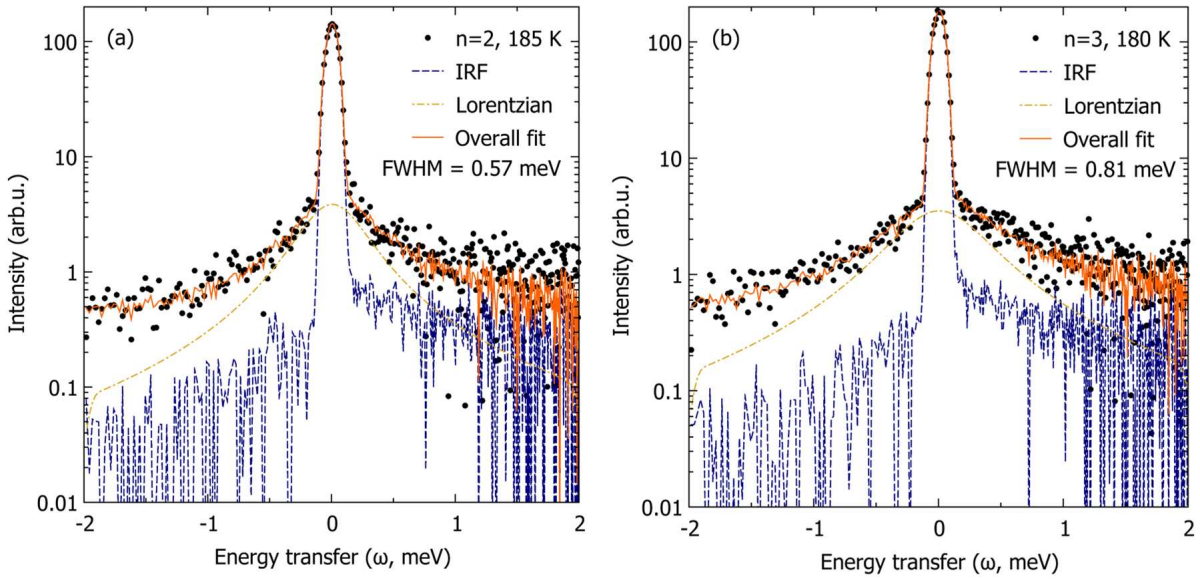

Figure 16: Representative QENS spectra of (a) $(d{-}n\text{BA})_2(\text{MA})\text{Pb}_2\text{I}_7$ at 185 K and (b) $(d{-}n\text{BA})_2(\text{MA})_2\text{Pb}_3\text{I}_{10}$ at 180 K. The spectra are shown as black circles, with the overall fit shown as a solid red line. The data are modeled with a delta function convolved with an instrument resolution function collected for each sample at $T = 4$ K to account for elastic scattering, shown here as a blue dashed line. The broadening from quasi-elastic scattering fit is with a Lorentzian, shown as yellow dash-dotted line. The FWHM of the Lorentzian for (a) $(d{-}n\text{BA})_2(\text{MA})\text{Pb}_2\text{I}_7$ at $T = 185$ K is 0.57 $\pm$ 0.03 meV. This is smaller than the FWHM at $T = 180$ K in $(d{-}n\text{BA})_2(\text{MA})_2\text{Pb}_3\text{I}_{10}$ (b, 0.81 $\pm$ 0.03 meV), which supports the shorter residence times in the higher n-member shown in Figure 3.2 in the main text. Uncertainties represent one standard deviation.

Jump model analysis of ($d-n$BA)$_2$(MA)Pb$_2$I$_7$ and ($d-n$BA)$_2$(MA)$_2$Pb$_3$I$_{10}$

The organic cation motions described in the narrative are represented in Figure 17. In modeling the EISFs obtained from the quasi-elastic neutron scattering experiments, we tested different combinations of the following jump models for methylammonium for each compound and each temperature:

- Full $C_3 \otimes C_4$ motion, where the methylammonium rotates 120° about the C-N bond axis, combined with a 90° rotation about its centroid. These two distinct rotations are illustrated in Figure 17(a).

- Fractional $C_3 \otimes C_4$ motion. In this model, the above rotations are included in a weighted average with a fully static methylammonium (i.e., only a fraction of the molecules rotate).

- Fractional C_3 motion. In this model, we exclusively consider the rotation of methylammonium about the C-N bond axis. Here, we model the motion in a weighted average with a fully static methylammonium (i.e., only a fraction of the molecules rotate).

and the following jump models for d-nBA:

- Full $C_2 \otimes C_3$ motion describing the $-$CD$_2$NH$_3$ headgroup, such that a 120° rotation (C_3) of the $-$NH$_3$ hydrogens about the C-N bond axis is combined with a 180° rotation of the full molecule about an arbitrarily defined C_2 axis as illustrated in Figure 17(b). In this model, we refine the positional offset of the C_2 axis as well as the angle

that the molecule makes with this axis. Given that the only hydrogens from d-nBA belong to the ammonium group, this simple and well-constrained model provides large degree of molecular motion, as previously used.[5]

- Fractional $C_2 \otimes C_3$ motion; the model described above was combined in a weighted average with a fully static d-nBA.

- Fractional C_3 motion of a 120° rotation (C_3) of the $-NH_3$ hydrogens about the C-N bond axis. This was combined in a weighted average with a fully static d-nBA.

- Static d-nBA. This was included with a dynamic methylammonium molecule, as the EISF is not strictly sensitive to the contributions from hydrogen from different molecules.

The scripts used to generate these jump models are included below. In this section, we discuss several of the most promising models that were eventually ruled out. The main text provides a description of the best fit models.

A full, $C_3 \otimes C_4$ rotational contribution from the MA cation combined with a full $C_2 \otimes C_3$ motion of the d-nBA cation does not represent the data accurately as shown in Figure 18. At all temperatures in both compounds studied (n = 2, 3), this model has a quasi-elastic contribution that is too large for the data. When a model that applies a fractional $C_2 \otimes C_3$ of the d-nBA $-CD_2NH_3$ headgroup in conjunction with a $C_3 \otimes C_4$ tumbling of the methylammonium (Figure 19) is fit to the EISF, it still does not describe the data and produces unphysical values for the C_2 axis offset and angle; therefore, the highest temperature data is fit with a full contribution of the $CH_3NH_3^+$ $C_3 \otimes C_4$ tumbling to account

for the steep drop-off in the EISF at low Q and a fractional C_3 contribution from the d-nBA ammonium headgroup for both n-members as discussed in the narrative (Figure 3.3).

For $T <$ 300 K the full $CH_3NH_3^+$ and fractional d-nBA model is has too much quasi-elastic contribution to represent the data (Figure 20) in both n-members; therefore, it stands to reason that one of the motions is no longer present. As the d-nBA contribution is already fractional, eliminating this motion fits temperatures 300 K $> T >$ 140 K, where the d-nBA ammonium headgroup is nominally static and there is a fractional contribution from the $CH_3NH_3^+$ $C_3 \otimes C_4$ tumbling (Figure 3.3). The difference between the 240 K/185 K in $(d-n\text{BA})_2(\text{MA})\text{Pb}_2\text{I}_7$ and 210 K/180 K in $(d-n\text{BA})_2(\text{MA})_2\text{Pb}_3\text{I}_{10}$ is therefore described by distinct fractional contributions of $CH_3NH_3^+$ $C_3 \otimes C_4$ motions to the EISF; these best fit parameters are plotted in Figure 22 and tabulated in Table 6.

When the temperature is further reduced $T \leq$ 140 K, the C_4 rotation of MA is frozen out and only the C_3 rotations of the $CH_3NH_3^+$ are contributing fractionally as a function of decreasing temperature in both compounds as plotted in Figure 22 and tabulated in Table 7. An alternative hypothesis is that only C_3 rotations of methylammonium are contributing to these dynamics at either high or low temperatures. This model is disproved as seen in Figure 21, as this alternative hypothesis does not describe the data at temperatures below 300 K. As the $C_3 \otimes C_4$ motion model is a better fit at $T =$ 300 K, the C_3 hypothesis is further discredited as a representative model.

Residence times of the principle hopping modes were calculated from the half-width-at-half-maximum from the Lorentzian function with the formula: HWHM $= \hbar/\tau$ and depicted in Figure 3.2 and listed in Table 8. The residence times increase as a function of decreas-

ing temperature with the exception of the temperatures where C_4 motion is freezing out ($T = 185$ K for $(d{-}n\text{BA})_2(\text{MA})\text{Pb}_2\text{I}_7$ and 180K for $(d{-}n\text{BA})_2(\text{MA})_2\text{Pb}_3\text{I}_{10}$) where they are shortened significantly as seen in the 3D materials.[29]

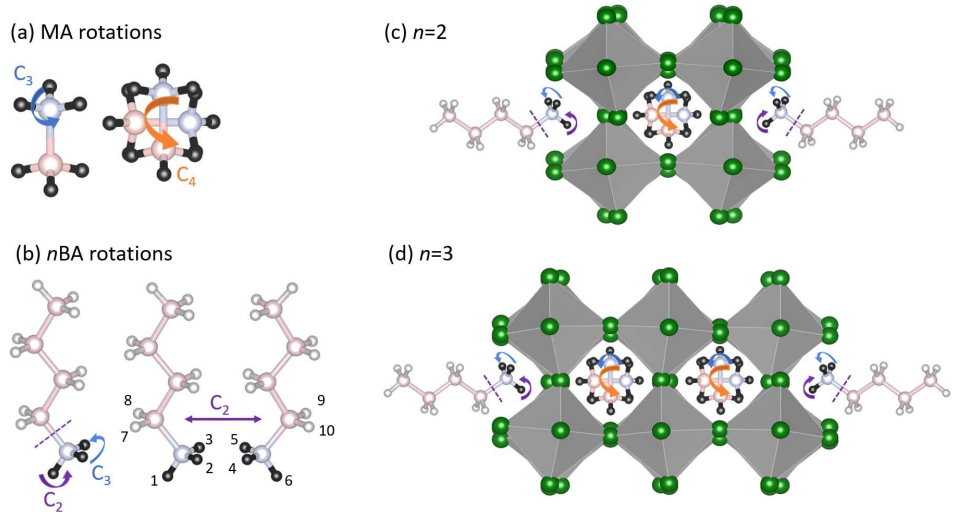

Figure 17: Organic cation rotations modeled in this paper as described in the narrative. (a) the $C_3 \otimes C_4$ tumbling of the methylammonium in the cuboctahedral void, where the C_4 is described by orange arrows and C_3 is described by blue arrows. (b) $C_2 \otimes C_3$ rotation of the d-nBA $-\text{CD}_2\text{NH}_3$ headgroup in the organic layer, where the C_2 is described by purple arrows and the C_3 is described by blue arrows. (c) the organic cation motions in $(d{-}n\text{BA})_2(\text{MA})\text{Pb}_2\text{I}_7$, n =2 and (d) the organic cation motions in $(d{-}n\text{BA})_2(\text{MA})_2\text{Pb}_3\text{I}_{10}$, n =3. Observable hydrogens are colored in black. Pale pink = C, pale blue = N, gray = D.

Table 6: Best fit parameters for hydrogens undergoing $C_3 \otimes C_4$ motion in $(d{-}n\text{BA})_2(\text{MA})\text{Pb}_2\text{I}_7$, n =2 and $(d{-}n\text{BA})_2(\text{MA})_2\text{Pb}_3\text{I}_{10}$, n =3. Errors were estimated from taking the square root of the diagonals of the covariance matrix.

$C_3 \otimes C_4$ Fraction			
Temperature (K)	$n = 2$	Temperature (K)	$n = 3$
300	1.0(1)	300	0.96(1)
240	0.77(1)	210	0.57(1)
185	0.63(4)	180	0.47(1)

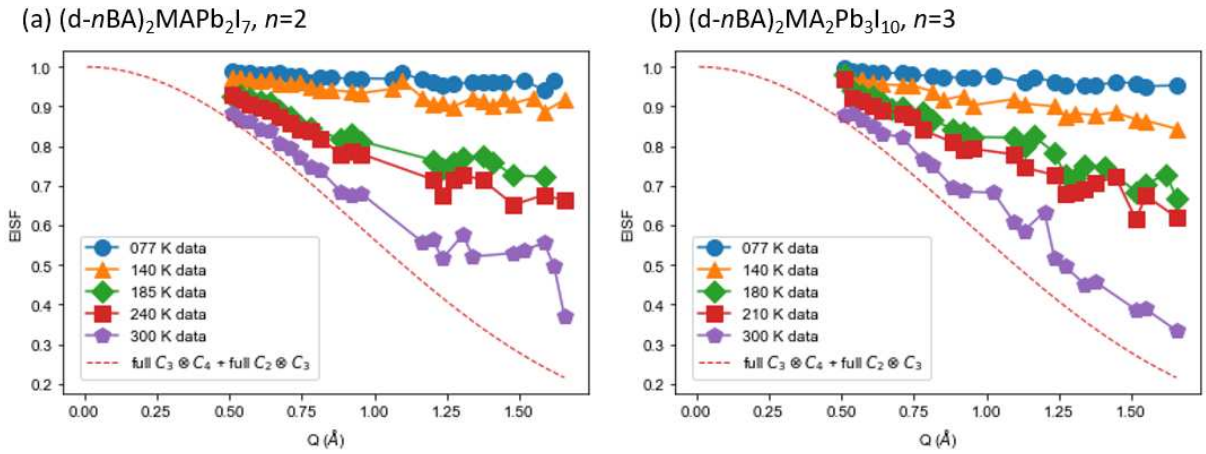

Figure 18: Elastic incoherent structure factors of (a) $(d{-}n\text{BA})_2(\text{MA})\text{Pb}_2\text{I}_7$ and (b) $(d{-}n\text{BA})_2(\text{MA})_2\text{Pb}_3\text{I}_{10}$ from 77 K to 300 K extracted from QENS data at DCS, NIST. Data are modeled by a jump model describing the full $C_3 \otimes C_4$ tumbling of the methylammonium in the cuboctahedral void and full $C_2 \otimes C_3$ rotation of the ammonium $-\text{CD}_2\text{NH}_3$ headgroup (dashed red line). This model does not describe the data at any temperature as it is more dynamic than the data.

Table 7: Best fit parameters for hydrogens undergoing C_3 motion in $(d{-}n\text{BA})_2(\text{MA})\text{Pb}_2\text{I}_7$, n =2 and $(d{-}n\text{BA})_2(\text{MA})_2\text{Pb}_3\text{I}_{10}$, n =3. Errors were estimated from taking the square root of the diagonals of the covariance matrix.

C_3 Fraction			
Temperature (K)	$n = 2$	Temperature (K)	$n = 3$
140	0.36(1)	140	0.37(1)
77	0.17(9)	77	0.13(4)

Table 8: Relaxation times (τ, ps) extracted from QENS spectra of $(d{-}n\text{BA})_2(\text{MA})\text{Pb}_2\text{I}_7$, n =2 and $(d{-}n\text{BA})_2(\text{MA})_2\text{Pb}_3\text{I}_{10}$, n =3. Error bars represent one standard deviation.

Temp (K)	$n = 2$ residence times (ps)	Temp (K)	$n = 3$ residence times (ps)
300	2.6±0.1	300	2.2±0.1
240	3.1±0.1	210	2.7±0.1
185*	2.3±0.1*	180*	1.6±0.07*
140	3.7±0.4	140	2.5±0.2
77	8.5±2	77	4.4±0.8

† Calculated with the HWHM in 9 with the formula: $\text{HWHM}_{\text{Lorentzian}} = \hbar/\tau$
* indicates change in residence time corresponding to phase transition
Uncertainty calculated with error propagation of one Q-group from DAVE.

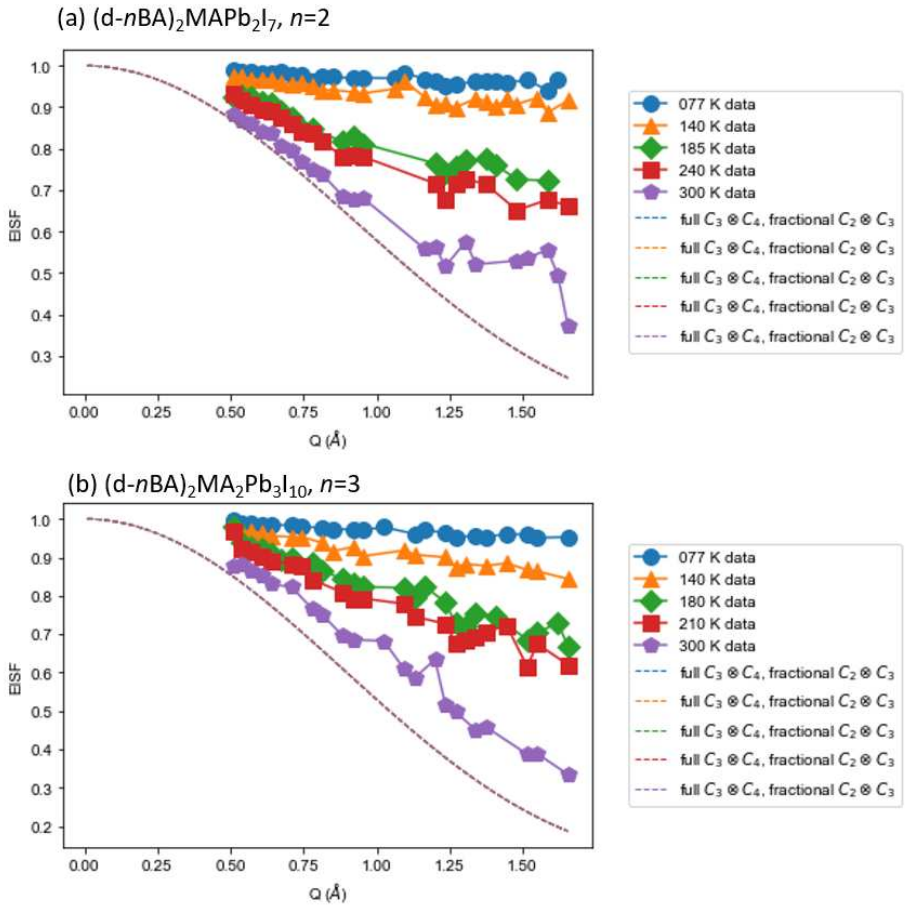

Figure 19: Elastic incoherent structure factors of (a) $(d{-}n\text{BA})_2(\text{MA})\text{Pb}_2\text{I}_7$ and (b) $(d{-}n\text{BA})_2(\text{MA})_2\text{Pb}_3\text{I}_{10}$ from 77 K to 300 K extracted from QENS data at DCS, NIST. Data are modeled by a jump model describing the full $C_3{\otimes}C_4$ tumbling of the methylammonium in the cuboctahedral void and a fractional $C_2{\otimes}C_3$ rotation of the d-nBA ammonium $-\text{CD}_2\text{NH}_3$ headgroup (dashed lines). This model does not describe the data at any temperature. Dashed lines for models describing data at $T \leq 300$ K are overlapping.

Table 9: Half-width half-maximum (HWHM, meV) extracted from QENS spectra of $(d{-}n\text{BA})_2(\text{MA})\text{Pb}_2\text{I}_7$, n =2 and $(d{-}n\text{BA})_2(\text{MA})_2\text{Pb}_3\text{I}_{10}$, n =3. Error bars represent one standard deviation.

Temp (K)	$n = 2$ HWHM (meV)	Temp (K)	$n = 3$ HWHM (meV)
300	0.25±0.01	300	0.29±0.01
240	0.21±0.01	210	0.25±0.01
185*	0.28±0.02	180*	0.40±0.02
140	0.18±0.02	140	0.27±0.02
77	0.07±0.03	77	0.15±0.03

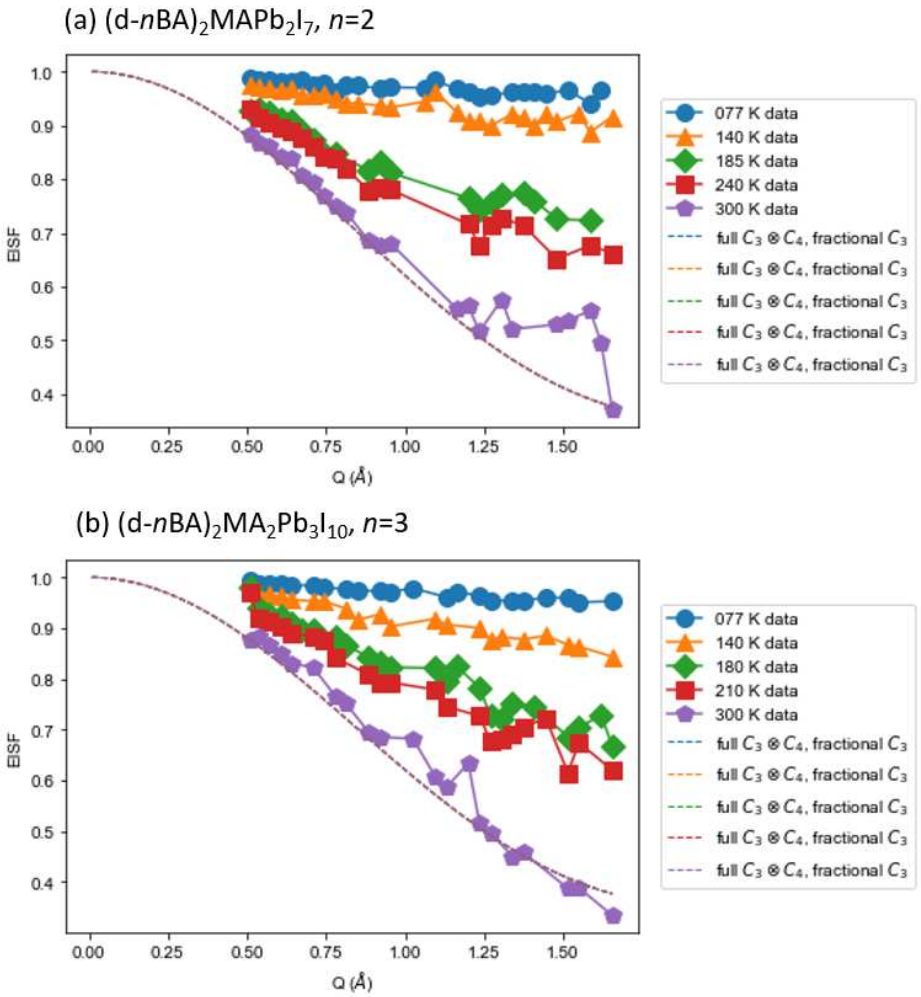

Figure 20: Elastic incoherent structure factors of (a) $(d{-}n\text{BA})_2(\text{MA})\text{Pb}_2\text{I}_7$ and (b) $(d{-}n\text{BA})_2(\text{MA})_2\text{Pb}_3\text{I}_{10}$ from 77 K to 300 K extracted from QENS data at DCS, NIST. Data are modeled by a jump model describing the full $C_3 \otimes C_4$ tumbling of the methylammonium in the cuboctahedral void and a fractional C_3 rotation of the d-nBA ammonium $-\text{NH}_3$ headgroup (dashed lines). This model does not describe the data at $T < 300$ K. Dashed lines for models describing data at $T \leq 300$ K are overlapping.

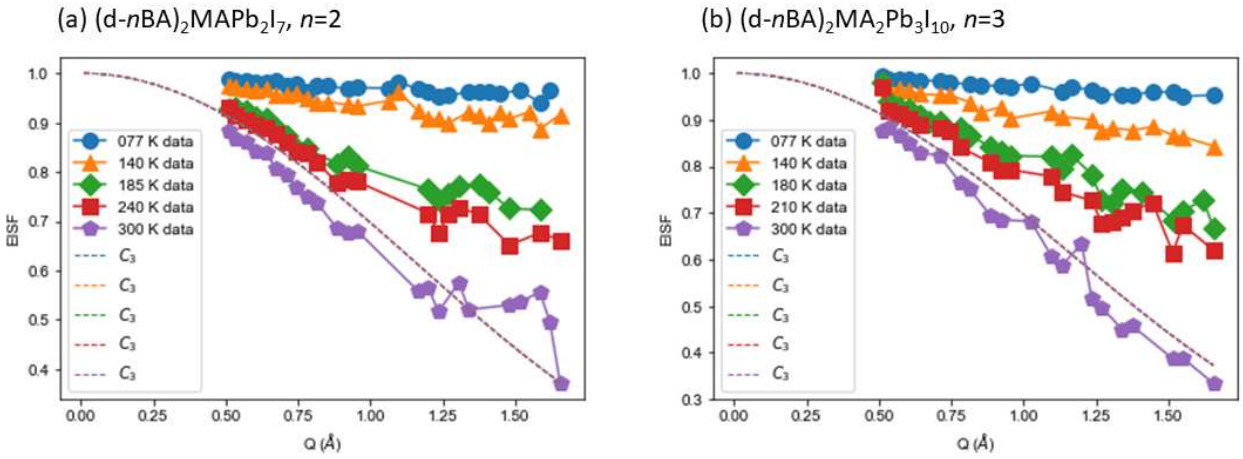

Figure 21: Elastic incoherent structure factors of (a) $(d{-}n\text{BA})_2(\text{MA})\text{Pb}_2\text{I}_7$ and (b) $(d{-}n\text{BA})_2(\text{MA})_2\text{Pb}_3\text{I}_{10}$ from 77 K to 300 K extracted from QENS data at DCS, NIST. Data are modeled by a jump model describing only the C_3 rotation of the methylammonium in the cuboctahedral void (dashed lines). This model does not describe the data at $T < 300$ K. Dashed lines for models describing data at $T < 300$ K are overlapping.

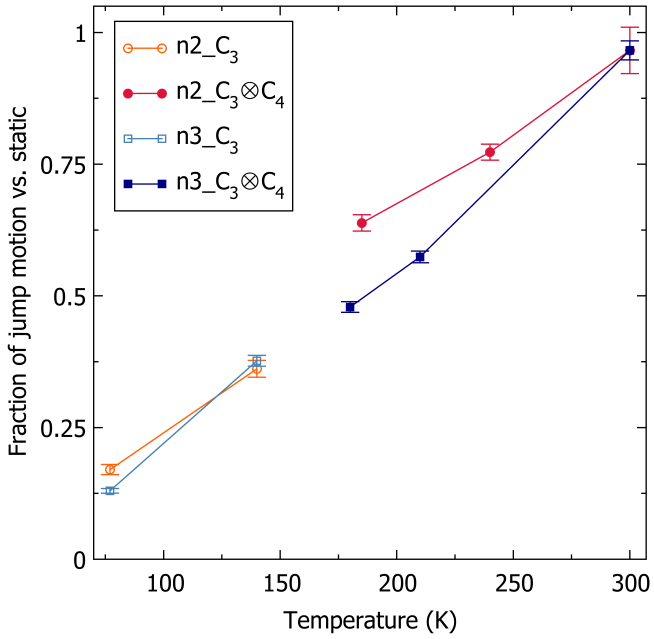

Figure 22: Fraction of C_3 and $C_3 \otimes C_4$ motion of the methylammonium organic cations in $(d{-}n\text{BA})_2(\text{MA})\text{Pb}_2\text{I}_7$ ($n = 2$, red circles) and $(d{-}n\text{BA})_2(\text{MA})_2\text{Pb}_3\text{I}_{10}$ ($n = 3$, blue squares) at 77 K to 300 K extracted from QENS data at DCS, NIST. The fractional motion is described as a linear combination of some fraction of the molecules experiencing the $C_3 \otimes C_4$ rotations at $T > 180$ K or C_3 rotations at $T \leq 140$ K and the other fraction are modeled as static; the fractional contribution is a fitted parameter. Jump models describe the C_3 rotations (hollow symbols) of the ammonium headgroup and methyl group of $CH_3NH_3^+$ and the $C_3 \otimes C_4$ rotation (solid symbols) of $CH_3NH_3^+$, as described in the narrative. Values are listed in Table 6 and Table 7. Error bars represent one standard deviation.

EISF jump models implemented in Python:

Models were fit and evaluated using the `curve_fit` routine implemented in `scipy.optimize` library and visualized using `matplotlib`.

Preamble:

```
import numpy as np
from scipy import integrate
from scipy.optimize import curve_fit
from scipy.optimize import fsolve
import matplotlib
```

Helper Functions:

```
def matrixrotate(ph,th,ps):
    #https://en.wikipedia.org/wiki/Rotation_formalisms_in_three_dimensions
    costh = np.cos(th)
    sinth = np.sin(th)
    cosph = np.cos(ph)
    sinph = np.sin(ph)
    cosps = np.cos(ps)
    sinps = np.sin(ps)
    M = np.array([[costh*cosps, -1.0*cosph*sinps + sinph*sinth*cosps, sinph*sinps+cosph*
    sinth*cosps],
                  [costh*sinps, cosph*cosps + sinph*sinth*sinps, -1.0*sinph*cosps + cosph*
    sinth*sinps],
                  [-1.0*sinth, sinph*costh,  cosph*costh]])
    return M


def AX(ph):
    ph = ph*np.pi/180
```

```
    cosph = np.cos(ph)
    sinph = np.sin(ph)
    M = np.array([[1,0,0],[0,cosph,-1.*sinph],[0,sinph,cosph]])
    return M

def AY(th):
    th = th *np.pi/180
    costh = np.cos(th)
    sinth = np.sin(th)
    M = np.array([[costh,0,sinth],[0,1,0],[-1.*sinth,0,costh]])
    return M

def AZ(ps):
    ps = ps *np.pi/180
    cosps = np.cos(ps)
    sinps = np.sin(ps)
    M = np.array([[cosps,-1*sinps,0],[sinps,cosps,0],[0,0,1]])
    return M

def XpRgen(X, a,b,c):
    # rotate a single molecule by a, b, and c angles.
    # the default angles are:
    # uniform(0, 2*np.pi), which provides a random number between 0 and 2pi
    M = matrixrotate(a,b,c)
    return np.dot(M, X.T).T

def distance(a,b):
    return np.linalg.norm(a-b)
```

Methylammonium structure generation and rotation:

```
## Generate a structure, then move and rotate it:
## adapted from DOI: 10.1039/C5CP05348J
```

```
# MA hydrogen positions
mC1=np.array([0,0,1.4937190])
mN1=np.array([0,0,-1.4937190])

mC1 = np.array([-0.0000, 0.0000, 0.8295  ])
mN1 = np.array([-0.0000, 0.0000, -0.7032 ])
mH1 = np.array([1.0061 ,0.2389 ,1.1736   ])
mH2 = np.array([-0.7100, 0.7518, 1.1736  ])
mH3 = np.array([-0.2961, -0.9908, 1.1736 ])
mH4 = np.array([0.2724, 0.9205, -1.0709  ])
mH5 = np.array([-0.9333, -0.2243 ,-1.0709])
mH6 = np.array([0.6609, -0.6961, -1.0709 ])

# Make eclispsed, and center about rotation:
mC1 = (mC1-mN1)/2
mN1 = -1*mC1
mH1 = np.array([mH1[0],mH1[1],(mH1[2]-mH4[2])/2])
mH2 = np.array([mH2[0],mH2[1],(mH2[2]-mH4[2])/2])
mH3 = np.array([mH3[0],mH3[1],(mH3[2]-mH4[2])/2])
mH4 = np.array([mH1[0],mH1[1],-1*mH1[2]])
mH5 = np.array([mH2[0],mH2[1],-1*mH2[2]])
mH6 = np.array([mH3[0],mH3[1],-1*mH3[2]])
MA = np.zeros([8,3])
MA[0] = mC1
MA[1] = mN1
MA[2] = mH1
MA[3] = mH2
MA[4] = mH3
MA[5] = mH4
MA[6] = mH5
MA[7] = mH6
```

```
## Rotate so on primary axes to make next steps easier:
MA=XpRgen(MA,0,0,16.638744652*np.pi/180+np.pi/2)
MA=np.dot(AX(180),MA.T).T


### C3xC4:
## compute jump distances according to:
## http://www.rsc.org/suppdata/c5/cp/c5cp05348j/c5cp05348j1.pdf
## (adapted from DOI: 10.1039/C5CP05348J )
mr1 = distance(MA[2],np.dot(AZ(120),MA[2].T).T)
mr2 = distance(MA[2],np.dot(AX(90),MA[2].T).T)
mr3 = distance(MA[2],np.dot(AY(120),(np.dot(AX(90),MA[2].T).T).T).T)
mr4 = distance(MA[2],MA[6])
mr5 = distance(MA[2],MA[5])
mr6 = distance(MA[2],np.dot(AX(90),MA.T).T[5])
mr7 = distance(MA[2],np.dot(AY(-120),(np.dot(AX(90),MA[2].T).T).T).T)
mr8 = distance(MA[2],MA[7])
mr9 = distance(MA[2],np.dot(AX(90),MA.T).T[7])
mr10= distance(MA[4],np.dot(AX(90),MA.T).T[4])
mdiameter = distance(MA[2],np.dot(AZ(180),MA[2].T).T)
rMA= mdiameter/2
mr = np.array([mr1,mr2,mr3,mr4,mr5,mr6,mr7,mr8,mr9,mr10])
```

n-butylammonium structure generation and rotation:

```
## Generate a structure, starting from CH3NH3+


# NH3 hydrogen positions (in Angstroms)
H1 = np.array([1.0061 ,0.2389 ,1.1736   ])
H2 = np.array([-0.7100, 0.7518, 1.1736  ])
H3 = np.array([-0.2961, -0.9908, 1.1736 ])
H4 = np.array([0.2724, 0.9205, -1.0709  ])
H5 = np.array([-0.9333, -0.2243 ,-1.0709])
H6 = np.array([0.6609, -0.6961, -1.0709 ])
```

```
C1 = np.array([-0.0000, 0.0000, 0.8295  ])
N1 = np.array([-0.0000, 0.0000, -0.7032 ])
NH3 = np.zeros([5,3])
NH3[0]=H1
NH3[1]=H2
NH3[2]=H3
NH3[3]= H4  ## place holder ; not sensitive to this position
NH3[4]= H5  ## place holder ; not sensitive to this position

# rotate so aligned with primary axis:
func = lambda x: np.dot(AZ(x),NH3.T).T[2,0]
Zangle = fsolve(func,16.8)[0]

NH3rot = np.dot(AZ(Zangle-90+180),NH3.T).T

NH3rot[3]= np.array([1.07/(2.09/np.sin(109.5*np.pi/180))*2.09, np.sin(109.5/2*np.pi/180)
    *1.07, 0.8295- np.cos(np.arcsin(1.07/(2.09/np.sin(109.5*np.pi/180))))*2.09  ])
NH3rot[4]= np.array([1.07/(2.09/np.sin(109.5*np.pi/180))*2.09, -1*np.sin(109.5/2*np.pi/180)
    *1.07, 0.8295- np.cos(np.arcsin(1.07/(2.09/np.sin(109.5*np.pi/180))))*2.09 ])

def positions(Yangle,Xoffset):
    ## Generate the shifted H positions based upon fitting parameters:
    NH3rot2 = np.dot(AY(Yangle),NH3rot.T).T
    NH3final = NH3rot2 - np.array([Xoffset,0,0])
    ## Generate second set (positions 4-6) via C2 rotation:
    NH3_C2 = np.dot(AZ(180),NH3final.T).T
    return NH3final,NH3_C2

def distances(Yangle,Xoffset,dlib):
    NH3final,NH3_C2=positions(Yangle,Xoffset)
    ## generate jump distances for EISF calculations:
    #Seung-Hun Lee OA+ C2xC3 from SI doi: 10.1063/1.5131667
    # See Table S.X.
```

```
    r0 = distance(NH3final[0],NH3final[1]) ## R1,2
    r1 = distance(NH3final[0],NH3_C2[0])   ## R1,4
    r2 = distance(NH3final[1],NH3_C2[1])   ## R2,5
    r3 = distance(NH3final[2],NH3_C2[2])   ## R3,6
    r4 = distance(NH3final[0],NH3_C2[1])   ## R1,5
    r5 = distance(NH3final[0],NH3_C2[2])   ## R1,6
    r6 = distance(NH3final[1],NH3_C2[2])   ## R2,6
    d1 = distance(NH3final[4],NH3_C2[4])   ## R7,9
    d2 = distance(NH3final[3],NH3_C2[3])   ## R8,10
    rs = [r0,r1,r2,r3,r4,r5,r6,d1,d2,dlib]
    return rs
```

Calculate total EISF based on methylammonium and nBA (n=2) structure:

```
def calcEISF(Q,*params):
    ## this is the full model by Lee et al.
    Yangle = params[0]
    Xoffset = params[1]
    dlib=0
    r0,r1,r2,r3,r4,r5,r6,d1,d2,dlib = distances(Yangle,Xoffset,dlib)
    #Seung-Hun Lee OA+ from SI doi: 10.1063/1.5131667:
    # C2xC3, just describes the CH2NH3 headgroup.
    A_A_C2xC3 = 1/18*(3+6*j0(Q,r0)+j0(Q,r1)+j0(Q,r2)+j0(Q,r3)+2*j0(Q,r4)+2*j0(Q,r5)+2*j0(Q,
    r6))
    ## C3xC4 of MA
    A_A_C3xC4 = 1/36*(3+6*j0(Q,mr1)+4*j0(Q,mr2)+2*j0(Q,mr3)+2*j0(Q,mr4)+3*j0(Q,mr5)+2*j0(Q,
    mr6)+4*j0(Q,mr7)+4*j0(Q,mr8)+4*j0(Q,mr9)+2*j0(Q,mr10))
    return  (6*A_A_C2xC3 + 6 * A_A_C3xC4)/12

    def calcEISF_C2_nBA_variablefrac(Q,*params):
    #fractional C2xC3 motion of nBA with full MA C3xC4
    Yangle = params[0]
    Xoffset = params[1]
```

```
    dlib=0
    frac=params[2]
    r0,r1,r2,r3,r4,r5,r6,d1,d2,dlib = distances(Yangle,Xoffset,dlib)
    A_A_C2xC3 = 1/18*(3+6*j0(Q,r0)+j0(Q,r1)+j0(Q,r2)+j0(Q,r3)+2*j0(Q,r4)+2*j0(Q,r5)+2*j0(Q,
    r6))
    static = np.ones(np.shape(Q))
    MA = 1/36*(3+6*j0(Q,mr1)+4*j0(Q,mr2)+2*j0(Q,mr3)+2*j0(Q,mr4)+3*j0(Q,mr5)+2*j0(Q,mr6)+4*
    j0(Q,mr7)+4*j0(Q,mr8)+4*j0(Q,mr9)+2*j0(Q,mr10))
    nBA = ((frac*A_A_C2xC3)+((1-frac)*static))
    A_total = (nBA*6 + MA*12)/18
    return A_total

def calcEISF_C3_nBA_variablefrac(Q,frac):
    #fractional C3 motion of nBA with full MA C3xC4
    r0 = distance(NH3rot[0],NH3rot[1])
    A_A_C3 = 1/9 * (3+6*j0(Q,r0))
    static = np.ones(np.shape(Q))
    MA = 1/36*(3+6*j0(Q,mr1)+4*j0(Q,mr2)+2*j0(Q,mr3)+2*j0(Q,mr4)+3*j0(Q,mr5)+2*j0(Q,mr6)+4*
    j0(Q,mr7)+4*j0(Q,mr8)+4*j0(Q,mr9)+2*j0(Q,mr10))
    nBA = ((frac*A_A_C3)+((1-frac)*static))
    A_total = (nBA*6 + MA*6)/12
    return A_total

def calcEISF_staticnBA(Q,frac):
    #static nBA with frac C3 and C4 of MA
    A_A_C3xC4 = 1/36*(3+6*j0(Q,mr1)+4*j0(Q,mr2)+2*j0(Q,mr3)+2*j0(Q,mr4)+3*j0(Q,mr5)+2*j0(Q,
    mr6)+4*j0(Q,mr7)+4*j0(Q,mr8)+4*j0(Q,mr9)+2*j0(Q,mr10))
    static = np.ones(np.shape(Q))
    nBA = (static*6)/12
    MA = ((frac*A_A_C3xC4)+((1-frac)*static))*6/12
    return nBA + MA

def calcEISF_C3(Q):
```

```
    ## this is all C3 of all H - no need to differeniate
    r0 = distance(NH3rot[0],NH3rot[1])
    A_A_C3 = 1/9 * (3+6*j0(Q,r0))
    return A_A_C3


def calcEISF_C3_variablefrac(Q,frac):
    ## this is-all C3 motion becomes fractionally static
    ## differentiate between MA and nBA H undergoing C3
    r0 = distance(NH3rot[0],NH3rot[1])
    A_A_C3 = 1/9 * (3+6*j0(Q,r0))
    static = np.ones(np.shape(Q))
    nBA = (static*6)/12
    A_total = ((frac*A_A_C3)+((1-frac)*static))*6/12 + nBA
    return A_total
```

Calculate total EISF based on methylammonium and nBA (n=3) structure:

```
def calcEISF(Q,*params):
    ## this is the full model by Lee et al.
    Yangle = params[0]
    Xoffset = params[1]
    dlib=params[2]
    r0,r1,r2,r3,r4,r5,r6,d1,d2,dlib = distances(Yangle,Xoffset,dlib)
    ##Seung-Hun Lee OA+ from SI doi: 10.1063/1.5131667:
    ## C2xC3, just describes the CH2NH3 headgroup.
    A_A_C2xC3 = 1/18*(3+6*j0(Q,r0)+j0(Q,r1)+j0(Q,r2)+j0(Q,r3)+2*j0(Q,r4)+2*j0(Q,r5)+2*j0(Q,
    r6))
    ## C3xC4 of MA
    A_A_C3xC4 = 1/36*(3+6*j0(Q,mr1)+4*j0(Q,mr2)+2*j0(Q,mr3)+2*j0(Q,mr4)+3*j0(Q,mr5)+2*j0(Q,
    mr6)+4*j0(Q,mr7)+4*j0(Q,mr8)+4*j0(Q,mr9)+2*j0(Q,mr10))
    A_total = (6*A_A_C2xC3 + 12*A_A_C3xC4)/18 ## specific to nBA2MA2Pb3I10
    return A_total
```

```
def calcEISF_C2_nBA_variablefrac(Q,*params):
    #fractional C2xC3 motion of nBA with full MA C3xC4
    Yangle = params[0]
    Xoffset = params[1]
    dlib=0
    frac=params[2]
    r0,r1,r2,r3,r4,r5,r6,d1,d2,dlib = distances(Yangle,Xoffset,dlib)
    A_A_C2xC3 = 1/18*(3+6*j0(Q,r0)+j0(Q,r1)+j0(Q,r2)+j0(Q,r3)+2*j0(Q,r4)+2*j0(Q,r5)+2*j0(Q,
    r6))
    static = np.ones(np.shape(Q))
    MA = 1/36*(3+6*j0(Q,mr1)+4*j0(Q,mr2)+2*j0(Q,mr3)+2*j0(Q,mr4)+3*j0(Q,mr5)+2*j0(Q,mr6)+4*
    j0(Q,mr7)+4*j0(Q,mr8)+4*j0(Q,mr9)+2*j0(Q,mr10))
    nBA = ((frac*A_A_C2xC3)+((1-frac)*static))
    A_total = (nBA*6 + MA*12)/18
    return A_total

 def calcEISF_C3_nBA_variablefrac(Q,frac):
     #fractional C3 motion of nBA with full MA C3xC4
     r0 = distance(NH3rot[0],NH3rot[1])
     A_A_C3 = 1/9 * (3+6*j0(Q,r0))
     static = np.ones(np.shape(Q))
     MA = 1/36*(3+6*j0(Q,mr1)+4*j0(Q,mr2)+2*j0(Q,mr3)+2*j0(Q,mr4)+3*j0(Q,mr5)+2*j0(Q,mr6)+4*
    j0(Q,mr7)+4*j0(Q,mr8)+4*j0(Q,mr9)+2*j0(Q,mr10))
     nBA = ((frac*A_A_C3)+((1-frac)*static))
     A_total = (nBA*6 + MA*12)/18
     return A_total

def calcEISF_staticnBA(Q,frac):
    A_A_C3xC4 = 1/36*(3+6*j0(Q,mr1)+4*j0(Q,mr2)+2*j0(Q,mr3)+2*j0(Q,mr4)+3*j0(Q,mr5)+2*j0(Q,
    mr6)+4*j0(Q,mr7)+4*j0(Q,mr8)+4*j0(Q,mr9)+2*j0(Q,mr10))
    static = np.ones(np.shape(Q))
    nBA = (static*6)/18
    MA = ((frac*A_A_C3xC4)+((1-frac)*static))*12/18
```

```
    return nBA + MA


def calcEISF_C3(Q):
    ## this is just C3 motion of the -NH3 ends - all C3 of all H - no need to differeniate
    r0 = distance(NH3rot[0],NH3rot[1])
    A_A_C3 = 1/9 * (3+6*j0(Q,r0))
    return A_A_C3


def calcEISF_C3_variablefrac(Q,frac):
    ## this is-all C3 motion becomes fractionally static
    r0 = distance(NH3rot[0],NH3rot[1])
    A_A_C3 = 1/9 * (3+6*j0(Q,r0))
    static = np.ones(np.shape(Q))
    nBA = (static*6)/18
    A_total = ((frac*A_A_C3)+((1-frac)*static))*12/18 + nBA
    return A_total
```

Appendix C

Supplemental Information for Excited State Dynamics in Isotopically Substituted Layered Perovskites

Preliminary Characterization

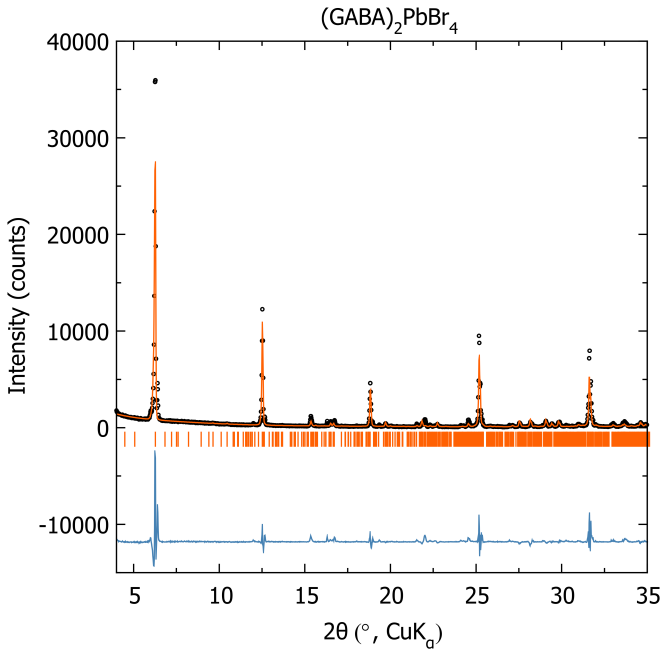

Figure 23: Powder X-ray diffraction of (a) $(GABA)_2PbBr_4$. Black circles, orange line, and blue line represent the data, fit, and difference, respectively. The PXRD data were modeled with $P2_1/c$ space group.

At room temperature, there is thermal energy to detrap self-trapped excitons and populate a free excitonic state (Figure 24, b). This gives rise to the single emissive peak

centered at ≈ 400 nm (Figure 4.2). When the temperature is lowered, there is not enough thermal energy to overcome the detrapping energy of the self-trapped exciton. Therefore, there is recombination from a distribution of states; giving rise to the observed white light emission.

Approximating τ of isotoptically-substituted layered material

The harmonic oscillator function is:

$$\omega = \sqrt{\frac{k}{m}}$$

where k is the force constant and m is the mass.

If we let 1 represent protons and 2 represent deuterons:

$$\frac{\omega_1 = \sqrt{\frac{k}{m_1}}}{\omega_2 = \sqrt{\frac{k}{m_2}}}$$

Squaring both sides, we end up with:

$$\frac{\omega_1^2}{\omega_2^2} = \frac{\frac{k}{m_1}}{\frac{k}{m_2}} = \frac{m_2}{m_1}$$

After cancelling and taking the square root of both sides, we have an expression that equates omega and mass:

$$\frac{\omega_1}{\omega_2} = \sqrt{\frac{m_2}{m_1}}$$

We will let $m_2 = 2m_1$,

$$\frac{\omega_1}{\omega_2} = \sqrt{\frac{2m_1}{m_1}} = \sqrt{2}$$

thus,

$$\omega_1 = \omega_2\sqrt{2}$$

From QENS analysis we know that τ is defined as

$$\tau = \frac{\hbar}{\omega}$$

Therefore,

$$\frac{\tau_1}{\tau_2} = \frac{\frac{\hbar}{\omega_1}}{\frac{\hbar}{\omega_2}} = \frac{\omega_2}{\omega_1}$$

$$\tau_2 = \frac{\omega_1}{\omega_2} * \tau_1$$

Thus,

$$\tau_2 = \tau_1\sqrt{2}$$

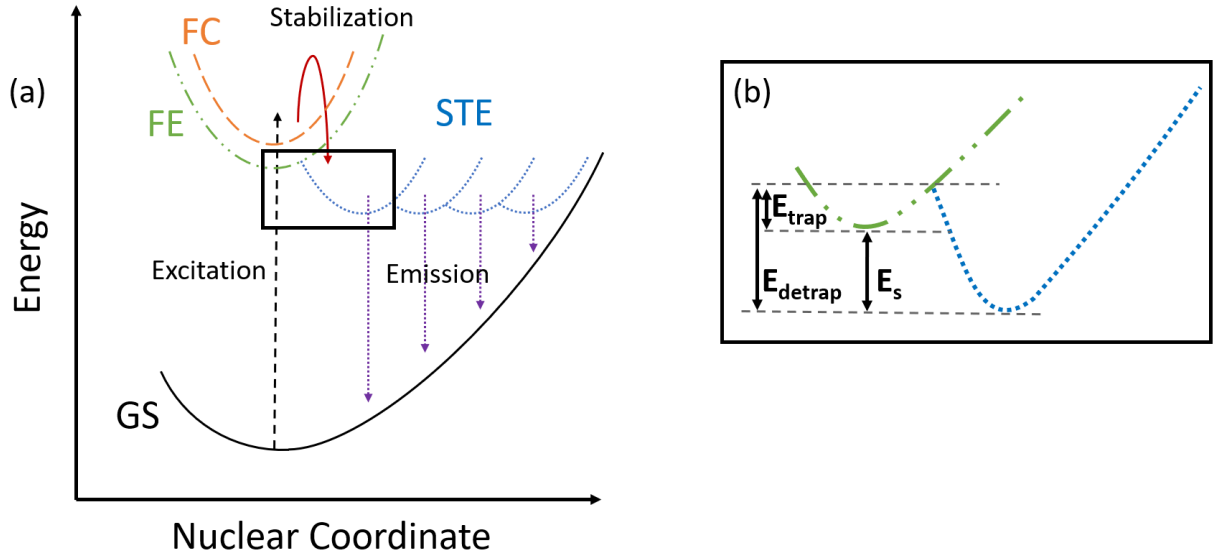

Figure 24: (a) Nuclear coordinate diagram showing excitation (black dashed line) from a ground state (solid black curve) to an excited state of either a free carrier (FC, orange dashed line), free exciton (FE, green dot-dashed line), or self-trapped exciton (STE, blue dotted line) and relaxation back to the ground state (purple dotted lines). (b) Inset shows the trapping energy (E_{trap}) of self-trapped excitons, the detrapping energy (E_{detrap}) of self-trapped excitons to free excitons, and the depth of the self-trapped excitonic well (E_S)

Table 10: Decay times of $(GABA)_2PbBr_4$ and $(d{-}GABA)_2PbBr_4$ calculated from time-resolved photoluminescence with $R(t) = B_1 \exp(-t/\tau_1) + B_2 \exp(-t/\tau_2)$. The data are well described by a bi-exponential decay consisting of two components except for measurements taken 575 and 640 nm. Error bars represent one standard deviation.

Decay times (ns)					
Wavelength (nm)	$\tau 1_{GABA}$	$\tau 2_{GABA}$	Wavelength (nm)	$\tau 1_{d-GABA}$	$\tau 2_{d-GABA}$
391	17±0.5	74±0.4	390	7±0.1	31±0.3
539	27±2	287±10	539	46±5	282±32
589	29±0.6	420±21	575	201±3	
640	315±7		640	278±7	

Appendix D

Supplemental Information for Organic-Inorganic Coupling Effects on Broadband Emission through Halide Substitution in Layered Perovskites

Preliminary Characterization

For the compounds synthesized in this study, PXRD data were modeled with space groups of *Pbca* for $(n\text{BA})_2\text{PbBr}_4$, and $(n\text{BA})_2\text{PbI}_4$ using previously reported structures[1,19] with the Rietveld method implemented in TOPAS v6 (Bruker AXS). To our knowledge, the crystal structure for $(n\text{BA})_2\text{PbCl}_4$ is not reported; therefore, the iodide .cif with the iodide ions exchanged for chloride ions was used as a reference.

The differential scanning calorimetry for $(n\text{BA})_2\text{PbI}_4$ describe transitions at $\approx$ 250 K and $\approx$ 275 K where there is a discontinuity in the MSD (Figure 5.4). The differential scanning calorimetry for $(n\text{BA})_2\text{PbCl}_4$ has a transition at $\approx$ 205 K that does not correspond to any discontinuities in the MSD.

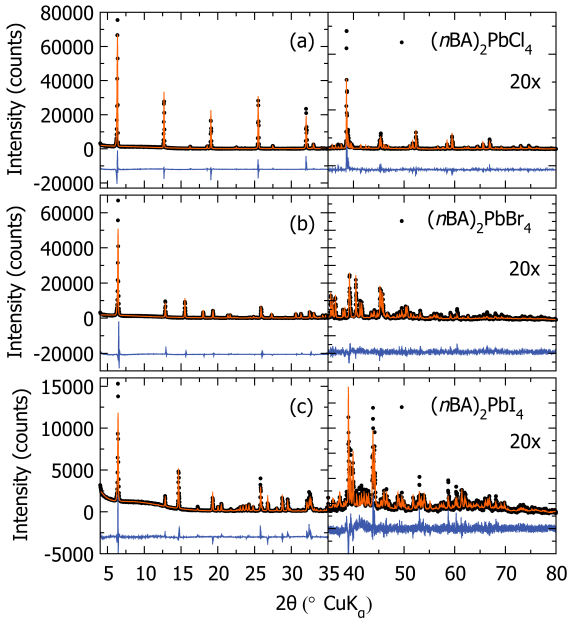

Figure 25: Powder X-ray diffraction of (a) $(n\text{BA})_2\text{PbCl}_4$, (b) $(n\text{BA})_2\text{PbBr}_4$, and (c) $(n\text{BA})_2\text{PbI}_4$. Black circles, orange line, and blue line represent the data, Rietveld refinement, and difference curve, respectively.

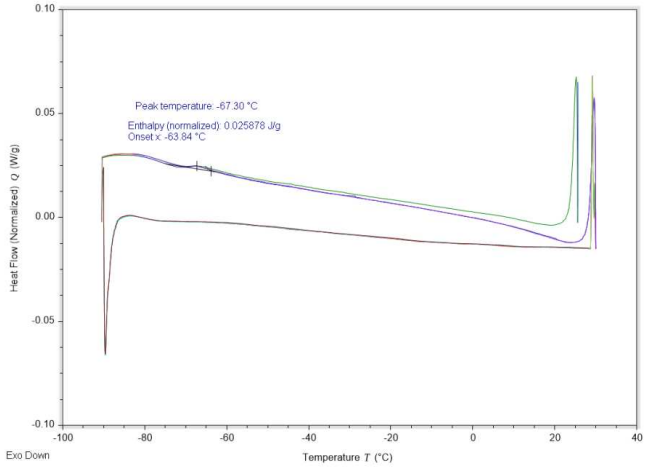

Figure 26: Differential scanning calorimetry of $(n\text{BA})_2\text{PbCl}_4$ collected from -90 °C to 30 °C. There is a transition at -67.30 °C (205 K). These transitions do not significantly affect the n-butylammonium dynamics.

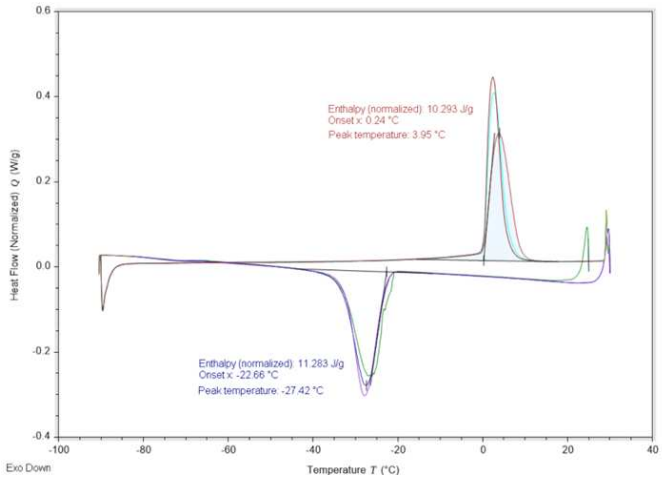

Figure 27: Differential scanning calorimetry of $(n\text{BA})_2\text{PbI}_4$ collected from -90 °C to 30 °C. There is a transition at -27.42 °C (245 K) and 3.95 °C (277 K). These transitions coincide with the discontinuity in the iodide analog MSD, indicating the n-butylammonium dynamics change significantly upon a structural transition.

Appendix E

Supplemental Information for Structural Dynamics in Broadband Emitting Solid Solutions

Preliminary Characterization

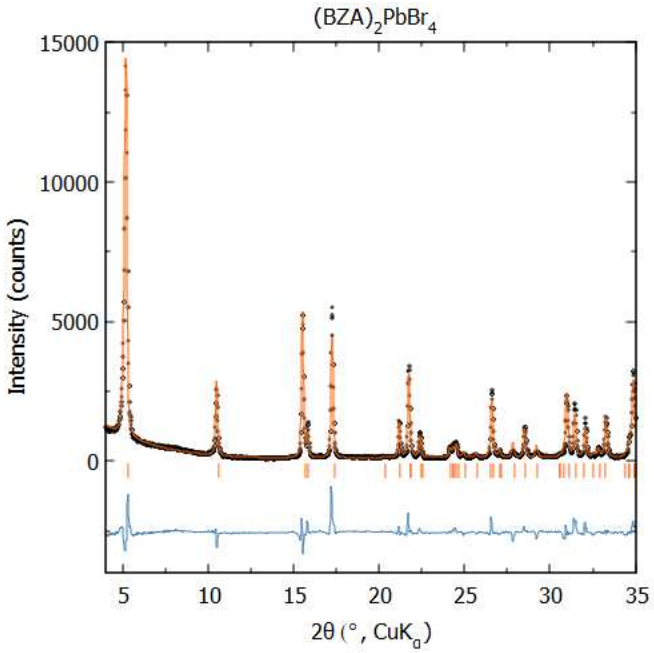

Figure 28: Powder X-ray diffraction of $(BZA)_2PbBr_4$. Black circles, orange line, and blue line represent the data, Rietveld refinement, and difference curve, respectively.

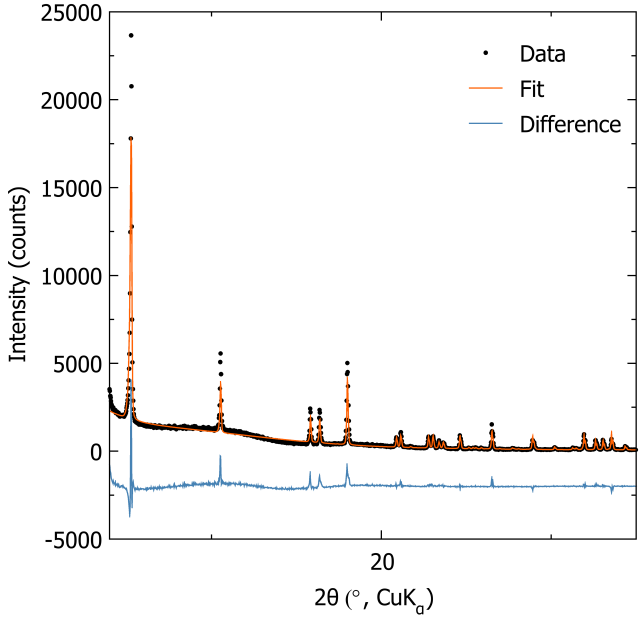

Figure 29: Powder X-ray diffraction of $(BZA)_2PbCl_4$. Black circles, orange line, and blue line represent the data, Rietveld refinement, and difference curve, respectively.

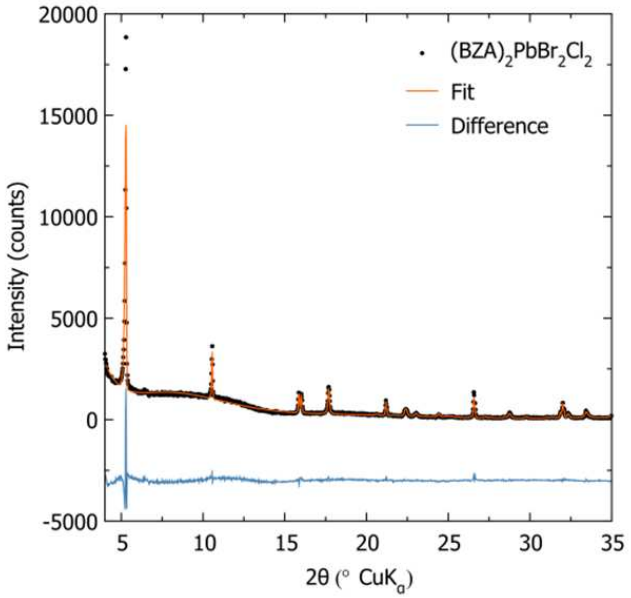

Figure 30: Powder X-ray diffraction of $(BZA)_2PbBr_2Cl_2$. Black circles, orange line, and blue line represent the data, Rietveld refinement, and difference curve, respectively.